3D non-linear beam dynamics for the LHC upgrades

Thomas Pugnat

université PARIS-SACLAY

3D non-linear beam dynamics for the LHC upgrades

Dynamique des faisceaux de particules non-linéaire pour les upgrades du LHC

Thèse de doctorat de l'Université Paris-Saclay

École doctorale n°576 Particules, Hadrons, Énergie, Noyau, Instrumentation, Imagerie, Cosmos et Simulation (PHENIICS)
Spécialité de doctorat: Physique des accélérateurs
Unité de recherche: Université Paris-Saclay, CEA, Département des Accélérateurs, de la Cryogénie et du Magnétisme, 91191, Gif-sur-Yvette, France
Référent: Faculté des sciences d'Orsay

Thèse présentée et soutenue à Paris-Saclay, le 22 Juin 2021, par

THOMAS PUGNAT

Composition du Jury :

Patrick PUZO Professeur des Universités, Université Paris-Saclay	Président
Jean-Marie DE CONTO Professeur des Universités, Université Grenoble Alpes	Rapporteur & Examinateur
Yannis PAPAPHILIPPOU Professeur invité et chef de groupe, CERN (BE - ABP/HSI)	Rapporteur & Examinateur
Angeles FAUS-GOLFE Chercheur, Université Paris-Saclay (CNRS/IN2P3/IJCLab)	Examinatrice
Rogelio TOMAS Physicien des accélérateurs senior, CERN (BE - ABP/HSS)	Examinateur

Direction de la thèse :

Olivier NAPOLY Thèse d'état, CEA Saclay (DRF/IRFU/DACM)	Directeur de thèse
Barbara DALENA Chercheur, CEA Saclay (DRF/IRFU/DACM)	Co-Directice de thèse

Thèse de doctorat
NNT : 2021UPASP047

À mes grands-parents PUGNAT et Jaqueline VERLEST, partis trop tôt.

”Il serait difficile de rendre raison des histoires et des oracles que nous avons rapportés, sans avoir recours aux Démons, mais aussi tout cela est-il bien vrai? Assurons nous bien du fait, avant de nous inquiéter de la cause.”

”It would be difficult to justify the stories and oracles we have reported, without resorting to the Demons, but is all this true? Let’s be sure of the facts before we worry about the cause.”

BERNARD LE BOUYER DE FONTENELLE, La dent d’or, **Histoire des Oracles,** 1687

Remerciements

Je tiens tout d'abord à remercier mon encadrante Barbara DALENA du Département des Accélérateurs, de Cryogénie et de Magnétisme (DACM) au CEA/Saclay pour son encadrement et pour m'avoir fait confiance tout au long de ces trois années de thèse. Sa patience, son soutien et son expérience m'ont été d'un grand secours tout au long de ce parcours.

Je remercie aussi fortement mon Directeur de thèse Olivier NAPOLY pour avoir accepter de diriger ces travaux avant son départ. Son soutien et ses conseils qu'il m'a prodigué, ont été d'une grande aide tout au long de ma thèse.

Je remercie Jean Marie DE CONTO, Professeur de l'Université Grenoble Alpes (IN2P3), et Yannis Papaphilipou, Group leader et Senior Physicist à l'Organisation Européenne pour la Recherche Nucléaire (CERN BE - ABP/HSI), pour avoir accepté la tâche de Rapporteur et pour l'ensemble des remarques qu'ils ont apportées.

Je remercie Patrick PUZO, Professeur de l'Université Paris-Saclay, d'avoir accepté la lourde tâche de Président de Jury. Je remercie Angeles FAUS-GOLFE, chercheuse à l'Université Paris-Saclay (CNRS/IN2P3/IJCLab) et Rogelio Tomàs, Senior Accelerator Physicist au CERN (BE - ABP/HSS) pour avoir accepté d'examiner mon travail en faisant partie de mon Jury.

Je remercie mes chefs de service Pierre VEDRINE et Philippe BREDY (DACM), ainsi que mon directeur du laboratoire Jerome Schwindling (LEDA) pour m'avoir permis de travailler au sein de leur service dans de bonnes conditions. À travers eux, je remercie aussi leurs équipes et tout particulièrement l'équipe de dynamique de faisceau du LEDA, pour m'avoir si chaleureusement accueilli parmis eux, pour leur nombreux conseils et pour m'avoir initié à l'épistémologie.

I thanks the beam dynamic team from the CERN for the discussion and expertise. I also thanks Susana IZQUIERDO BERMUDEZ and Ezio TODESCO from the CERN Magnet designer team as well as Lucas BONAVENTURA and Abele SIMONA from Polytechnico di Milano, and Andrea FRANCHI from the ESRF for their expertise

and help.

Enfin, je souhaiterais remercier toute ma famille, que se soit mes parents, mes frères et soeur, mes grand-parents et autres, pour m'avoir toujours soutenu dans la voie que j'ai choisi de suivre. Et je remercie ces grandes dames que j'ai croisé au détour du chemin de ma vie et qui m'ont redonné un élan.

À vous tous et à tous ceux que j'aurai éventuellement oublié, merci.

Contents

List of Figures

List of Tables

List of Symbols and Acronyms

Acronyms

Symbol	Description	Page
ABB	Direct and Cross Amplitude Beta-Beating.	42
AD	Direct and Cross Amplitude Detuning.	39
BPM	Beam Position Monitor.	41
CERN	European Organization for Nuclear Research (Acronym: *Conseil Européen pour la Recherche Nucléaire*).	5
CS, NC	Acronym for the Connector Side and Non-Connector side of a magnet.	10
DA	Dynamic Aperture.	91
HE	Hard Edge model, the magnetic field is constant inside and null outside the magnet without any transition.	45
HE+Heads	Hard Edge with Heads model, similar to the HE model but with additional multipole in the magnet extremities.	46
HL-LHC	High-Luminosity LHC, one project of upgrade for the LHC to improve its luminosity.	11
IP	Interaction Point, Point where the beams collide.	9
IR	Interaction Region, region containing the matching section quadrupoles, the Dispersion Suppressor, IT and IP.	9
IT	Inner Triplet or Final Focusing quadrupoles, Sequence of quadrupoles on each side of IPs.	9
LHC	Large Hadron Collider, the circular hadronic collider at the CERN with a circumference of $27\,\mathrm{km}$ and an energy at collision $13\,\mathrm{TeV}$.	7
Lie2	Model where the extra multipole in the HE+Heads model are replace by the Map develop in 4 using Lie Algebra.	47

MCOXS	Main octupole correctors in the LHC IRs.	79
MD	Machine Developement, Session of specified test on the machine.	79
MOS, MCOS	Main familly of octupole correctors in the LHC Arcs.	79
MQXA	One of the LHC IT Quadrupole (Q1/Q3) with 70 mm of aperture and design by the KEK.	10
MQXFS	IT Quadrupoles for HL-LHC (Q1, Q2a, Q2b and Q3) with a physical aperture of 150 cm.	12
RDT	Resonance Driving Terms	37

Math and Physic notations

Symbol	Description	Dimensions	Units	Page
$(\vec{q},\vec{p})$	Vector of canonical variable in the magnet, .i.e (x,p_x), (y,p_y) and (z,p_z). The momentum is normalized by the P_0.	(3,3)	(m,rad)	23
(s,δ)	Curviline canonical variable, respectively for position and momentum deviation.	(1,1)	(m,rad)	23
$\mathbf{R}$,$\mathbf{A}$	Respectively, rotation matrix and normalized space and the matrix transforming the normalized into the particle space.	$d \times d$	–	36
$\mathcal{H}$,$\mathcal{K}_{8D}$	Respectively, relativistic and approximated Hamiltonian. They are then decomposed into $\mathcal{H}_0$ and $\mathcal{H}_p$, the linear and perturbative Hamiltonian.	MeV or 1	1	18
$\mathfrak{M}$,$\mathfrak{A}$	Respectively, transfer map in the particle space, and map transforming the particle space into the normalized one.	–	–	36
$\Re$,$\Im$	Real and Imaginary part of the followed complex number.	–	1	19
$\vec{A}$, A_u	Vector potential ($u \in \{x,y,z\}$).	3	MeV/c	18
$\vec{a}$, a_u	Vector potential normalized by P_0 ($u \in \{x,y,z\}$).	3	1	24
$\vec{B}$, B_u	Magnetic field ($u \in \{x,y,z\}$ or $u \in \{\rho,\phi,z\}$ depending of the coordinate system).	3	MeV/c	15
b_n, a_n	Respectively n^{th}-order Normal and Skew harmonics normalized by the reference magnet strength B_{ref} (see Eq. (2.4)).	–	10^{-4}	16
$B_{u,n}$	Magnetic Field n^{th}-order harmonics with $u \in \{s,c\}$ for normal and skew harmonic respectively.	–	Tm^{-n}	15
$C^{[l]}_{u,n}$	Generalized gradient with $u \in \{s,c\}$ respectively for normal and skew harmonics (see Eq. (2.15)).	–	$\text{Tm}^{-(n+l)}$	20
l, ND	Respectively, current and max order of the generalized gradient derivatives along z.	–	1	20
n	Order of the Magnetic Field harmonic, i.e. half the number of pole in the equivalent magnet.	–	1	15
P_0	Total momentum of the referential particle.	–	MeV/c	24
q	Charge of the particle.	–	1	18

Physical constants

Symbol	Description	Value	Units	Page
c	Speed of light.	2.99792458×10^8	$\mathrm{m\,s^{-1}}$	18
m_p	Mass Energy of the Proton.	938.2720813	MeV	18

Introduction

When studying non-linear beam dynamic in accelerator physics, the main focus is on beam quality and particularly on long-term beam stability. Indeed, since cathodic rays and the work of E. Rutherford on his atomic model theory (1907-1919) which prompted J. Cockcroft and E. Walton to create the first $500\,\mathrm{kV}$ electrostatic accelerator (1928-1932), particle accelerators have diversified and been more specific for use. These accelerators must provide particle beams at ever greater energies for fundamental physics experiments. This implies an increase in their size as well as some magnetic or physic constraints in the design of elements which compose the ring. This is the case at CERN with the LHC of $27\,\mathrm{km}$ circumference, for example. In order to reach high peak magnetic field, accelerators depend more and more on decisive technological advances such as superconducting magnets. Those magnets have also strong magnetic field non-linearities, that may deteriorate the long-term stability of the machine. Therefore, they need to be accurately known and corrected, otherwise, the number of events in the experiments would decrease and the accelerator elements will be degraded faster than expected.

In 1985, a new program named TEAPOT [1] was presented for fast and exact particle tracking in an accelerator with magnet errors and misalignments. It is a method in order to improved the accuracy of the tracking using thin lens compared to thick lens. It was shown that it improves the accuracy of the Twiss parameters and amplitude detuning terms calculation and the computational speed of the tracking. A comparison with program from the same period (MARYLIE and RACETRACK) has shown better results, in particular compared to RACETRACK. In 2013, H. Burkhardt [2] has also shown a good accuracy between the thick and thin lens simulation in the estimation of the LHC dynamic aperture. However, as specify in [1], TEAPOT neglects the Fringe Field and consider only the hard edge approach of the magnetic Field.

In a paper from 1999 [3], M. Venturini has presented a new method to compute the 3D vector potential using the generalized gradient. This method can use the magnetic field from direct measurement or computation with the aid of some 3D electromagnetic code. The vector potential obtained using this method can then be used in transfer maps derived from the Lie algebra. He has shown that the reconstruction of the magnetic field using this approach is very accurate. Following this works, A. V. Bogomyagkov [4] has estimated analytically the contribution of the HL-LHC inner triplet quadrupoles Fringe Field to the amplitude detuning and chromaticity. However, the latter

studies have only consider the pure quadrupolar 3D magnetic field (b_2).

In a report, E. H. Maclean [5] presents an overview of the beam stability measurements against magnets non-linearities in the LHC, using different observable such as the variation of the number of oscillations per revolution as a function of the amplitude of particles. In this study, the measurements were compared to simulation predictions using the values of non-linear magnetic field harmonics measured element by element. This allowed them to show an improvement in beam stability and a gap between model predictions and beam-based corrections. They have shown that this discrepancy cannot be explained by the uncertainties of their actual model. However, their study used averaged field harmonics along the magnet, without considering the harmonics longitudinal distribution.

All of these studies showed that the Hard Edge model using thin lens with constant step size is not sufficient to accurately describe the movement of particles inside a magnetic field. It has also been shown that an improvement in beam stability is correlated to the accuracy of non-linearity corrections (Ref. [5]). Finally, a discrepancy is observed between the LHC corrector strength predictions from the model using magnetic field measurements and their beam-based estimations.

The aim of this thesis is to investigate if the Fringe Field in the LHC and HL-LHC type magnets can explain some of the discrepancy observed. More in general, the objective is to model and quantify the effect of the 3D magnetic field on different beam based observables.

The first chapter introduces the accelerators to which our studies are applied. It preliminary reviews their respective achievements and objectives. This lead us to aboard the definition of the Luminosity. Then, their Interaction Regions, Final Focusing magnets and correctors package are described. As shown in Ref. [5], the main sources of non-linearities at collision energy are the Inner Triplet magnets in the LHC near ATLAS and CMS. This is explained by the fact that the betatronic functions are the highest in those region. On other hand, since Inner Triplet magnets are superconductors, it is expected to have great discrepancy between the harmonics values in the center of the magnet and the extremities. Those points tend to suggest that small discrepancies between the Model and reality in those regions could have major impact on Beam Dynamic.

The second chapter reviews the definition of the Fringe Field. The idea is to show that the notion of Fringe Field often used, has lost one of its element through time. First section reviews what are the multipoles harmonics and how they are measured. Then, the Fringe Field definition given by H. Wiedmann [6] is compared to its representation though time thanks to the work of G. E. Lee-Whiting [7], E. Forest [8] and M. Venturini [3]. In the final section of this chapter, the method to obtain the 3D vector potential from this last paper is derived.

Using this 3D vector potential, the perturbation theory considering the Fringe Field is studied in the 3rd chapter. After defining the approximated Hamiltonian used in this thesis and reminding some basics about linear transverse beam dynamics, a decomposition of the vector potential contributions to the Hamiltonian perturbative part is derived.

Then, their impacts on three different beam-based observables are studied. First, we study the variation of revolution frequencies in the phase-spaces as the actions increase, i.e. the amplitude detuning (AD). Then, we look at the different Fringe Field contributions to the Resonance Driving Terms (RDTs). Finally, the non-linear variation of the beta-beating measurement as the actions increase (i.e. amplitude beta-beating or ABB) is studied.

The following 4th chapter focuses on how to accurately track a charged particle into a magnetic element with a good compromise with the CPU time. After quickly reminding what is a simplectic map, the three models that are compared in this thesis (i.e. the Hard Edge, the Hard Edge with Head and the Lie2 models) are presented. The implementation in the CERN transport code, SixTrack, of the last model is also presented.

In the 5th chapter, the impact of the three models, presented in chapter 4, on the amplitude detuning is studied. This beam-based observable refers to the variation of the transverse Phase-Space angular frequency (i.e. the tune) with respect to the action of the particle. It is the most direct and stable measurement of beam non-linearities. The impact of the model on the correctors strength expected to correct this amplitude detuning, is also quantified and compared to present strength specifications. Those correctors are used to correct locally non-linearities (i.e. reduce the beam Resonance Driving Terms (RDTs), Ref. [9]). Both predictions for the HL-LHC and comparison with measurements for LHC are discussed.

In the 6th chapter, a new beam-based observable is considered. That is the variation of the measured betatronic function deviation from nominal values with the action of the particle. There are two methods to measure it, either from the Amplitude of the main Spectral Line or from the Phase of the main Spectral Line of Beam Position Monitor (BPM) reading along the machine. In this thesis, we focus on the former. As in the case of the amplitude detuning we look at both predictions for HL-LHC and existing or possible measurements in LHC. At first, a comparison between the Hard-Edge and Hard-Edge with Heads models is made for the HL-LHC optics. Then, an analysis of several amplitude detuning measurements, performed during the LHC machine studies, are made in order to check if the phenomena is already observed in the LHC. And finally, three configurations of octupole are proposed in order to generate a horizontal amplitude beta-beating of $+500\,\%\mu\mathrm{m}^{-1}$. This choice is made such that this phenomena is higher that the Beam Position Monitors noise.

In the last chapter, the same models comparison as in the 5th chapter, is made on the Dynamic Aperture (DA) but only for the HL-LHC project. The DA is defined as the region of stable motion of the particles against magnet non-linearities and is often used to define tolerances on magnets conception in the design phase of circular accelerators. Unlike amplitude detuning, there is no analytic calculation of Dynamic Aperture including field errors and corrections. Its computation relies on tracking simulations therefore an accurate, symplectic and efficient non linear transfer map is necessary for large hadrons storage rings, as the LHC. This is the main motivation for defining the 3rd model described in chapter 4.

Chapter 1

The Large Hadron Collider and its upgrade in Luminosity

At the end of the World War II, the European research potential in Physics has almost disappeared. So, a small group of scientists and politics proposed the creation of an European Scientific Laboratory starting with R. Dautry, P. Auger and L. Kowarski from France, E. Amaldi from Italy and N. Bohr from Denmark. In 1949, during an European Conference for the culture, L. de Broglie made officially this proposal and in 1952, eleven European governments agreed to the creation of the CERN (i.e. "Conseil Européen pour la Recherche Nucléaire") at Meyrin (Switzerland) near the French-Swiss border.

Its creation is effective in September 1954, the 29th when twelve European States[1] members of the CERN Council signed the CERN convention [10]. And since its beginning, the CERN purposes are clearly oriented to Research in Accelerator and Particle Physics (and Astro-Particle Physics) and to "make generally available [...] its experimental and theoretical work" [10]. Since then, the CERN has build many accelerator, increasing in energy generation after generation ((p) for proton and (e) for electron/positron). Fig. 1.1 shows the latest CERN accelerator complex. The milestones of this project are:

1957: the Synchro-Cyclotron (SC, Beam Energy 600(p)MeV, Circ. 15.7 m)

1960: the Protons Synchrotron (PS, Beam Energy 28(p)-0.5(e)GeV, Circ. 628 m),

1971: the Super Protons Synchrotron (SPS, Beam Energy 450(p)-20(e)GeV, Circ. 7 km),

1981: the Large Electron Positron collider (LEP, Beam Energy 55-100(e)GeV, Circ. 27 km),

2008: the Large Hadron Collider (LHC, Beam Energy 6.5(p)TeV, Circ. 27 km).

[1] European Stat members of the CERN Council in 1954: Belgium, Denmark, France, the Federal Republic of Germany, Greece, Italy, the Netherlands, Norway, Sweden, Switzerland, the United Kingdom and Yugoslavia

These developments have been rewarded with major discoveries such as: neutral currents (Gargamelle, 1973), W and Z bosons (UA1 and UA2, 1983), the direct CP violation (NA48 at CERN and KTeV at Fermilab, 1999) and a boson with mass around $125\,\mathrm{GeV}/c^2$ consistent with the Higgs boson (ATLAS and CMS, 2012).

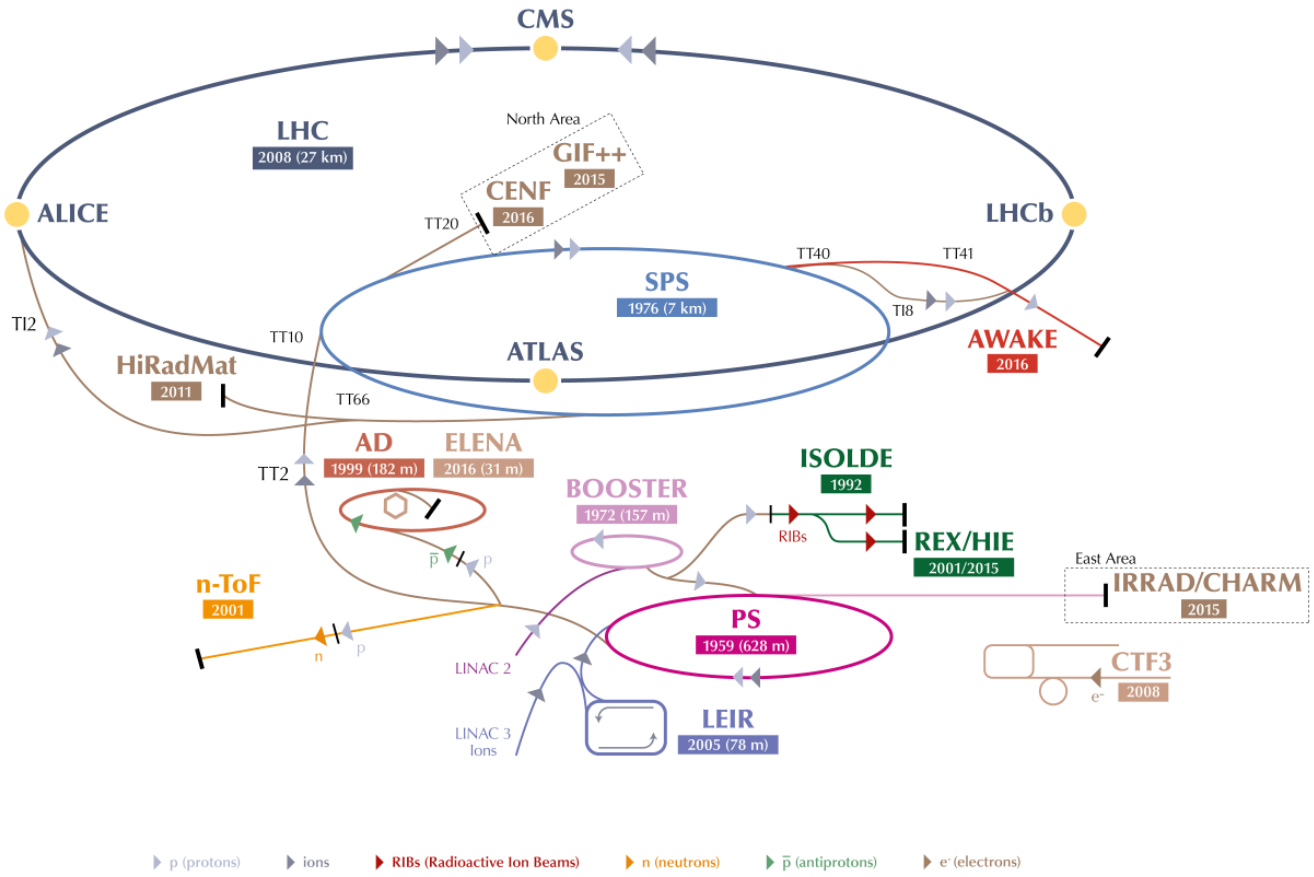

Figure 1.1: The CERN accelerators complex (© 2016-2020 CERN).

Today, many experiments are made at CERN on Fundamental Physics, even outside the LHC as can be seen in Fig. 1.1. The experiment GBAR (Gravitational Behaviour of Antimatter at Rest) measures the freefall acceleration under gravity of antimatter after being cooldown in an anti-proton decelerator. The n-Tof facility studies the interactions between neutrons and atoms nuclei. One application would be neutron imaging device for dense materials for example. The ISOLDE facility provides low energy radioactive beam (because of excess or neutron deficiency) and studies its properties. The CHARM facility allows tests to check how electronic components behave in radioactive environment. In 2018, it was used to test the satellite CELESTA (CERN Latchup and Experiment STudent sAtellite).

The beams of these experiments and of the main LHC ring come from the CERN accelerators injector chain, see Fig. 1.1. After leaving the source, the protons are first accelerated in a linear accelerator (LINAC2) to 50 MeV. The beams from LINAC2 are further accelerated in the four Proton Synchrotron Booster (PSB) rings to $1.4\,\mathrm{GeV}$, then by the Proton Synchrotron (PS) to $26\,\mathrm{GeV}$. The Super Proton Synchrotron (SPS) at the end of the injection chain delivers protons for the LHC with an energy of $450\,\mathrm{GeV}$ through two over 3 km long transfer lines (TI2 and TI8).

After the LHC injection phase that lasts 20 to 30 minutes, the beams are accelerated in about 20 minutes using a specially designed superconducting radio-frequency system (RF) to an energy of up to 7 TeV. This system consists of Sixteen cavities of high-purity niobium, which deliver an accelerating voltage of up to 16 MV per beam.

1.1 The Large Hardon Collider

1.1.1 Presentation of the Large Hadron Collider

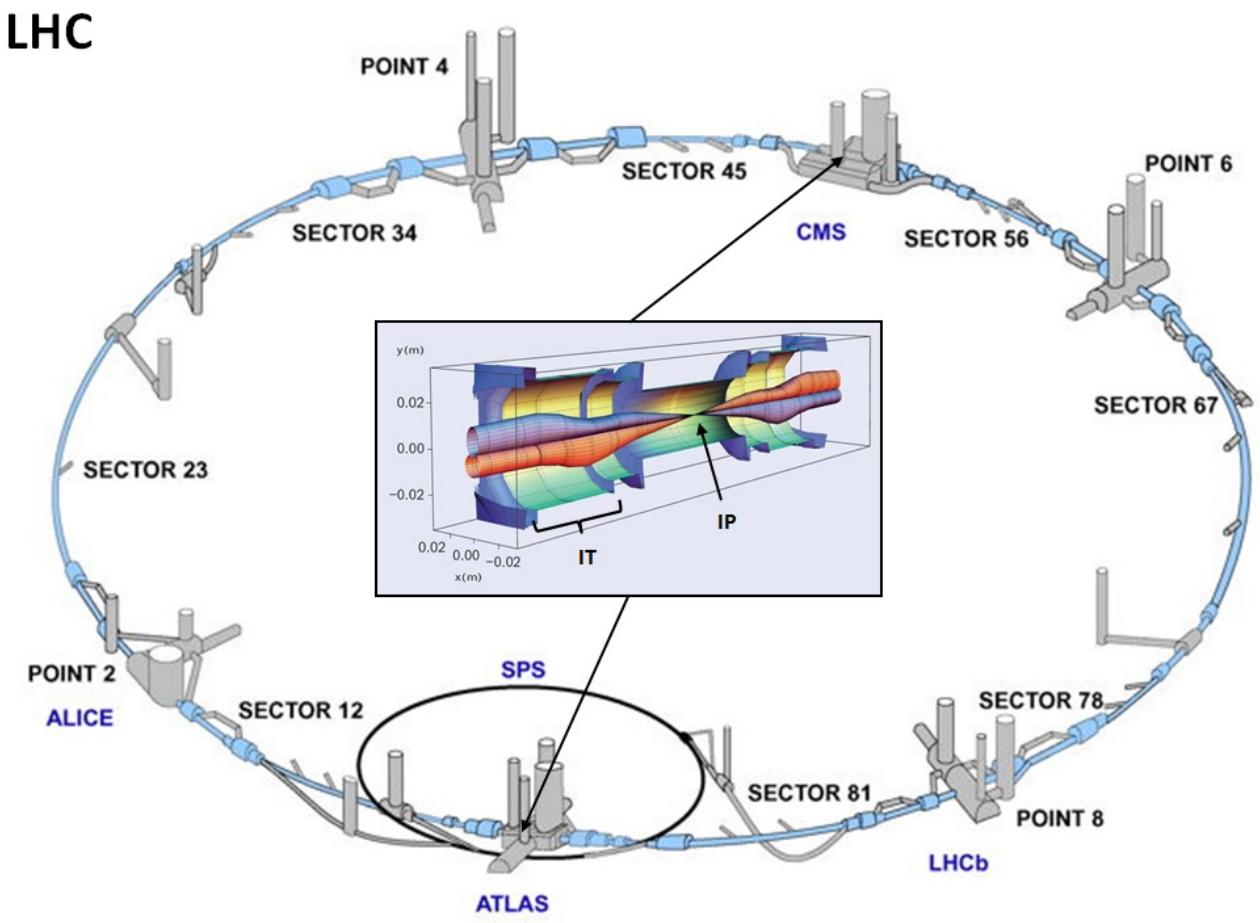

Figure 1.2: Structure of the LHC and 3D view of the Beams from the Inner Triplet (IT) to the Interaction Point (IP).

In 2008, the CERN inaugurated the Large Hadron Collider (LHC) also referred as the world's highest energy collider (see Ref. [11]). It supports a broad particle-physics program at the energy frontier [12]. Among others, its goals are to check the Higgs Boson existence, find candidate for Dark Matter or find indices of new physics beyond the Standard Model. Since the 1st run in 2009, the LHC was the source of many discoveries such as the following non exhaustive list:

- the 1st quark-gluon plasma (the densest matter thought to exist besides black holes) [13],

- the χ_{b1} (3P) and χ_{b2} (3P) bottomonium state [14, 15],
- the Higgs Boson [16, 17, 18],
- a very rare decay of the B_s meson into two muons ($B_s^0 \rightarrow \mu^+\mu^-$, matching the prediction from the non-supersymmetrical Standard Model rather than the many branches of supersymmetry [19]),
- two excited states of the bottom Xi baryon Ξ_b^- and Ξ_b^{*-} [20]
- the existence of pentaquarks or tetraquarks such as Z(4430) [21], X(4274), X(4500), X(4700) and X(4140) [22].

In order to make those discoveries, the LHC has been designed to reach a Peak luminosity of $1.0 \times 10^{34}\,\mathrm{cm}^{-2}\mathrm{sec}^{-1}$ at the main experiments (see Ref. [23]). Inside a ring of $27\,\mathrm{km}$ of circumference, two proton beams circulate in opposite direction at an energy of $6.5\,\mathrm{TeV}$ (equivalent to a speed of $0.999\,999\,991\,\mathrm{c}$). Each beam make more or less 11 000 revolutions per second. The accelerator in itself, is composed of 1 232 Dipoles used to bend the beam into the $27\,\mathrm{km}$ circumference and 392 main Quadrupoles used to focus and defocus the beam in order to keep the beam into a stable oscillating motion [23]. Their cables are composed of filament of superconductive niobium-titane (NbTi) inside copper, and kept at a temperature of $1.9\,\mathrm{K}$ with liquid helium.

In Fig. 1.2, it can be seen that the ring is divided in 8 arcs each composed of 21 FODO cells and 8 straight insertions for different functionalities:

Point 1: ATLAS: A particle detector using multiple layer of calorimeter for multiporpose experiments.

Point 2: ALICE: A particle detector for interaction between heavy ions for studying quark-gluon plasma.

Point 3: Momentum Collimation region.

Point 4: Region where the beam is kept at reference energy with Radio-Frequency Cavities.

Point 5: CMS: A particle detector similar to ATLAS and for similar purpose but with different detector technologies.

Point 6: Extraction region.

Point 7: Betatron Collimation region.

Point 8: LHCb: a particle detector specialized in the b-physics in order to measure the parameters of CP violation and help explaining the matter-antimatter asymmetry.

It is also important to note that there are two points of Injection from the SPS into the LHC for the two beams. They are located near ALICE (point 2) and LHCb (Point 8).

1.1.2 The LHC Interaction Regions and Inner Triplet magnets

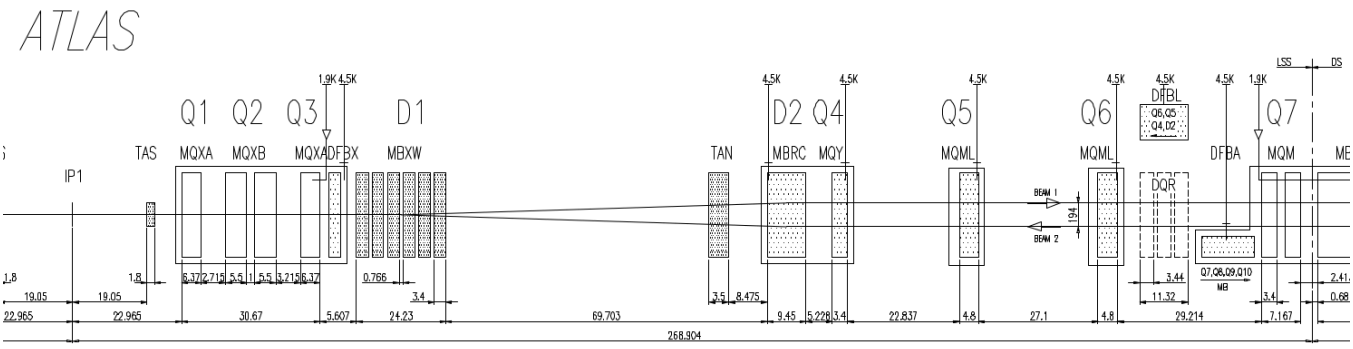

Figure 1.3: Schematic layout of the right side of IR1. (see Ref. [23]).

Coming from the Arcs (from the right side in Fig. 1.3), each beam passes through the matching section quadrupoles Q_4 to Q_7 followed by the Separation Dipoles[1] and then the Inner Triplet (IT) before reaching the experiment. The Interaction Points (IP) is the position where the 2 beams collide at a center-of-mass energy from 13 TeV to 14 TeV in the last LHC Run. This sequence is called the Interaction Regions (IR). The goal of the IT quadrupoles, also known as Final Focusing quadrupoles, is to make the betatronic function at the IP the lowest possible[2] and equal in both transverse axis in order to have a round beam. To reach this goal, the size of the beam in the IT quadrupoles is the highest along the accelerator. This implies that those quadrupoles must have a very strong magnetic field and a very big physical aperture. In the LHC, those Final Focusing magnet are called MQXA for Q1 and Q3, and MQXB for Q2.

Table 1.1: LHC Final Focusing Quadrupoles (MQXA and MQXB) main parameters (Ref. [23])

Type	MQXA	MQXB
Coil inner diameter	70 mm	70 mm
Magnetic length	6.37 m	5.5 m
Operating temperature	1.9 K	1.9 K
Nominal gradient	215 T/m	215 T/m
Nominal current	7149 A	11 950 A
Cold bore diameter OD/ID	66.5/62.9 mm	66.5/62.9 mm
Peak field in coil	8.6 T	7.7 T
Cable width, cable 1/2	11/11 mm	15.4/15.4 mm
Mid-thickness, cable 1/2	1.487/1.340 mm	1.456/1.146 mm
Keystone angle, cable 1/2	2.309/1.319 deg.	1.079/0.707 deg.
No of strands, cable 1/2	27/30	37/46
Strand diameter, cable 1/2	0.815/0.735 mm	0.808/0.650 mm
Cu/SC Ratio, cable 1/2	1.2/1.9	1.3/1.8
Filament diameter, cable 1/2	10/10 μm	6/6 μm

The IT (Q1, Q2, Q3 in Fig. 1.3) is composed of four single-aperture quadrupoles with a coil aperture of 70 mm. The magnets are cooled with superfluid helium at 1.9 K. Two types of quadrupoles are used in the triplet, 6.6 m long

[1] Two dipoles called D1 and D2 set to make the beams pass from two tube-lines in the Arcs to one in the IR.
[2] The value of the betatronic function at the IP is called β^*.

MQXA magnets designed and developed by KEK (Japan) and $5.7\,\mathrm{m}$ long MQXB magnets designed and built by FNAL (USA). Together with the orbit correctors MCBX, skew quadrupoles MQSX and multipole spool pieces were supplied by CERN [23]. Alongside the LHC main dipoles, the high-gradient, wide-aperture IT quadrupoles are the most demanding magnets in the collider, see Tab. 1.1. They must operate reliably at $215\,\mathrm{T/m}$, sustain extremely high heat loads in the coils, high radiation dose during their lifetime, and have a very good field quality, as shown in Tab. 1.2. The design of the MQXA quadrupole is based on a four-layer coil using $11\,\mathrm{mm}$ wide Rutherford-type graded NbTi cables. The coils are wound and cured in two double layers, and are assembled using $10\,\mathrm{mm}$ wide spacer-type collars. The MQXB design features a two-layer coil, with each layer individually wound using a $15.4\,\mathrm{mm}$ wide Rutherford-type NbTi cable.

Table 1.2: Field harmonics integrated strengths on the magnet considering the magnetic measurement and the magnetic model with the beam screen from the WISE database.

	b_3	b_4	b_5	b_6	b_7	b_8	b_{10}	a_3	a_4	a_5	a_6	a_7	a_8
MQXA.1R1	-0.391	1.017	-0.020	0.228	-0.016	-0.102	-0.102	0.317	-0.076	0.003	-0.045	0.012	0.003
MQXA.3R1	-0.370	1.270	-0.034	0.213	-0.016	-0.006	-0.026	-0.007	0.127	0.029	-0.014	0.007	0.005
MQXA.3L5	-0.285	1.414	-0.004	0.245	-0.013	0.046	-0.027	-0.165	0.182	-0.004	-0.053	-0.005	0.019
MQXA.1L5	-0.140	1.512	-0.024	0.268	-0.010	0.146	-0.097	0.180	-0.343	-0.031	-0.025	0.013	-0.015
MQXA.1R5	-0.167	1.451	-0.040	0.246	-0.013	0.146	-0.101	0.464	-0.018	0.051	0.025	-0.009	-0.004
MQXA.3R5	-0.073	1.503	-0.047	0.206	-0.008	0.050	-0.026	-0.418	-0.311	-0.044	-0.026	-0.005	-0.011
MQXA.3L1	-0.167	1.255	0.081	0.194	-0.010	-0.002	-0.025	0.222	0.129	-0.012	-0.011	0.005	-0.008
MQXA.1L1	0.652	0.882	-0.040	0.322	0.004	-0.103	-0.098	-0.052	0.232	0.038	-0.029	-0.003	-0.002

The LHC Inner Triplet magnet of type MQXA has a strong b_4 which comes from the ovalization of the coils and iron (Ref. [24]), and how the connection is made in one of the magnet extremity. The measured values of the integrated harmonics and their STD are reported in Table 1.3 for the body, connector (CS) and non-connector side (NC)[1]. The effect on the field harmonics of the beam screen will be discussed in section 5.2.

Table 1.3: Field harmonics integrated strengths on the full magnet, the connector side (CS) and the non-connector side (NC) of the MQXA family of LHC IT Quadrupoles [24]. These are the integrated measurements of the harmonics without the beam screen.

		b_3	b_4	b_5	b_6	b_7	b_8	b_{10}	a_3	a_4	a_5	a_6	a_7	a_8
6677 A (6.8 TeV)	Ave	0.04	1.30	0.00	0.33	0.00	0.02	-0.01	0.21	-0.02	0.01	-0.03	0.00	0.00
	Std	0.31	0.11	0.04	0.09	0.04	0.01	0.01	0.01	0.37	0.28	0.04	0.02	0.01
CS, l=0.34 m	Ave	-0.26	1.17	0.01	-0.54	0.00	–	-0.08	0.24	0.08	0.04	-0.06	0.00	0.00
	Std	1.20	0.14	0.17	0.10	0.02	–	0.01	1.20	0.26	0.14	0.04	0.01	0.01
NC, l=0.62 m	Ave	0.21	2.07	0.05	2.59	-0.01	–	-0.06	0.59	0.04	-0.06	0.09	0.03	0.00
	Std	1.20	0.14	0.17	0.10	0.02	–	0.17	0.01	0.02	0.01	0.01	0.00	1.20

[1] The connectors and non-connector side are also respectively called Lead End (LE) and Return End (RE).

1.2 The High-Luminosity LHC

1.2.1 Presentation of the High-Luminosity upgrade of the LHC

After 10 years of exploitation, the LHC IT magnets need to be replaced. On the other hand, a lot of questions have not been answered yet (New physic, Dark Matter, ...) and some new questions appear (the Higgs size, single or multiple peak, ...). Therefore, it was decided to increase of the Luminosity[1] in order to increase the likelihood to observe rare events, with minimum change to the machine. This upgrade of Luminosity is called High-Luminosity LHC or HL-LHC. If the LHC reach a Luminosity of $150\,\text{fb}^{-1}$ by the end of 2018, this project of upgrade wants to reach $250\,\text{fb}^{-1}$ per years. This implies a peak luminosity of $5 \times 10^{34}\,\text{cm}^{-2}\text{s}^{-1}$ at the experiments.

The luminosity recipe for round beams is given by:

$$L = \frac{n_b N_1 N_2 \gamma f_{rev}}{4\pi\beta^* \epsilon_n} F(\phi, \beta^*, \epsilon, \sigma_s) \tag{1.1}$$

where n_b are the number of bunches, N are the number of proton per bunch, γ is the relativistic factor, f_{rev} is the revolution frequency, β^* is the betatron function at the collision point, ϵ_n is the normalized emittance of the bunches and F is the geometric reduction factor due to the crossing angle. A number of performance optimisation of the LHC complex are required to maximise luminosity:

- maximize bunch intensities
- maximize number of bunches
- minimize the beam emittance
- compensate for 'F'
- minimize beam size at the collision point
- Improve machine 'Efficiency'

The higher bunch intensities and the reduction of emittance will be achieved by the injector complex upgrades, with some limitation on the bunch population due to the longitudinal acceptance of the LHC of bunches that are longitudinally stable in the SPS, at injection [25]. The reduction of the beam sizes at the collision point will be possible thanks to new inner triplet magnets with larger apertures and realized with new Nb_3Sn superconducting cables, instead of NbTi cables used for LHC. The maximum number of bunches is limited to 288 by machine protection considerations for the SPS extraction and injection in the LHC. The compensation for the geometric redaction factor F will be realised installing new equipment in the ring such as the superconducting RF crab cavities [26, 27, 28]. They are deflecting cavity which rotate the beam along the horizontal or vertical axis. In 2018, first beam tests of such crab cavities with protons were successfully performed at the CERN SPS [29]. With all these improvements the instantaneous (or peak) luminosity of about $19 \times 10^{34}\,\text{cm}^{-2}\text{s}^{-1}$ could be achieved, therefore luminosity levelling

[1] The Luminosity is a measure of the number of potential collisions per surface unit over a given period of time. It is an essential indicator of an accelerator's performance and is measured in inverse femtobarns (fb^{-1}), i.e. one inverse femtobarn equates to 100 million million collisions.

techniques will be implemented. The technique of luminosity levelling allows sustaining the operational luminosity, and the associated event pile-up, at a constant level over a significant time by means of several methods:

(i) a gradual reduction of the beta function at the interaction point β^*,

(ii) crossing angle variation,

(iii) changes in the RF voltage of crab cavities or more sophisticated crabbing schemes [30],

(iv) dynamic bunch-length reduction,

(v) controlled variation of the transverse separation between the two colliding beams.

The (i) method require higher beta function in the IR and then a new family of quadrupoles called MQXFS with a bigger physical aperture ($150\,\mathrm{cm}$). In Table 1.4 the beam parameters to obtain such performances are reported.

Table 1.4: Comparison of beam parameters between the LHC and the HL-LHC project.

Parameter	**Nominal LHC design report**	**HL-LHC standard**	**HL-LHC BCMS**
Beam energy in collision [TeV]	7	7	7
Particles per bunch, $N[10^{11}]$	1.15	2.2	2.2
Number of bunches per beam	2808	2748	2604
Beam current [A]	0.58	1.09	1.03
Crossing angle in ATLAS and CMS	285	590	590
Minimum β^* [m]	0.55	0.15	0.15
Levelled luminosity $[10^{34}cm^{-2}s^{-1}]$	-	5.0	5.0
Virtual Luminosity with crab cavity $[10^{34}cm^{-2}s^{-1}]$	(1.18)	19.54	18.52
ϵ_n [μm]	3.75	2.50	2.50
ϵ_L [eVs]	2.50	2.50	2.50
r.m.s. energy spread [0.0001]	1.13	1.13	1.13
r.m.s. bunch length [cm]	7.55	7.55	7.55
Total loss factor R_0 without crab cavity	0.836	0.305	0.305
Total loss factor R_1 with crab cavity	(0.981)	0.829	0.829
Beam-beam/IP without crab cavity	0.0031	0.0033	0.0033
Beam-beam/IP with crab cavity	(0.0038)	0.0011	0.0011
Events/crossing without levelling and crab cavity	(27)	198	198
Events/crossing with levelling and crab cavity	(27)	138	146

1.2.2 The HL-LHC High-Luminosity Interaction Regions and MQXFS Inner Triplet magnets

The main change in the LHC that are relevant for our studies are the one which concern the Interaction Regions. A schematic layout of the very final part of those region is shown in Fig. 1.4. The main differences are:

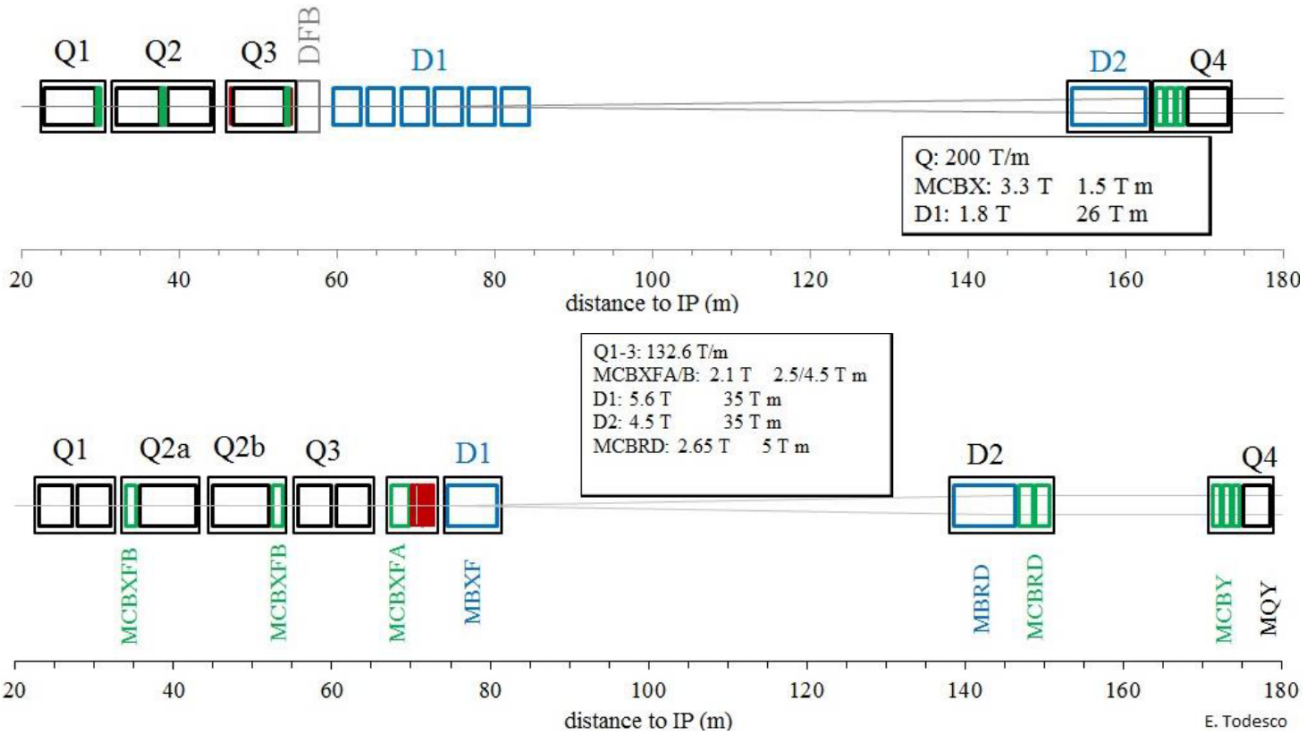

Figure 1.4: Schematic layout of the magnets in the current IR region till Q_4 of the LHC (top) and HL-LHC (bottom). Thick boxes are magnets, thin boxes are cryostats (Ref. [31]).

- Maintain the distance from the first magnet to the collision point at 23 m which imply Increasing the aperture of the Final Focusing quadrupole from 70 mm to 150 mm to allow a smaller β^*;
- Select the Nb_3Sn technology for the quadrupoles, allowing doubling the aperture at constant integrated gradient without a too large increase in the triplet length
- Recover the 10 m of additional space required by the triplet and the correctors, and to gain further space to insert the crab cavities;
- Replace the 20-m-long normal conducting magnet D1 operating at 1.28 T with a superconducting 6.27 m long magnet, operating at 5.6 T, thus recovering $\sim$15 m;
- Increase the apertures of D1 and D2 dipoles and associated correctors: D1 from 60 mm to 150 mm, D2 from 80 mm to 105 mm. For the new dipoles D1 and D2, Nb-Ti superconductor has been chosen;

- A new Non-linear correctors package which correct all the normal and skew harmonics up to the 6 order;
- Add horizontal and vertical orbit correctors close to D2 (not present in the LHC) with a nominal strength of $5\,\mathrm{T/m}$.

Table 1.5: HL-LHC Final Focusing Quadrupoles (MQXSF) main parameters (Ref. [31])

Type	MQXFA	MQXFB
Coil inner diameter	150 mm	150 mm
Magnetic length	4.20 m	7.174 m
Operating temperature	1.9 K	1.9 K
Nominal gradient	132.2 T/m	132.2 T/m
Nominal current	16 230 A	16 230 A
Cable width	18.363 mm	18.363 mm
Mid-thickness in./ou.	1.530/1.658 mm	1.530/1.658 mm
Keystone angle[1]	0.40 deg.	0.40 deg.
No of strands	40	40
Strand diameter	0.850 mm	0.850 mm
Cu/SC Ratio	1.20	1.20

The HL-LHC Inner Triplet magnet of type MQXFS is a family of Quadrupole using Nb_3Sn cables. They can reach higher magnetic field (11-12 T) as report in Tab. 1.5. In this case, the strongest allowed harmonics to take into consideration is the b_6. The values of the integrated harmonics is reported in Table 1.6 and with a longitudinal profile shown in Figure 2.1. The beam screen will also be changed and it's new design will generate a b_6 but since its orientation is not know, it will be ignored for the following studies.

Table 1.6: Estimated of the principal field harmonics in units at 50 mm of the HL-LHC IT Quadrupoles type MQXFS. The beam screen effect has not been taken into consideration (Ref. [25]).

		L [m]	b_3	b_4	b_5	b_6	b_{10}	b_{14}	a_2	a_3	a_4	a_5	a_6	a_{10}	a_{14}
Q1 and Q3	Sys	3.459	0.000	0.000	0.000	0.323	-0.175	-0.856	-2.985	0.000	0.000	0.000	0.210	0.006	-0.021
	U,R		0.820	0.570	0.420	1.100	0.200	0.023	10.000	0.650	0.650	0.430	0.310	0.040	0.005
Q2a and Q2b	Sys	6.409	0.000	0.000	0.000	-0.075	-0.148	-0.862	-1.753	0.000	0.000	0.000	0.124	0.004	-0.012
	U,R		0.820	0.570	0.420	1.100	0.200	0.023	10.000	0.650	0.650	0.430	0.310	0.040	0.005
Connector Side		0.400	0.000	0.000	0.000	8.943	-0.189	-0.545	-31.342	0.000	0.000	0.000	2.209	0.065	-0.222
Non-Connector Side		0.341	0.000	0.000	0.000	-0.025	-0.821	-1.083	0.000	0.000	0.000	0.000	0.000	0.000	0.000

***

Transverse and particularly some Fringe Field beam dynamics have already been made for both accelerators. Nevertheless, as we will see in the next chapter, the definition of the Fringe Field has lost one of its element over the years.

Chapter 2

What do we mean by Fringe Field?

After some discussion with Magnet designers and Beam Dynamic experts, it appears that a nuance in the definition of Fringe Field has disappeared over the many beam dynamics studies. As this can lead to some misunderstanding, it is necessary to clarify what we mean by Fringe Field.

2.1 What are the harmonics used for beam dynamic simulation?

The representation of the magnetic field of the accelerator elements usually takes the following form as a multipole expansion (Ref. [32, 33]):

$$\mathrm{B}_y(x,y,s) + i\mathrm{B}_x(x,y,s) = \sum_{n\in\mathbb{N}} (\ B_{n,c}(s) + iB_{n,s}(s)\ )(\ x+iy\ )^{n-1} \tag{2.1}$$

The transverse magnetic field is decomposed as $B_{n,u}$ with $u \in \{s,c\}$ respectively for normal and skew n^{th}-order harmonics. The order n corresponds to half the number of pole in the equivalent magnet: 1 for Dipole, 2 for Quadrupole, 3 for Sextupole, etc. The same harmonic field components can be measured as Fourier expansion of the radial component of the magnetic field B_ρ, which is usually measured with rotating coils:

$$\mathrm{B}_\rho(\rho,\phi,z) = \sum_{n\in\mathbb{N}} (\ B_{n,c}(z)\cos(n\phi) + B_{n,s}(z)\sin(n\phi)\ )\rho^{n-1} \tag{2.2}$$

In fact, as magnets are not perfect, each magnetic field contains not only the main multipole, for which the magnet is designed, but also other harmonics such as: allowed harmonics (due to the geometry of the magnet) and not-allowed harmonics (due to geometrical errors during its construction). These two last kind of harmonics are called magnetic field errors. In simulation codes, those harmonics are normalized by the reference magnetic field B_{ref} ($B_{ref} = B_{2,s}$ for normal quadrupole) while measured at a reference radius R_{ref} [33]. This reference field is

usually taken in the center of the magnet, where the field is constant. Using the MAD convention[1] [34, 33], those normalized harmonics divided by the accelerator $B\rho_A = P_0c^2$, are noted as b_n for the normal and a_n for the skew harmonics component as in Tab. 1.2 and 1.6:

$$\begin{aligned} \frac{B_{n,c}}{B_{ref}} &= \frac{1}{(n-1)!B_{ref}R_{ref}^{n-1}} \left.\frac{\partial^{n-1}\mathrm{B}_y}{\partial x^{n-1}}\right|_{\rho=R_{ref},s} \\ &= b_n \times 10^{-4} B\rho_A \end{aligned} \qquad \begin{aligned} \frac{B_{n,s}}{B_{ref}} &= \frac{1}{(n-1)!B_{ref}R_{ref}^{n-1}} \left.\frac{\partial^{n-1}\mathrm{B}_x}{\partial x^{n-1}}\right|_{\rho=R_{ref},s} \\ &= a_n \times 10^{-4} B\rho_A \end{aligned} \tag{2.3}$$

In the designing phase of an accelerator, each magnet harmonics is defined by 3 values. These 3 values represent the effect of the magnet manufacturing incertitude on the harmonics: the systematic error $b_{n,S}$, the uncertainty $b_{n,U}$ and the random component $b_{n,R}$ (respectively for the Skew harmonics, Ref. [9]).

$$b_n = b_{n_S} + \frac{\xi_U}{1.5} b_{n_U} + \xi_R b_{n_R} \qquad a_n = a_{n_S} + \frac{\xi_U}{1.5} a_{n_U} + \xi_R a_{n_R} \tag{2.4}$$

where ξ_U is Gaussian distributed random variable cut at $1.5\,\sigma$ for each class of magnet and ξ_R is Gaussian distributed random variable cut at $3\,\sigma$ different for each magnet. Once the magnets are build, the values b_n and a_n can be replaced by the measured ones, as in the LHC [5]. In beam dynamic studies, these harmonics are used to compute the correctors specification (Ref. [9]). They are also used to estimate different configurations of the accelerator for dynamic aperture studies (Ref. [35]).

In reality, those equations (2.3)-(2.4) hide the Fringe Field information. The harmonics are considered constant along the longitudinal axis, either by taking them from the 2D magnetic field simulations or averaged over the whole magnet length, as done for the integrated measurements. The longitudinal distribution of the harmonics for the HLLHC MQXFS, is shown Fig. 2.1 as computed with 3D magnetic field simulations.

2.2 How the definition of Fringe Field has evolved with time?

Since the 1970s, a lot of studies have been made in order to convey the Fringe Field information to beam dynamic studies as shown in Refs. [7, 8]. The Fringe Field of a quadrupole will generate an octupole-like harmonics; for sextupoles, it will be a decapole-like; for octupoles, a dodecapole-like; and so on. In those paper, the Fringe Field definition is reduced to modeling the effect of the longitudinal derivatives of the harmonics (B_z). In MAD-X/PTC [34] for example, this is equivalent to set the flag FRINGE as True.

If this notion is sufficient when considering only the magnet main harmonics, it is not enough to describe the

[1] In order to simplify our calculus, we use the USA convention for n which state that for a dipole $n = 1$ while in the MAD convention $n = 0$.
[2] ρ_A refers to the radius of the accelerator ring, to be distinguished from ρ the radius inside the magnet.

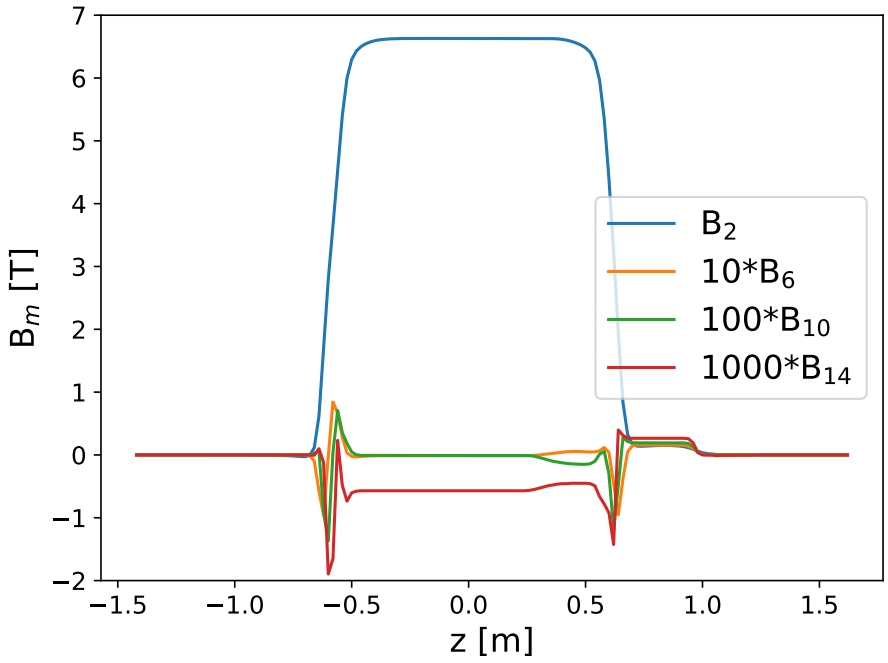

Figure 2.1: Normal harmonics sampled at $\Delta z = 2$mm for the prototype of HL-LHC Inner Triplet quadrupole (MQXFS).

behaviour of the other harmonics, allowed or not. In Ref. [6], H. Wiedemann uses a more global definition by comparing it to the Hard Edge model (i.e. the magnetic field is constant inside and null outside the magnet without any gradient in the transition). He describes the Fringe Field as follows:

> *In reality, however, since nature does not allow sudden changes of physical quantities (natura non facit saltus) the hard edge model is only an approximation, although for practical purposes a rather good one. In a real magnet the field strength does not change suddenly from zero to full value but rather follows a smooth transition from zero to the maximum field. Sometimes, the effects due to this smooth field transition or fringe field are important and [...].*
>
> H. WIEDEMANN, **Particle Accelerator Physics** - p. 119

In fact, the Fourier representation of the other harmonics strengths can change suddenly and greatly (even their signs) in the extremity of the magnet as shown in Fig. 2.1. This comes from the complexity of the structure in its heads, in particular in the connector side. As a quick comparison, this is equivalent to have multipoles in the magnet extremities with strength different from its center. This taken into consideration, studying the Fringe Field consists in considering two notions:

1. the notion of harmonics derivatives (at the order l), i.e. $\partial^l B_{n,u}/\partial z^l$ (with $u \in \{s, c\}$) or B_z.

2. the notion of harmonics longitudinal distribution, i.e. $B_{n,u}(z)$ (with $u \in \{s, c\}$).

Usually, the magnet designers try to reduce those extra harmonics since they are a source of instability in beam dynamics. But, the extremities are very complex to handle, in particular on the connector side. So, they try to compensate non-linearities from one side with the other or with the center. Another important point to consider is the variation of the particle radius from one magnet extremity to the other in region where strong focusing is required (like the LHC interaction region).

2.3 3D vector potential

In order to describe or simulate the particles motion inside an accelerator, the Hamiltonian formalism is widely used with the relation $\frac{\mathrm{d}u}{\mathrm{d}t} = [\mathcal{H}, u] \ \ \forall\, u \in \{Q, P\}$ for any function u of the canonical variables (Q, P) and with the Poisson bracket defined as:

$$[\mathcal{H}, u] = \frac{\partial \mathcal{H}}{\partial P}\frac{\partial u}{\partial Q} - \frac{\partial \mathcal{H}}{\partial Q}\frac{\partial u}{\partial P} \tag{2.5}$$

In the expression of the relativistic Hamiltonian $\mathcal{H}$, the magnetic field is commonly represented in the form of vector potential $\vec{A}$ such as of a charged particle in a electromagnetic field:

$$\mathcal{H} = c\sqrt{(m_p c)^2 + \left\|\vec{P} - q\vec{A}(\vec{Q})\right\|_2^2} + qV \tag{2.6}$$

where q and m_p are respectively the charge and mass of the particle (here a proton), c is the speed of light and V is a scalar potential.

There are many possible representation of the potential vector, like using finite elements as in [36]. [3] is the first record we have found of the computation of the 3D vector potential from the harmonics longitudinal profile, using Generalized Gradient. More details can be found in [37].

Using Maxwell equations, it is known that the magnetic field $\vec{B}$ is related to a scalar potential ψ and the vector potential $\vec{A}$ by the equation $\vec{B} = \nabla\psi = \nabla \times \vec{A}$. From this follows the Laplace equation:

$$\nabla \cdot \vec{B}(\rho, \phi, z) \quad = \nabla^2\psi(\rho, \phi, z) \quad = 0 \tag{2.7}$$

Let's suppose that the scalar potential can be decomposed into 3 distinct functions for each of the cylindrical coordinates, i.e. $\psi(\rho, \phi, z) = R(\rho)P(\phi)Z(z)$. Since we are considering a finite magnet, some boundary conditions have to be taken into consideration such as:

- the scalar potential decrease outside the magnet along the longitudinal axis, i.e. $\lim\limits_{z \to \pm\infty} \psi = const.$,
- the scalar potential is constant at the center of the magnet, i.e. $\left.\frac{\partial \psi}{\partial z}\right|_{z=0} = const.$,

- the scalar potential is 2π-periodic by rotation around the z-axis, i.e. $\psi(\rho, \psi + 2n\pi, z) = \psi(\rho, \psi, z)\ \forall n \in \mathbb{N}$,

- because of the poles symmetry, the scalar potential is null at the center of the magnet, i.e. $\psi|_{\rho=0} = 0$,

It results that equation (2.7) could be transformed into:

$$\nabla^2\psi(\rho,\phi,z) = 0 \quad \Rightarrow \quad \begin{cases} \dfrac{\mathrm{d}^2 Z}{\mathrm{d}z^2} - k^2 Z &= 0 \\ \dfrac{\mathrm{d}^2 P}{\mathrm{d}\phi^2} - n^2 P &= 0 \\ \rho^2 \dfrac{\mathrm{d}^2 R}{\mathrm{d}\rho^2} + \rho \dfrac{\mathrm{d}R}{\mathrm{d}\rho} - \left((k\rho)^2 + n^2\right) R &= 0 \end{cases} \tag{2.8}$$

The solutions to the system (2.8) are proportional to:

$$Z(z) \propto e^{\pm ikz}; \quad P(\phi) \propto e^{\pm in\phi}; \quad R(\rho) \propto I_{\pm n}(k\rho), K_{\pm n}(k\rho) \tag{2.9}$$

where $I_{\pm n}$ and $K_{\pm n}$ respectively the first and second kind modified Bessel functions. Considering that the last boundary condition can't be satisfied by the second kind since $\lim_{k\rho\to 0} K_{\pm n}(k\rho) = \infty$, it can be stated that $R(\rho) \propto I_{\pm n}(k\rho)$. Since $\mathrm{B}_\rho(\rho = R_{ref}, \phi, z)$ is a real number and considering that :

$$\mathrm{B}_\rho(\rho = R_{ref}, \phi, z) \quad = \sum_{n\in\mathbb{N}} B_{n,c}(R_{ref}, z)\cos(n\phi) + B_{n,s}(R_{ref}, z)\sin(n\phi) \quad = \left.\frac{\partial\psi(\rho,\phi,z)}{\partial\rho}\right|_{\rho=R_{ref}} \tag{2.10}$$

it can be assumed that similarly to the magnetic field in Eq. (2.2), the scalar potential can be expressed as:

$$\psi = \sum_{n\in\mathbb{N}} \psi_{n,c}(\rho, z)\cos(n\phi) + \psi_{n,s}(\rho, z)\sin(n\phi) \propto \sum_{n,k\in\mathbb{N}} \Re\left(C_{n,k} I_n(k\rho) e^{i(kz+n\phi)}\right) \tag{2.11}$$

It follows that for $u \in \{s, c\}$.:

$$\tilde{B}_{n,u}(R_{ref}, k) \quad = \quad \frac{1}{\sqrt{2\pi}} \int_{-\infty}^{+\infty} B_{n,u} e^{-ikz}\, \mathrm{d}z \tag{2.12}$$

$$\psi_{n,u}(\rho, z) \quad = \quad \frac{1}{\sqrt{2\pi}} \int_{-\infty}^{+\infty} \frac{I_n(k\rho)}{k I_n'(kR_{ref})} \tilde{B}_{n,u} e^{ikz}\, \mathrm{d}k \tag{2.13}$$

By using $I_n(k\rho)$ Ascending Series into Eq. (2.13) $\left(\text{i.e. } I_n(k\rho) = \sum_{l=0}^{\infty} \frac{1}{l!(l+n)!}\left(\frac{k\rho}{2}\right)^{2l+n}\right)$, the scalar potential harmonics expression becomes:

$$\psi_{n,u}(\rho, z) \quad = \quad \sum_{l=0}^{\infty} \frac{(-1)^l n!}{2^{2l} l!(l+n)!} C_{n,u}^{[2l]}(z) \rho^{2l+n} \tag{2.14}$$

with the Generalized Gradient given by:

$$C^{[l]}_{n,u}(z) \quad = \quad \frac{i^l}{2^n n!}\frac{1}{\sqrt{2\pi}}\int_{-\infty}^{+\infty}\frac{k^{n+l-1}}{I'_n(R_{ref}k)}\tilde{B}_{n,u}(R_{ref},k)e^{ikz}\,\mathrm{d}k \tag{2.15}$$

$C^{[l]}_{n,s}(z)$ and $C^{[l]}_{n,c}(z)$ are respectively called the normal and skew Generalized Gradients. As high order derivatives are fast dumped by the factor $\frac{n!}{2^{2l}l!(l+n)!}$, the sum over l is usually done from 0 to ND, where ND represents the maximum accuracy of the magnetic field reconstruction.

Since $\nabla\times\vec{A}=\nabla\psi$ is the relation between the scalar potential and the vector potential, it leaves the former with a degree of freedom, i.e. a gauge. Defining a vector potential such that $\vec{A}=\vec{A}'+\nabla\lambda$, where λ is an arbitrary scalar, it can be shown that $\nabla\times\vec{A}=\nabla\times\vec{A}'+\nabla\times\nabla\lambda=\nabla\times\vec{A}'$. In this thesis, we will use the Coulomb-free gauge such that $A_\phi=0$ in order to express the theory. On the contrary, we will use the Horizontal Coulomb-free gauge ($A_x=0$) for the simulation. Because it increases the computational speed, without changing the field content (for even numbers of derivatives). The construction of the vector potential from the scalar potential (Eq. (2.13-2.14)) with the Coulomb-free gauge is given by:

$$A_\rho \quad = \quad \sum_{n=1}^{\infty}\rho\frac{\cos(n\phi)}{n}\frac{\partial\psi_{n,s}}{\partial z}-\rho\frac{\sin(n\phi)}{n}\frac{\partial\psi_{n,c}}{\partial z} \tag{2.16}$$

$$A_z \quad = \quad \sum_{n=1}^{\infty}-\rho\frac{\cos(n\phi)}{n}\frac{\partial\psi_{n,s}}{\partial z}+\rho\frac{\sin(n\phi)}{n}\frac{\partial\psi_{n,c}}{\partial z} \tag{2.17}$$

The Generalized Gradients from normal harmonics are noted as $C^{[l]}_{n,s}$ and the ones from the skew harmonics as $C^{[l]}_{n,c}$ with n, the order of the harmonics and $[l]$, the "order" of the longitudinal derivative. The Madx integrated strengths can be related to the Generalized Gradients as follow: $K_{n-1}=\frac{B_{ref}b_n}{B\rho_A}\times10^{-4}=\frac{n}{B\rho_A}\int C^{[0]}_{n,s}(z)\,\mathrm{d}z$ (respectively for the skew).

$$\begin{aligned}A_x(x,y,z) \quad = & \sum_{n}^{\infty}\sum_{l}^{\infty} \quad \frac{(-1)^l(n-1)!}{2^{2l}l!(l+n)!}\left[\sum_{p=0}^{n/2}\sum_{q=0}^{l}\binom{n}{2p}\binom{l}{q}(-1)^p x^{n+2(l-p-q)+1}y^{2(p+q)}C^{[2l+1]}_{n,s}(z)\right.\\ & \left.-\sum_{p=0}^{(n-1)/2}\sum_{q=0}^{l}\binom{n}{2p+1}\binom{l}{q}(-1)^p x^{n+2(l-p-q)}y^{2(p+q)+1}C^{[2l+1]}_{n,c}(z)\right]\end{aligned} \tag{2.18}$$

$$\begin{aligned}A_y(x,y,z) \quad = & \sum_{n}^{\infty}\sum_{l}^{\infty} \quad \frac{(-1)^l(n-1)!}{2^{2l}l!(l+n)!}\left[\sum_{p=0}^{n/2}\sum_{q=0}^{l}\binom{n}{2p}\binom{l}{q}(-1)^p x^{n+2(l-p-q)}y^{2(p+q)+1}C^{[2l+1]}_{n,s}(z)\right.\\ & \left.-\sum_{p=0}^{(n-1)/2}\sum_{q=0}^{l}\binom{n}{2p+1}\binom{l}{q}(-1)^p x^{n+2(l-p-q)-1}y^{2(p+q+1)}C^{[2l+1]}_{n,c}(z)\right]\end{aligned} \tag{2.19}$$

$$A_z(x,y,z) = \sum_{n}^{\infty}\sum_{l}^{\infty} \frac{(-1)^l (n-1)!(2l+n)}{2^{2l} l!(l+n)!} \left[\sum_{p=0}^{n/2}\sum_{q=0}^{l} \binom{n}{2p}\binom{l}{q} (-1)^p x^{n+2(l-p-q)} y^{2(p+q)+1} C_{n,s}^{[2l]}(z) \right.$$
$$\left. - \sum_{p=0}^{(n-1)/2}\sum_{q=0}^{l} \binom{n}{2p+1}\binom{l}{q} (-1)^p x^{n+2(l-p-q)-1} y^{2(p+q)} C_{n,c}^{[2l]}(z) \right] \tag{2.20}$$

***

In this chapter we have reviewed how the magnetic field is decomposed and used for beam dynamic studies. The definition of the notion of Fringe Field is given to show that it is composed of two notions: the derivatives of the multipole harmonics and the longitudinal distribution of the harmonics along the magnet. Expressions (2.18-2.20) give a representation of the Vector Potential as functions of a coefficient C, that depends on z (computed using Eq. (2.15)), and a polynomial in the x and y transverse dimensions. This formalism is suitable for solving the equation of motion in numerical simulations where derivatives/integration of the vector potential are required, as is discussed in the next two chapters.

Chapter 3

Fringe Field Perturbation Theory

Particle motion in accelerators follows Lorentz equations. In storage rings the particle motion in the transverse plane can be modeled by an harmonic oscillator (small oscillation around reference orbit) [6]. Another way to express the particle motion is to consider Hamiltonian mechanics [38]. This allows to easily disentangle the linear and non-linear fields contributions to the particle motion.

The first section reviews some basis of linear beam dynamics and the definition of the Hamiltonian perturbative part. In the second section, the Hamiltonian perturbative part is decomposed into the contribution from the main harmonics and the Fringe Field ones. The case of Octupole, Octupole-like, Dodecapole and Dodecapole-like contributions are detailed. Then, a brief definition of the Lie algebra and the Lie operator are given as well as how they are useful when solving the Hamiltonian equation of motions. This allows us to explain how the contributions from section 3.2 are linked to the Resonance Driving Terms in section 3.4 and the Amplitude Detuning in section 3.5. Then, using the definition of the Resonance Driving Terms, the non-linear variation of the Beta-Beating with the action, called Amplitude Beta-Beating, is derived when computed from the spectral line amplitude. Finally, the limit to observe this latter phenomena is discussed in the last section.

3.1 Linear and non-linear beam dynamics

The description of the path of a charged particle in a magnetic field is usually described with 3 pairs of canonical variables. As shown in Figure 3.1, the coupled coordinates (x, p_x) and (y, p_y) represent the local transverse positions and normalized momenta inside the magnets and (s, δ) represent the curvilinear positions[1] and momenta deviation in the accelerator. In this thesis, we add another couple (z, p_z) to represent the longitudinal position and momenta inside the magnet.

[1] t and s are often used interchangeable in papers. This is the results of a proper change of variable which end-up by dividing by the square of the speed.

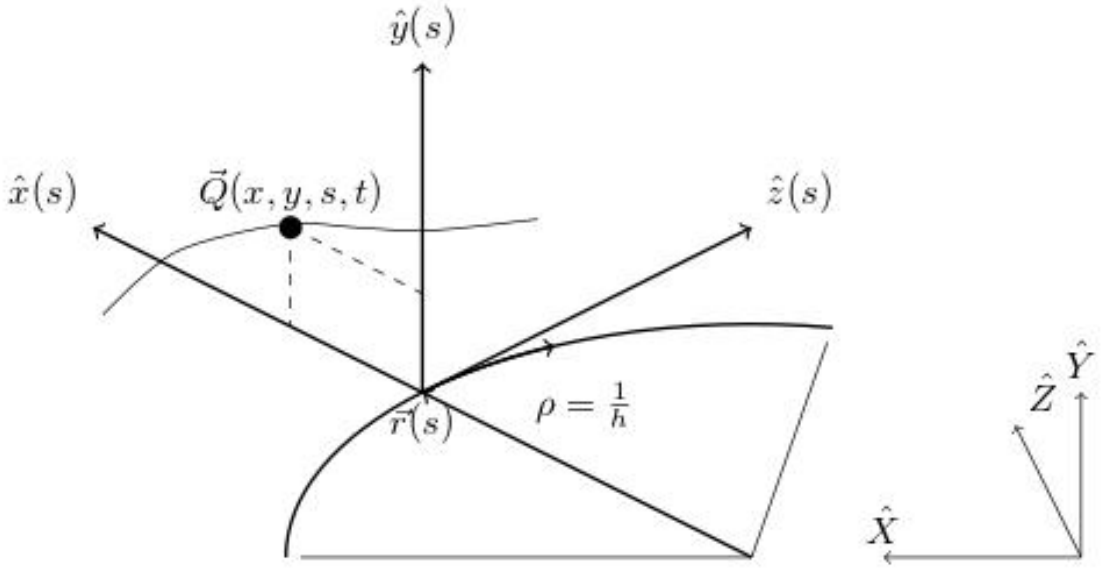

Figure 3.1: Beam trajectory inside an accelerator.

As can be noted in Fig. 3.1, the longitudinal and the curvilinear axes are locally collinear. The particle position is given with respect to a reference particle. This implies that the transverse coordinate can be decomposed into $u = u_c + u_\beta + u_\delta$ for $u \in \{x, y\}$. Here, u_β represents the on momentum motion of the particle around the reference particle. u_c stands for the difference between the reference particle closed orbit and the magnet center. It can create magnetic field feed-down which makes the beam see lower multipoles artificially by polynomial expansion. Meanwhile, u_δ is the impact of the total energy deviation. Similarly, this can generate a chromatic feed-down dependent of this deviation. In the case of the momentum, they are normalized by the total momentum of the reference particle P_0. For the sake of simplicity, let's consider the case with zero dispersion ($u_\delta \approx 0$) and magnet perfectly aligned ($u_c \approx 0$).

When a charged particle moves through a static magnetic field, its path is ruled by the conservation of the relativist Hamiltonian:

$$\mathcal{K}_{6D}[x, p_x, y, p_y, s, \delta|\sigma] = -\sqrt{(1+\delta)^2 - (p_x - a_x)^2 - (p_y - a_y)^2} - a_z \tag{3.1}$$

where σ represents the physical cylindrical slice of the magnet in this context. Similarly to the momentum, the vector potential $\vec{a} = (a_x, a_y, a_z)$ is normalized by $P_0 c/q$ with q the particle charge and c the speed of light. This Hamiltonian could be approximate by a new 8D Hamiltonian using the square root Taylor expansion with the paraxial approximation ($p_z \gg p_x, p_y$), and introducing the longitudinal canonical variables (z, p_z) as shown by Y. K. Wu in [39]:

$$\mathcal{K}_{8D}[x, p_x, y, p_y, z, p_z, s, \delta|\sigma] \quad = \quad \frac{(p_x - a_x)^2}{2(1+\delta)} + \frac{(p_y - a_y)^2}{2(1+\delta)} + \delta + p_z - a_z \tag{3.2}$$

This approximated Hamiltonian can then be decomposed into $\mathcal{K} = \mathcal{H}_0 + \mathcal{H}_p$ where the respective linear and perturbative terms are defined as:

$$\mathcal{H}_0 = \frac{p_x^2}{2(1+\delta)} + \frac{p_y^2}{2(1+\delta)} + \delta + p_z - \frac{1}{2\rho_A^2}x^2 - K_1(x^2 - y^2) \tag{3.3}$$

$$\mathcal{H}_p = -a_z - \frac{p_x a_x + p_y a_y}{(1+\delta)} + \frac{a_x^2 + a_y^2}{2(1+\delta)} \tag{3.4}$$

$\mathcal{H}_0$ describes the linear motion in presence of ideal dipoles and quadrupoles fields (respectively, $1/2\rho_A^2$ an K_1 being their strengths). $\mathcal{H}_p$ describes the motion in presence of realistic magnetic field including non-linear magnetic fields errors (b_n derivatives, b_3, b_4, ...) and deviation from $\mathcal{H}_0$ (Δb_1 and Δb_2).

For now, let's consider only the first term of the Hamiltonian $\mathcal{H}_0$. By using the Hamiltonian mechanic described at the beginning of sec. 2.3, the Hill's differential equations can be derived:

$$0 = \frac{\partial p_x}{\partial s} - [\mathcal{H}_0, x] = \frac{\partial^2 x}{\partial s^2} + \left(\frac{1}{\rho_A^2} + 2K_1\right)x \tag{3.5}$$

$$0 = \frac{\partial p_y}{\partial s} - [\mathcal{H}_0, y] = \frac{\partial^2 y}{\partial s^2} - 2K_1 y \tag{3.6}$$

Assuming that $K = \frac{1}{\rho_A^2} + 2K_1$ or $K = -2K_1$, the Hill's equation can be obtained:

$$0 = \frac{\partial^2 u}{\partial s^2} + Ku \tag{3.7}$$

As the beam pass through the accelerator, it will cross a succession of focusing and defocusing quadrupoles. As it is well known, the solution of Eq.(3.7) is a sum of a sinus and cosinus when $K > 0$ and exponential when $K < 0$. So the beam will be in a oscillating state in both transverse planes. By plotting the transverse momenta as a function of the transverse positions, as shown in Fig. 3.2, the particle describes an ellipse turn after turn.

In their paper [40], E. D. Courant and H. S. Snyder used this approach coupled with the periodicity property of a circular accelerator in order to demonstrate the existence of:

- the Courant-Snyder invariants $2J_u$, also known as Action or Amplitude, which corresponds to the area of the ellipse in Fig. 3.2. They can be obtained using the formula:

$$2J_u = \beta_u(s)p_u^2(s) + 2\alpha_u(s)u(s)p_u(s) + \gamma_u(s)u^2(s) \tag{3.8}$$

- the Twiss Parameters ($\alpha_u(s)$, $\beta_u(s)$ and $\gamma_u(s)$) which characterize the ellipse at a position s in the accelerator,

as shown in Fig. 3.2. They follow the properties:

$$1 = \beta_u(s)\gamma_u(s) - \alpha_u^2(s) \tag{3.9}$$

$$\alpha_u(s) = -\frac{\beta_u'(s)}{2} \tag{3.10}$$

- the phase advance $\mu_u(s) = \Delta\mu_u(s,0)$ between two positions in the accelerator which is given by:

$$\Delta\mu_u(s_1, s_0) = \int_{s_0}^{s_1} \frac{\mathrm{d}s}{\beta_u(s)} \tag{3.11}$$

- the tunes Q_u which is the number of the particle oscillation after one turn (one revolution in the circular accelerator) and which can be obtained with:

$$Q_u = \frac{\mu_u}{2\pi} = \frac{1}{2\pi}\oint \frac{\mathrm{d}s}{\beta_u(s)} \tag{3.12}$$

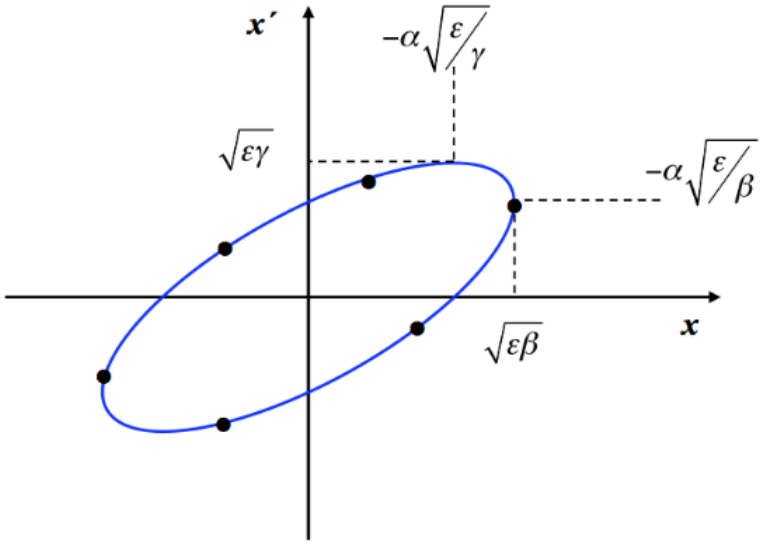

Figure 3.2: Pointcaré section and Twiss parameters, with $x' = p_u$ and $\epsilon = 2J_u$.

We have now the solutions of the Hill's equation which takes the following form at a position s in the accelerator and after N revolutions:

$$u(s) = \sqrt{2J_u\beta_u(s)}\cos(\mu_u N + \mu_u(s)) \tag{3.13}$$

$$p_u(s) = -\sqrt{\frac{2J_u}{\beta_u(s)}}\left[\sin(\mu_u N + \mu_u(s)) + \alpha_u(s)\cos(\mu_u N + \mu_u(s))\right] \tag{3.14}$$

All of this taken into consideration, we can now define a matrix $\mathbf{A}$ defined at a position s. This allows us to transform

from a normalized canonical variable $(\tilde{u}, \tilde{p}_u)$ to the canonical variable (u, p_u).

$$\begin{pmatrix} u \\ p_u \end{pmatrix} = \underbrace{\begin{pmatrix} \beta_u(s)^{1/2} & 0 \\ -\alpha(s)\beta_u(s)^{-1/2} & \beta_u(s)^{-1/2} \end{pmatrix}}_{\mathbf{A}(s)} \begin{pmatrix} \tilde{u} \\ \tilde{p}_u \end{pmatrix} \tag{3.15}$$

3.2 Hamiltonian perturbative terms from the 3D vector potential

Using the Hamiltonian perturbative part given by the expression Eq. (3.4), different contributions can be identified. In order to simplify the following explanation, we consider that the normalized vector potential is expressed in the form $a_u = \sum_n^\infty \sum_l^\infty a_{u;n,l}\ \forall u \in \{x, y, z\}$ with n, the harmonics order and l its derivative order, as seen in Eq. (2.18-2.20). The different contributions can be summarized as:

- $\mathcal{V}_{HE} = \sum_n^\infty a_{z;n,0}$ contains the main harmonics of the magnet. In this regard, the main difference, compared to the previous studies, is that we consider a distribution non-uniform of the harmonics inside the magnet.
- $\mathcal{V}_{FF;pa} = -\sum_n^\infty \sum_{l=0}^\infty \frac{p_x a_{x;n,l} + p_y a_{y;n,l}}{(1+\delta)}$, the momenta multiplied by the transverse vector potential. This vector potential contains the harmonics odd derivatives and so, this Hamiltonian term acts as a $(n+2l+2)$-multipole like.
- $\mathcal{V}_{FF;a_z} = -\sum_n^\infty \sum_{l=1}^\infty a_{z;n,l}$, the harmonics even derivatives in the longitudinal vector potential. This Hamiltonian term acts as a $(n+2l)$-multipole like.
- $\mathcal{V}_{FF;a^2} = \sum_n^\infty \sum_{l=0}^\infty \frac{a_{x;n,l}^2 + a_{y;n,l}^2}{2(1+\delta)}$, the square of the transverse vector potential. This Hamiltonian term acts as a $2(n+l+1)$-multipole like.

Using these definitions, the perturbative part of the Hamiltonian is now decomposed in 4 terms[1]:

$$\mathcal{H}_p = \mathcal{V}_{HE} + \mathcal{V}_{FF;pa} + \mathcal{V}_{FF;a_z} + \mathcal{V}_{FF;a^2} + O(2) \tag{3.16}$$

Now, using Eq. (3.15) and the expression of the vector potential Eq. (2.18-2.20), the different contributions can be expressed as a function of the normalized canonical variables. Those canonical variables can be replaced by the complex Courant-Snyder coordinates $h_{(w),u\pm} = \tilde{u} \pm i\tilde{p}_u = \sqrt{2J_u} e^{\mp i(\mu_u N + \mu_u(w))}$ with $\tilde{u} = (h_{(w),u+} + h_{(w),u-})/2$ and $\tilde{p}_u = i(h_{(w),u-} - h_{(w),u+})/2$. This way, the Hamiltonian perturbative part at a multipole position (w) can be

[1] The last term $O(2)$ is the error term and contains the rest of the Taylor series, among which are the Kinetic terms with $p_x^4 + p_y^4$. But as the subject of this thesis are big hadronic circular accelerators, their contribution are negligible. For these terms, the same following method can also be applied.

expressed as the following sum:

$$\mathcal{H}_p(w) = \sum_{jklm} h_{w,jklm} h^j_{(w),x+} h^k_{(w),x-} h^l_{(w),y+} h^m_{(w),y-} \tag{3.17}$$

All the Hamiltonian terms listed previously ($\mathcal{V}_{HE}$, $\mathcal{V}_{FF;pa}$, etc) add similarly in the $h_{w,jklm}$. Now, as discussed in the previous chapter, the Fringe Field is not only composed of the B_z but also of the longitudinal variation of the harmonics. Which means that the same multipole can have different strength values along the magnet, as the betatronic function.

3.2.1 Normal Octupole perturbative terms

Octupolar contributions to the pertubative Hamiltonian come from normal octupole harmonics and from normal quadrupole harmonics.

- For a normal Octupole (b_4):

  Using Eq. (2.20) and Eq. (3.15), it follows:

$$\begin{aligned}
\mathcal{V}_{HE} &= -a_{z;4,0} \\
&= C^{[0]}_{4,s} \left[x^4 - 6x^2y^2 + y^4\right] &(3.18)\\
&= C^{[0]}_{4,s} \left[\beta_x^2 \tilde{x}^4 - 6\beta_x\beta_y \tilde{x}^2\tilde{y}^2 + \beta_y^2 \tilde{y}^4\right] &(3.19)
\end{aligned}$$

  Then considering that $\tilde{u} = (h_{u-} + h_{u+})/2$, we can develop:

$$\begin{aligned}
\tilde{u}^4 &= \frac{1}{16}\left[h^4_{u-} + 4h^3_{u-}h_{u+} + 6h^2_{u-}h^2_{u+} + 4h_{u-}h^3_{u+} + h^4_{u+}\right] &(3.20)\\
\tilde{x}^2\tilde{y}^2 &= \frac{1}{16}\left[h^2_{x-} + 2h_{x-}h_{x+} + h^2_{x+}\right]\left[h^2_{y-} + 2h_{y-}h_{y+} + h^2_{y+}\right] \\
&= \frac{1}{16}\left[h^2_{x-}h^2_{y-} + 2h_{x-}h_{x+}h^2_{y-} + h^2_{x+}h^2_{y-}\right. \\
&\quad +2h^2_{x-}h_{y-}h_{y+} + 4h_{x-}h_{x+}h_{y-}h_{y+} + 2h^2_{x+}h_{y-}h_{y+} \\
&\quad \left.+h^2_{x-}h^2_{y+} + 2h_{x-}h_{x+}h^2_{y+} + h^2_{x+}h^2_{y+}\right] &(3.21)
\end{aligned}$$

  Combining Eq. (3.19) and Eqs. (3.20-3.21), we obtain the coefficient $h_{w,jklm}$ in Tab. 3.1.

- For the 1^{st} derivative of a normal Quadrupole (b_2):

$$\begin{aligned}
\mathcal{V}_{FF;pa} &= -\frac{p_x a_{x;2,0} + p_y a_{y;2,0}}{1+\delta} \\
&= -\frac{C^{[1]}_{2,s}}{1+\delta}\left[\frac{x^3 p_x}{6} - \frac{x p_x y^2 - x^2 y p_y}{2} - \frac{y^3 p_y}{6}\right] \qquad (3.22)\\
&= -\frac{C^{[1]}_{2,s}}{1+\delta}\left[\frac{\alpha_x\beta_x\tilde{x}^4 - \beta_x\tilde{x}^3\tilde{p}_x}{6} + \frac{(\alpha_y\beta_x - \alpha_x\beta_y)\tilde{x}^2\tilde{y}^2 + \beta_y\tilde{x}\tilde{p}_x\tilde{y}^2 - \beta_x\tilde{x}^2\tilde{y}\tilde{p}_y}{2} - \frac{\alpha_y\beta_y\tilde{y}^4 - \beta_y\tilde{y}^3\tilde{p}_y}{6}\right] \qquad (3.23)
\end{aligned}$$

Now, let's considering that $\tilde{u} = (h_{u-} + h_{u+})/2$ and $\tilde{p}_u = i(h_{(w),u-} - h_{(w),u+})/2$, we can develop:

$$\begin{aligned}
\tilde{u}^3\tilde{p}_u &= \frac{i}{16}\left[h^3_{u-} + 3h^2_{u-}h_{u+} + 3h_{u-}h^2_{u+} + h^3_{u+}\right]\left[h_{u-} - h_{u+}\right] \\
&= \frac{i}{16}\left[h^4_{u-} + 2h^3_{u-}h_{u+} + 0h^2_{u-}h^2_{u+} - 2h_{u-}h^3_{u+} - h^4_{u+}\right] \qquad (3.24)\\
\tilde{x}\tilde{p}_x\tilde{y}^2 &= \frac{i}{16}\left[h^2_{x-} + 0h_{x-}h_{x+} - h^2_{x+}\right]\left[h^2_{y-} + 2h_{y-}h_{y+} + h^2_{y+}\right] \\
&= \frac{i}{16}\left[h^2_{x-}h^2_{y-} + 0h_{x-}h_{x+}h^2_{y-} - h^2_{x+}h^2_{y-}\right. \\
&\qquad +2h^2_{x-}h_{y-}h_{y+} + 0h_{x-}h_{x+}h_{y-}h_{y+} - 2h^2_{x+}h_{y-}h_{y+} \\
&\qquad \left.+h^2_{x-}h^2_{y+} + 0h_{x-}h_{x+}h^2_{y+} - h^2_{x+}h^2_{y+}\right] \qquad (3.25)\\
\tilde{x}^2\tilde{y}\tilde{p}_y &= \frac{i}{16}\left[h^2_{x-} + 2h_{x-}h_{x+} + h^2_{x+}\right]\left[h^2_{y-} + 0h_{y-}h_{y+} - h^2_{y+}\right] \\
&= \frac{i}{16}\left[h^2_{x-}h^2_{y-} + 2h_{x-}h_{x+}h^2_{y-} + h^2_{x+}h^2_{y-}\right. \\
&\qquad +0h^2_{x-}h_{y-}h_{y+} + 0h_{x-}h_{x+}h_{y-}h_{y+} + 0h^2_{x+}h_{y-}h_{y+} \\
&\qquad \left.-h^2_{x-}h^2_{y+} - 2h_{x-}h_{x+}h^2_{y+} - h^2_{x+}h^2_{y+}\right] \qquad (3.26)
\end{aligned}$$

As $up_u = \tilde{u}\tilde{p}_u - \alpha_u\tilde{u}^2$, we can add Eq. (3.20) to Eq. (3.24), and Eq. (3.21) to Eq. (3.25) and (3.26). It follows that:

$$\begin{aligned}
\tilde{u}^3(\tilde{p}_u - \alpha_u\tilde{u}) &= \frac{1}{16}\left[(i-\alpha_u)h^4_{u-} - (2i-4\alpha_u)h^3_{u-}h_{u+} + 6\alpha_u h^2_{u-}h^2_{u+}\right. \\
&\qquad \left.-(2i+4\alpha_u)h_{u-}h^3_{u+} - (i+\alpha_u)h^4_{u+}\right] \qquad (3.27)\\
\tilde{x}\tilde{y}^2(\tilde{p}_x - \alpha_x\tilde{x}) &= \frac{1}{16}\left[(i-\alpha_x)h^2_{x-}h^2_{y-} - 2\alpha_x h_{x-}h_{x+}h^2_{y-} - (i+\alpha_x)h^2_{x+}h^2_{y-}\right. \\
&\qquad +2(i-\alpha_x)h^2_{x-}h_{y-}h_{y+} - 4\alpha_x h_{x-}h_{x+}h_{y-}h_{y+} - 2(i+\alpha_x)h^2_{x+}h_{y-}h_{y+} \\
&\qquad \left.+(i-\alpha_x)h^2_{x-}h^2_{y+} - 2\alpha_x h_{x-}h_{x+}h^2_{y+} - (i+\alpha_x)h^2_{x+}h^2_{y+}\right] \qquad (3.28)\\
\tilde{x}^2\tilde{y}(\tilde{p}_y - \alpha_y\tilde{y}) &= \frac{1}{16}\left[(i-\alpha_y)h^2_{x-}h^2_{y-} + 2(i-\alpha_y)h_{x-}h_{x+}h^2_{y-} + (i-\alpha_y)h^2_{x+}h^2_{y-}\right. \\
&\qquad -2\alpha_y h^2_{x-}h_{y-}h_{y+} - 4\alpha_y h_{x-}h_{x+}h_{y-}h_{y+} - 2y\alpha_y h^2_{x+}h_{y-}h_{y+} \\
&\qquad \left.-(i+\alpha_y)h^2_{x-}h^2_{y+} - 2(i+\alpha_y)h_{x-}h_{x+}h^2_{y+} - (i+\alpha_y)h^2_{x+}h^2_{y+}\right] \qquad (3.29)
\end{aligned}$$

Combining Eq. (3.23) with Eq. (3.27), (3.28) and (3.29), we obtain the coefficient $h_{w,jklm}$ in Tab. 3.1.

- For the 2^{nd} derivative of a normal Quadrupole (b_2):

$$\begin{aligned}\mathcal{V}_{FF;Aa_z} &= -a_{z;2,1} \\ &= -\frac{C_{2,s}^{[2]}}{12}\left[x^4 - y^4\right] \qquad (3.30) \\ &= -\frac{C_{2,s}^{[2]}}{12}\left[\beta_x^2\tilde{x}^4 - \beta_y^2\tilde{y}^4\right] \qquad (3.31)\end{aligned}$$

Following the same procedure of the previous points, we obtain the coefficients $h_{w,jklm}$ in Tab. 3.1.

Table 3.1: Normal Octupole and Octupole-like perturbative terms, computed using the codes in Appendix A.

Magnetic term	$h_{w,jklm}$	Main	Fringe Field	
		$n=4\ ND=0$	$n=2\ ND=1$	$n=2\ ND=2$
$\tilde{x}^4$	$h_{w,4000}$	$C_{4,s}^{[0]}\frac{\beta_x^2}{16}$	$C_{2,s}^{[1]}\frac{\beta_x(\alpha_x - i)}{32(1+\delta)}$	$-C_{2,s}^{[2]}\frac{\beta_x^2}{96}$
$\tilde{x}^3\tilde{p}_x$	$h_{w,3100}$	$C_{4,s}^{[0]}\frac{\beta_x^2}{4}$	$C_{2,s}^{[1]}\frac{\beta_x(2\alpha_x - i)}{16(1+\delta)}$	$-C_{2,s}^{[2]}\frac{\beta_x^2}{24}$
$\tilde{p}_x^4$	$h_{w,2200}$	$3C_{4,s}^{[0]}\frac{\beta_x^2}{8}$	$3C_{2,s}^{[1]}\frac{\beta_x\alpha_x}{16(1+\delta)}$	$-C_{2,s}^{[2]}\frac{\beta_x^2}{16}$
$\tilde{y}^4$	$h_{w,0040}$	$C_{4,s}^{[0]}\frac{\beta_y^2}{16}$	$-C_{2,s}^{[1]}\frac{\beta_y(\alpha_y - i)}{32(1+\delta)}$	$C_{2,s}^{[2]}\frac{\beta_y^2}{96}$
$\tilde{y}^3\tilde{p}_y$	$h_{w,0031}$	$C_{4,s}^{[0]}\frac{\beta_y^2}{4}$	$-C_{2,s}^{[1]}\frac{\beta_y(2\alpha_y - i)}{16(1+\delta)}$	$C_{2,s}^{[2]}\frac{\beta_y^2}{24}$
$\tilde{p}_y^4$	$h_{w,0022}$	$3C_{4,s}^{[0]}\frac{\beta_y^2}{8}$	$-3C_{2,s}^{[1]}\frac{\beta_y\alpha_y}{16(1+\delta)}$	$C_{2,s}^{[2]}\frac{\beta_y^2}{16}$
	$h_{w,2020}$	$-3C_{4,s}^{[0]}\frac{\beta_x\beta_y}{8}$	$C_{2,s}^{[1]}\frac{\beta_x(\alpha_y - i) - \beta_y(\alpha_x - i)}{32(1+\delta)}$	0
$\tilde{x}\tilde{p}_x\tilde{y}^2$	$h_{w,1120}$	$-3C_{4,s}^{[0]}\frac{\beta_x\beta_y}{4}$	$C_{2,s}^{[1]}\frac{\beta_x(\alpha_y - i) - \beta_y\alpha_x}{16(1+\delta)}$	0
$\tilde{x}^2\tilde{y}^2$	$h_{w,0220}$	$-3C_{4,s}^{[0]}\frac{\beta_x\beta_y}{8}$	$C_{2,s}^{[1]}\frac{\beta_x(\alpha_y - i) - \beta_y(\alpha_x + i)}{32(1+\delta)}$	0
$\tilde{x}^2\tilde{y}\tilde{p}_y$	$h_{w,2011}$	$-3C_{4,s}^{[0]}\frac{\beta_x\beta_y}{4}$	$C_{2,s}^{[1]}\frac{\beta_x\alpha_y - \beta_y(\alpha_x - i)}{16(1+\delta)}$	0
	$h_{w,1111}$	$-3C_{4,s}^{[0]}\frac{\beta_x\beta_y}{2}$	$C_{2,s}^{[1]}\frac{\beta_x\alpha_y - \beta_y\alpha_x}{8(1+\delta)}$	0

The formal expression of these terms can be computed by a python code using the sympy library. The main functions are shown in Appendix A. They have been tested by comparing the amplitude detuning terms (see section 3.5) computed with these functions and the one reported in [41], when using the vector potential convention of MadX. These expressions are also the base of the analytical prediction compared in chapter 5 and 6 with tracking simulations.

3.2.2 Normal Dodecapole perturbative terms

Dodecapole contributions to the pertubative Hamiltonian come from normal b_6 harmonics and from normal octupole b_4 harmonics. The third and forth derivatives of the quadrupole harmonics can also generate dodecapole contribution, but they are usually very small.

- For a normal 12-pole (b_6):

$$\mathcal{V}_{HE} = C_{6,s}^{[0]}\left[x^6 - 15x^4y^2 + 15x^2y^4 - y^6\right] \tag{3.32}$$

$$= C_{6,s}^{[0]}\left[\beta_x^3\tilde{x}^6 - 15\beta_x^2\beta_y\tilde{x}^4\tilde{y}^2 + 15\beta_x\beta_y^2\tilde{x}^2\tilde{y}^4 - \beta_y^3\tilde{y}^6\right] \tag{3.33}$$

- For the 1^{st} derivative of a normal octupole (b_4):

$$\mathcal{V}_{FF;pa} = \frac{C_{4,s}^{[1]}}{4(1+\delta)}\left[x^5p_x - 6x^3p_xy^2 + x^4yp_y + xp_xy^4 - 6x^2y^3p_y + y^6\right] \tag{3.34}$$

$$= \frac{C_{4,s}^{[1]}}{4(1+\delta)}\left[\tilde{x}^5(\tilde{p}_x - \alpha_x\tilde{x}) - 6\tilde{x}^3\tilde{y}^2(\tilde{p}_x - \alpha_x\tilde{x}) + \tilde{x}^4\tilde{y}(\tilde{p}_y - \alpha_y\tilde{y})\right.$$
$$\left. + \tilde{x}\tilde{y}^4(\tilde{p}_x - \alpha_x\tilde{x}) - 6\tilde{x}^2\tilde{y}^3(\tilde{p}_y - \alpha_y\tilde{y}) + \tilde{y}^5(\tilde{p}_y - \alpha_y\tilde{y})\right] \tag{3.35}$$

- For the 2^{nd} derivative of a normal octupole (b_4):

$$\mathcal{V}_{FF;a_z} = 3C_{4,s}^{[2]}\left[-\frac{x^6}{40} + \frac{x^4y^2}{8} + \frac{x^2y^4}{8} - \frac{y^6}{40}\right] \tag{3.36}$$

$$= 3C_{4,s}^{[2]}\left[-\frac{\beta_x^3\tilde{x}^6}{40} + \frac{\beta_x^2\beta_y\tilde{x}^4\tilde{y}^2}{8} + \frac{\beta_x\beta_y^2\tilde{x}^2\tilde{y}^4}{8} - \frac{\beta_y^3\tilde{y}^6}{40}\right] \tag{3.37}$$

- For the 1^{st} derivative of a normal quadrupole (b_2):

$$\mathcal{V}_{FF;a^2} = \frac{(C_{2,s}^{[1]})^2}{24(1+\delta)}\left[-x^6 + x^4y^2 - x^2y^4 + y^6\right] \tag{3.38}$$

$$= \frac{(C_{2,s}^{[1]})^2}{24(1+\delta)}\left[-\beta_x^3\tilde{x}^6 + \beta_x^2\beta_y\tilde{x}^4\tilde{y}^2 - \beta_x\beta_y^2\tilde{x}^2\tilde{y}^4 + \beta_y^3\tilde{y}^6\right] \tag{3.39}$$

The different contributions are reported in Table 3.2 also computed with the Python function of Appendix A.

As can be seen in Table 3.1 and 3.2, the Fringe Field contributions add to the same Hamiltonian terms as the main harmonics but with different signs and coefficients. In particular, the derivatives of the main quadrupole field add to the hamiltonian terms excited by the normal octupole. The derivatives of the octupole field components add to the hamiltonians terms excited by the dodecapole field. In certain cases, those terms can be complex.

Table 3.2: Normal dodecapole and dodecapole-like perturbative terms, computed using the codes in Appendix A.

Magnetic term	$h_{w,jklm}$	Main	Fringe Field		
		$n=6\ ND=0$	$n=4\ ND=1$	$n=4\ ND=2$	$n=2\ ND=1$
$\tilde{x}^6$	$h_{w,6000}$	$C_{6,s}^{[0]}\frac{\beta_x^3}{64}$	$C_{4,s}^{[1]}\frac{\beta_x^2(\alpha_x-i)}{256(1+\delta)}$	$-3C_{4,s}^{[2]}\frac{\beta_x^3}{2560}$	$-C_{2,s}^{[1]2}\frac{\beta_x^3}{256(1+\delta)}$
$\tilde{x}^5\tilde{p}_x$	$h_{w,5100}$	$3C_{6,s}^{[0]}\frac{\beta_x^3}{32}$	$C_{4,s}^{[1]}\frac{\beta_x^2(3\alpha_x-2i)}{128(1+\delta)}$	$-9C_{4,s}^{[2]}\frac{3\beta_x^3}{1280}$	$-3C_{2,s}^{[1]2}\frac{\beta_x^3}{128(1+\delta)}$
	$h_{w,4200}$	$15C_{6,s}^{[0]}\frac{\beta_x^3}{64}$	$5C_{4,s}^{[1]}\frac{\beta_x^2(3\alpha_x-i)}{256(1+\delta)}$	$-15C_{4,s}^{[2]}\frac{\beta_x^3}{512}$	$-15C_{2,s}^{[1]2}\frac{\beta_x^3}{256(1+\delta)}$
	$h_{w,3300}$	$5C_{6,s}^{[0]}\frac{\beta_x^3}{16}$	$5C_{4,s}^{[1]}\frac{\beta_x^2\alpha_x}{64(1+\delta)}$	$-3C_{4,s}^{[2]}\frac{\beta_x^3}{128}$	$-5C_{2,s}^{[1]2}\frac{\beta_x^3}{64(1+\delta)}$
$\tilde{x}^4\tilde{y}^2$	$h_{w,4020}$	$-15C_{6,s}^{[0]}\frac{\beta_x^2\beta_y}{64}$	$C_{4,s}^{[1]}\frac{\beta_x^2(\alpha_y-i)-6\beta_x\beta_y(\alpha_x-i)}{256(1+\delta)}$	$C_{4,s}^{[2]}\frac{\beta_x^2\beta_y}{64}$	$C_{2,s}^{[1]2}\frac{\beta_x^2\beta_y}{256(1+\delta)}$
$\tilde{x}^3\tilde{p}_x\tilde{y}^2$	$h_{w,3120}$	$-15C_{6,s}^{[0]}\frac{\beta_x^2\beta_y}{16}$	$C_{4,s}^{[1]}\frac{\beta_x^2(\alpha_y-i)-3\beta_x\beta_y(2\alpha_x-i)}{64(1+\delta)}$	$C_{4,s}^{[2]}\frac{\beta_x^2\beta_y}{16}$	$C_{2,s}^{[1]2}\frac{\beta_x^2\beta_y}{64(1+\delta)}$
$\tilde{x}^4\tilde{y}\tilde{p}_y$	$h_{w,2220}$	$-15C_{6,s}^{[0]}\frac{3\beta_x^2\beta_y}{32}$	$C_{4,s}^{[1]}\frac{3\beta_x^2(\alpha_y-i)-18\beta_x\beta_y\alpha_x}{128(1+\delta)}$	$C_{4,s}^{[2]}\frac{3\beta_x^2\beta_y}{32}$	$C_{2,s}^{[1]2}\frac{\beta_x^2\beta_y}{128(1+\delta)}$
	$h_{w,1320}$	$-15C_{6,s}^{[0]}\frac{\beta_x^2\beta_y}{16}$	$C_{4,s}^{[1]}\frac{\beta_x^2(\alpha_y-i)-3\beta_x\beta_y(2\alpha_x+i)}{64(1+\delta)}$	$C_{4,s}^{[2]}\frac{\beta_x^2\beta_y}{16}$	$C_{2,s}^{[1]2}\frac{\beta_x^2\beta_y}{64(1+\delta)}$
	$h_{w,0420}$	$-15C_{6,s}^{[0]}\frac{\beta_x^2\beta_y}{64}$	$C_{4,s}^{[1]}\frac{\beta_x^2(\alpha_y-i)-6\beta_x\beta_y(\alpha_x+i)}{64(1+\delta)}$	$C_{4,s}^{[2]}\frac{\beta_x^2\beta_y}{64}$	$C_{2,s}^{[1]2}\frac{\beta_x^2\beta_y}{256(1+\delta)}$
	$h_{w,4011}$	$-15C_{6,s}^{[0]}\frac{\beta_x^2\beta_y}{32}$	$C_{4,s}^{[1]}\frac{\beta_x^2\alpha_y-6\beta_x\beta_y(\alpha_x-i)}{128(1+\delta)}$	$C_{4,s}^{[2]}\frac{\beta_x^2\beta_y}{32}$	$C_{2,s}^{[1]2}\frac{\beta_x^2\beta_y}{128(1+\delta)}$
	$h_{w,3111}$	$-15C_{6,s}^{[0]}\frac{\beta_x^2\beta_y}{8}$	$C_{4,s}^{[1]}\frac{\beta_x^2\alpha_y-3\beta_x\beta_y(2\alpha_x-i)}{32(1+\delta)}$	$C_{4,s}^{[2]}\frac{\beta_x^2\beta_y}{8}$	$C_{2,s}^{[1]2}\frac{\beta_x^2\beta_y}{32(1+\delta)}$
	$h_{w,2211}$	$-15C_{6,s}^{[0]}\frac{3\beta_x^2\beta_y}{16}$	$C_{4,s}^{[1]}\frac{3\beta_x^2\alpha_y-18\beta_x\beta_y\alpha_x}{64(1+\delta)}$	$C_{4,s}^{[2]}\frac{3\beta_x^2\beta_y}{16}$	$3C_{2,s}^{[1]2}\frac{\beta_x^2\beta_y}{64(1+\delta)}$
$\tilde{x}^2\tilde{y}^4$	$h_{w,2040}$	$-15C_{6,s}^{[0]}\frac{\beta_x\beta_y^2}{64}$	$C_{4,s}^{[1]}\frac{\beta_y^2(\alpha_x-i)-6\beta_x\beta_y(\alpha_y-i)}{256(1+\delta)}$	$C_{4,s}^{[2]}\frac{\beta_x\beta_y^2}{64}$	$-C_{2,s}^{[1]2}\frac{\beta_x\beta_y^2}{256(1+\delta)}$
$\tilde{x}\tilde{p}_x\tilde{y}^4$	$h_{w,2031}$	$-15C_{6,s}^{[0]}\frac{\beta_x\beta_y^2}{16}$	$C_{4,s}^{[1]}\frac{\beta_y^2(\alpha_x-i)-3\beta_x\beta_y(2\alpha_y-i)}{64(1+\delta)}$	$C_{4,s}^{[2]}\frac{\beta_x\beta_y^2}{16}$	$-C_{2,s}^{[1]2}\frac{\beta_x\beta_y^2}{64(1+\delta)}$
$\tilde{x}^2\tilde{y}\tilde{p}_y^3$	$h_{w,2022}$	$-15C_{6,s}^{[0]}\frac{3\beta_x\beta_y^2}{32}$	$C_{4,s}^{[1]}\frac{3\beta_y^2(\alpha_x-i)-18\beta_x\beta_y\alpha_y}{128(1+\delta)}$	$C_{4,s}^{[2]}\frac{3\beta_x\beta_y^2}{32}$	$C_{2,s}^{[1]2}\frac{\beta_x\beta_y^2}{128(1+\delta)}$
	$h_{w,2013}$	$-15C_{6,s}^{[0]}\frac{\beta_x\beta_y^2}{16}$	$C_{4,s}^{[1]}\frac{\beta_y^2(\alpha_x-i)-3\beta_x\beta_y(2\alpha_y+i)}{64(1+\delta)}$	$C_{4,s}^{[2]}\frac{\beta_x\beta_y^2}{16}$	$-C_{2,s}^{[1]2}\frac{\beta_x\beta_y^2}{64(1+\delta)}$
	$h_{w,2004}$	$-15C_{6,s}^{[0]}\frac{\beta_x\beta_y^2}{64}$	$C_{4,s}^{[1]}\frac{\beta_y^2(\alpha_x-i)-6\beta_x\beta_y(\alpha_y+i)}{64(1+\delta)}$	$C_{4,s}^{[2]}\frac{\beta_x\beta_y^2}{64}$	$-C_{2,s}^{[1]2}\frac{\beta_x\beta_y^2}{256(1+\delta)}$
	$h_{w,1140}$	$-15C_{6,s}^{[0]}\frac{\beta_x\beta_y^2}{32}$	$C_{4,s}^{[1]}\frac{\beta_y^2\alpha_x-6\beta_x\beta_y(\alpha_y-i)}{128(1+\delta)}$	$C_{4,s}^{[2]}\frac{\beta_x\beta_y^2}{32}$	$-C_{2,s}^{[1]2}\frac{\beta_x\beta_y^2}{128(1+\delta)}$
	$h_{w,1131}$	$-15C_{6,s}^{[0]}\frac{\beta_x\beta_y^2}{8}$	$C_{4,s}^{[1]}\frac{\beta_y^2\alpha_x-3\beta_x\beta_y(2\alpha_y-i)}{32(1+\delta)}$	$C_{4,s}^{[2]}\frac{\beta_x\beta_y^2}{8}$	$-C_{2,s}^{[1]2}\frac{\beta_x\beta_y^2}{32(1+\delta)}$
	$h_{w,1122}$	$-15C_{6,s}^{[0]}\frac{3\beta_x\beta_y^2}{16}$	$C_{4,s}^{[1]}\frac{3\beta_y^2\alpha_x-18\beta_x\beta_y\alpha_y}{64(1+\delta)}$	$C_{4,s}^{[2]}\frac{3\beta_x\beta_y^2}{16}$	$-3C_{2,s}^{[1]2}\frac{\beta_x\beta_y^2}{64(1+\delta)}$
$\tilde{y}^6$	$h_{w,0060}$	$C_{6,s}^{[0]}\frac{\beta_y^3}{64}$	$C_{4,s}^{[1]}\frac{\beta_y^2(\alpha_y-i)}{256(1+\delta)}$	$-3C_{4,s}^{[2]}\frac{\beta_y^3}{2560}$	$-C_{2,s}^{[1]2}\frac{\beta_y^3}{256(1+\delta)}$
$\tilde{y}^5\tilde{p}_y$	$h_{w,0051}$	$3C_{6,s}^{[0]}\frac{\beta_y^3}{32}$	$C_{4,s}^{[1]}\frac{\beta_y^2(3\alpha_y-2i)}{128}$	$-9C_{4,s}^{[2]}\frac{3\beta_y^3}{1280}$	$-3C_{2,s}^{[1]2}\frac{\beta_y^3}{128(1+\delta)}$
	$h_{w,0042}$	$15C_{6,s}^{[0]}\frac{\beta_y^3}{64}$	$5C_{4,s}^{[1]}\frac{\beta_y^2(3\alpha_y-i)}{256(1+\delta)}$	$-15C_{4,s}^{[2]}\frac{\beta_y^3}{512}$	$-15C_{2,s}^{[1]2}\frac{\beta_y^3}{256(1+\delta)}$
	$h_{w,0033}$	$5C_{6,s}^{[0]}\frac{\beta_y^3}{16}$	$5C_{4,s}^{[1]}\frac{\beta_y^2\alpha_y}{64(1+\delta)}$	$-3C_{4,s}^{[2]}\frac{\beta_y^3}{128}$	$-5C_{2,s}^{[1]2}\frac{\beta_y^3}{64(1+\delta)}$

3.3 Lie algebra for non-linear beam dynamics

Starting from Eq. (3.13) and Eq. (3.14), which describe the evolution of the trajectory vector from the start of a magnet to a point s, one can also rewrite them in more elegant way in matrix notation. In particular, assuming the

magnetic field of a quadrupole begin and end abruptly at the beginning and end of the magnets, these matrices are (more details are in chapter 4):

$$\begin{pmatrix} x \\ p_x \end{pmatrix}_s = \begin{pmatrix} \cos(\sqrt{k}L) & k^{-1/2}\sin(\sqrt{k}L) \\ -k^{1/2}\sin(\sqrt{k}L) & \cos(\sqrt{k}L) \end{pmatrix} \begin{pmatrix} x \\ p_x \end{pmatrix}_0 \quad \text{if } k > 0 \tag{3.40}$$

$$\begin{pmatrix} x \\ p_x \end{pmatrix}_s = \begin{pmatrix} \cosh(\sqrt{|k|}L) & |k|^{-1/2}\sinh(\sqrt{|k|}L) \\ |k|^{1/2}\sinh(\sqrt{|k|}L) & \cosh(\sqrt{|k|}L) \end{pmatrix} \begin{pmatrix} x \\ p_x \end{pmatrix}_0 \quad \text{if } k < 0 \tag{3.41}$$

Those transformations from a point 0 to a point s are called transfer maps. In this case, these matrices are linear and satisfy the symplecticity condition.

This condition is very important for us, as we study the impact of the 3D vector potential on beam based observable such as the dynamic aperture. Proton beams have a long lifetime, therefore the computation of dynamic aperture usually need to be computed up to 10^5 revolutions in the machine or even more. The symplectic property is a guaranty that total energy of the system is preserved through the transformation.

Definition 3.3.1 (Symplecticity)**.** Let f be a differentiable transformation such that $f(\vec{q},\vec{p}) \ : \ U \longrightarrow \mathbb{R}^{2d}$ with $\vec{q}$ and $\vec{p}$ two canonical vectors of size d in $U \subset \mathbb{R}^{2d}$ an open set. f is symplectic if its Jacobian matrix $\mathbf{J}(\vec{q},\vec{p})$ is symplectic, i.e. if it satisfies:

$$\mathbf{J}(\vec{q},\vec{p})^T \ \mathbf{S} \ \mathbf{J}(\vec{q},\vec{p}) = \mathbf{S} \tag{3.42}$$

with:

$$\mathbf{S} = \begin{pmatrix} 0 & \mathbf{I} \\ -\mathbf{I} & 0 \end{pmatrix} \tag{3.43}$$

In the case of non-linear magnetic field elements, similar transfer matrices are historically derived trough Taylor expansion of the final coordinates at the position s around the initial one [42]:

$$z_{a,s} = K_a + \sum_b R_{ab} z_{b,0} + \sum_{bc} T_{abc} z_{b,0} z_{c,0} + \sum U_{abcd} z_{b,0} z_{c,0} z_{d,0} + \dots \tag{3.44}$$

where $z_{a,s} \in \{x, p_x, \dots\}$ at the position s. The matrix $\mathbf{R}$ is the linear matrix while $\mathbf{T}$ and $\mathbf{U}$ contains the non-linear field treated as aberrations. In general, $\mathbf{T}$ and $\mathbf{U}$ do not satisfy the simplecticity conditions and require a high number of coefficients to be evaluated.

Lie Algebra offers the possibility of both analysing the impact of non-linear magnetic field on a linear optics and computing non-linear transfer maps. Using the same linear vector space as z in our case, the definition of a Lie algebra is:

Definition 3.3.2 (Lie algebra (Ref. [43]))**.** A Lie algebra $\mathbb{A}$ over a field of numbers $\mathbb{F}$ is defined as a linear vector space supplemented by a rule/operator for multiplying two vectors to yield a third vector.

$$\begin{array}{ccc} \mathbb{A} \times \mathbb{A} & \longrightarrow & \mathbb{A} \\ (x \ , \ y) & \longmapsto & x \circ y \end{array} \tag{3.45}$$

The rule is noted as $[x, y] = x \circ y$. In order to be called an algebra, it must follows the following axiom for all $x, y, z \in \mathbb{A}$ and $a, b \in \mathbb{F}$:

1. Bilinearity: $[x + y, z] = [x, z] + [y, z]$, $[x, y + z] = [x, y] + [x, z]$ and $[ax, by] = ab[x, y]$

To be called a Lie algebra, 2 additional axioms must be followed:

2. Anticommutativity: $[x, y] = -[y, x]$

3. The Jacobi identity: $[x, [y, z]] + [z, [x, y]] + [y, [z, x]] = 0$

From a group $(\mathbb{B}, \star)$ with $\mathbb{B}$ a linear vector space and $\star$ an operator, a Lie algebra can easily be build using the operator:

$$[x, y] = x \star y - y \star x \qquad \forall \, x, y \in \mathbb{B} \tag{3.46}$$

A famous example is called the Lie Operator. It is defined as follows given a function of this linear space:

$$: f := \sum_{u \in \{x, y, \dots\}} \frac{\partial f}{\partial p_u} \frac{\partial}{\partial u} - \frac{\partial f}{\partial u} \frac{\partial}{\partial p_u} \tag{3.47}$$

When a differential equation needs to be solved other the same space (such as $\dfrac{\mathrm{d}U}{\mathrm{d}t} = : f : U$), the solution over an interval L is given by the exponentiation of this same operator, also known as Lie Transformation:

$$U|_{t+L} = \mathfrak{M} \, U|_t = e^{\int : f : dt} \, U|_t \tag{3.48}$$

This exponential form has some very useful properties that can be used to simplify the equations. For two function $\mathcal{A}$ and $\mathcal{B}$ and $O(2)$ being the error terms, it follows that:

$$exp(: \mathcal{A} + \mathcal{B} :) = exp(: \mathcal{A} :) exp(: \mathcal{B} :) + O(2) \tag{3.49}$$

$$exp(: \mathcal{A} :) exp(: \mathcal{B} :) = exp(: \mathcal{A} + \mathcal{B} : + O(2)) \tag{3.50}$$

When the exponential form of the Lie operator is applied to a coordinate of the space, it transforms this coordinate according to the system described by the operator $: f :$. It is worth noticing that this coincides with the definition of transfer map.

Our goal here is to describe the motion of a particle through the accelerator. For that, we can solve the differential equation from the Hamiltonian mechanics. These differential equations which rule the motion between those two points of the accelerator are:

$$\frac{\mathrm{d}u}{\mathrm{d}s} \;=\; \frac{\partial \mathcal{H}}{\partial p_u} \qquad , \qquad \frac{\mathrm{d}p_u}{\mathrm{d}s} \;=\; -\frac{\partial \mathcal{H}}{\partial u} \tag{3.51}$$

where u is in $\{x, y, \dots\}$. These equations can be summarized in the following form using the Poison Bracket introduced in Eq. (2.5) and linked to the definition of the Lie operator:

$$\frac{\mathrm{d}u}{\mathrm{d}s} \;=\; [\mathcal{H}, u] \;=: \mathcal{H} : U \qquad \text{for all } \; u \; \text{ in } \; \{x, p_x, y, p_y, \dots\} \tag{3.52}$$

In fact, given the previous definition in Eq. (3.47), the Poisson Bracket is clearly related to the Lie operator, with the Hamiltonian as function f applied to the canonical variable u:

$$: \mathcal{H} := \sum_{u \in \{x, y, \dots\}} \frac{\partial \mathcal{H}}{\partial p_u} \frac{\partial}{\partial u} - \frac{\partial \mathcal{H}}{\partial u} \frac{\partial}{\partial p_u} \tag{3.53}$$

Then, the solution of the Hamiltonian equations over an interval of length L is given by the following equation. If $: \mathcal{H} :$ is s-invariant in this interval, an approximation can also be made:

$$U|_{s+L} \;=\; e^{\int : \mathcal{H} : \, \mathrm{d}s} \, U|_s \;\approx\; e^{L : \mathcal{H} :} \, U|_s \;\approx\; \sum_{k=0}^{\infty} \frac{(L : \mathcal{H} :)^k}{k!} \, U|_s \tag{3.54}$$

with:

$$: \mathcal{H} : U = [\mathcal{H}, U] \tag{3.55}$$

$$: \mathcal{H} :^2 U = [\mathcal{H}, [\mathcal{H}, U]] \tag{3.56}$$

$$\vdots$$

As a side note, if we look back at the expression of the Poisson bracket (Eq. (2.5)) and the Lie Operator (Eq. (3.47), it appears that they can be expressed in a matrix form:

$$: \mathcal{H} : \;=\; -\nabla \mathcal{H} \;\; \mathbf{S} \;\; \nabla \tag{3.57}$$

with $\mathbf{S}$ being the same matrix as the one used for the definition of a symplectic transformation.

Therefore, Lie Algebra and Lie Group transformations provide a tool to generate transfer maps by solving Hamilton equations. These transfer maps are symplectic at any order of the Hamiltonian. In the next section, we discuss how they can help analysing the impact of the perturbative terms of the Hamiltonian on the particle coordinates, while in the next chapter we use them to derive a new non-linear transfer map for tracking simulations.

3.4 Resonance driving terms and spectral lines

As stated in the previous section, one way to solve the Hamiltonian equations between two positions s_1 and s_2 in the accelerator, consists in using a Lie transformation (i.e. a Lie transfer map or Lie map). Let's define a map[1] to transport a particle in a system assuming the Hamiltonian is invariant on this interval:

$$\mathfrak{M}(s_1, s_2) = \exp(: \Delta\sigma\mathcal{H} :) = \sum_k \frac{: \Delta\sigma\mathcal{H} :^k}{k!} \tag{3.58}$$

Here, $\mathcal{H}$ and $\Delta\sigma$ corresponds respectively to the Hamiltonian and the step size between s_1 and s_2. The term $: \Delta\sigma\mathcal{H} :$ is called the Lie Operator and when applied to a canonical variable or function f, it operates as a Poisson Bracket, i.e. $: \Delta\sigma\mathcal{H} : f = \Delta\sigma[\mathcal{H}, f]$. In Section 3.1, it has been shown that a matrix $\mathbf{A}$ exists in linear beam dynamic, which allows the normalisation of the canonical variables into a pure rotation space. In this space, the transfer map of a particle from a position s_1 to s_2 is just a rotation matrix $\mathbf{R}(s_1, s_2)$ in those normalised phase-spaces. Then, in the linear space, the transfer map $\mathfrak{M}$ is a composition of those two matrices, as shown in:

$$\begin{array}{ccccc} & & \mathbf{A}^{-1}(s_1) & & \\ & (u, p_u|s_1) & \longrightarrow & (\tilde{u}, \tilde{p}_u|s_1) & \\ \mathfrak{M}(s_1, s_2) & \downarrow & & \downarrow & \mathbf{R}(s_1, s_2) \\ & (u, p_u|s_2) & \longleftarrow & (\tilde{u}, \tilde{p}_u|s_2) & \\ & & \mathbf{A}(s_2) & & \end{array} \tag{3.59}$$

As discussed in the previous sections, the Hamiltonian is composed of a linear $\mathcal{H}_0$ and a perturbative terms $\mathcal{H}_p$. So, the next step is to check if a similar process can be applied to the motion described by the perturbative part of the Hamiltonian $\mathcal{H}_p$. In [44], E. Forest, M. Berz and J. Irwin demonstrated that a normalization map $\mathfrak{A}(b) = \exp(: \mathcal{F}(b) :)$

[1] More details about the construction of such transfer map are discuss in Sec. 4.3.

exists:

$$\mathfrak{A}^{-1}(b)e^{:\Delta\sigma\mathcal{H}(b):}\mathfrak{A}(b) = e^{:\Delta\sigma\tilde{\mathcal{H}}(b):} \tag{3.60}$$

They show that combinations of the eigenvectors $\xi_{u\pm}^{(b)} = \sqrt{2I_u}\exp(\mp i(\mu_u N + \mu_u(b))$ acts as excited resonances[1]. Those eigenvectors are similar to the complex Courant-Snyder coordinates mentioned in sec. 3.2. The difference is that $2I_u$ is by definition invariant along the accelerator while $2J_u$ is only in the linear case. They also demonstrate that as the perturbative terms of the Hamiltonian is a polynomial using those eigenvectors (see Eq. (3.17)), the normalization map $\mathfrak{A}$ can only be computed using the Hamiltonian terms satisfying:

$$(j-k)Q_x + (l-m)Q_y \neq p \quad \forall\, p \in \mathbb{Z} \tag{3.61}$$

Knowing such constrain, three conditions can be derived:

- Eq. (3.61) is equal to 0. We will note it as $\mathcal{H}_{AD}$ and it contains the Hamiltonian h_{jklm} terms such that $j = k$ and $l = m$. It will be studied in sec. 3.5 for the variation of the tunes with the actions.
- Eq. (3.61) is equal to p, a non-integer. We will note it as $\mathcal{H}_{RDT}$. These terms describe additional Resonance Driving Terms (RDT).
- Eq. (3.61) is equal to p, an integer. We will note it as $\mathcal{H}_R$. It contains the rest of the h_jklm terms, the source of beam instabilities.

The initial Hamiltonian can now be expressed as $\mathcal{H} = \mathcal{H}_0 + \mathcal{H}_p = \mathcal{H}_0 + \mathcal{H}_{AD} + \mathcal{H}_{RDT} + \mathcal{H}_R$ and it becomes $\tilde{\mathcal{H}} = \tilde{\mathcal{H}}_0 + \tilde{\mathcal{H}}_{AD} + \tilde{\mathcal{H}}_R$ in the normalized space. We now need to describe the normalization map $\mathfrak{A}$ with its generating function $\mathcal{F}$.

As mentioned previously, the normalization process presented by E. Forest, M. Berz and J. Irwin introduces new resonances to the trajectory of the particles. In the Poincaré section, this results in a deformation of the ellipse. These resonances linked to the $\mathcal{H}_{RDT}$ term of the Hamiltonian, are used to describe the generating function $\mathcal{F}$. This function is a polynomial of the eigenvectors $\xi_{x\pm}$ and $\xi_{y\pm}$, similar to the perturbative term of the Hamiltonian in Eq. (3.17), the exponents being the same: j, k, l and m. The strength of these resonances computed at a position (b) and excited by multipolar errors at (w), will be noted as $f_{jklm}^{(b)}$. They are given by the following expression, as demonstrate by A. Franchi in [45]:

$$f_{jklm}^{(b)} = \frac{h_{jklm}}{1 - e^{2\pi i[(j-k)Q_x + (l-m)Q_y]}} = \frac{\sum_w h_{w,jklm} e^{i[(j-k)\Delta\mu_x(b,w) + (l-m)\Delta\mu_y(b,w)]}}{1 - e^{2\pi i[(j-k)Q_x + (l-m)Q_y]}} \tag{3.62}$$

[1] To be more general, in [44], the authors consider two kinds of motion: stable and unstable. The eigenvectors mentioned here are for the first kind. For the latter, the complex 'i' have to be removed from the equations.

where $\Delta\mu_u^{(b-w)} = \mu_u^{(b)} - \mu_u^{(w)} \pmod{Q_u}$ is the phase advance between the error source (w) and the position of the observation (b). Using those generating function terms, the expression of the Courant-Snyders variables becomes $h_{u\pm}^{(b)} = \exp(:\mathcal{F}(b):)\xi_{u\pm}^{(b)} = \xi_{u\pm}^{(b)} + [\mathcal{F}(b), \xi_{u\pm}^{(b)}] + O(2)$. That being said, the eigenvectors as the Courant-Snyders variables are not canonical variable. Using a simple change of variable, the Poisson bracket of two generating functions f and g can be expressed with those eigenvectors as:

$$[g,f] = \sum_{u\in\{x,y,z\}} \left(\frac{\partial g}{\partial u}\frac{\partial f}{\partial p_u} - \frac{\partial g}{\partial p_u}\frac{\partial f}{\partial u}\right) = 2i \sum_{u\in\{x,y,z\}} \left(\frac{\partial g}{\partial \xi_{u,+}}\frac{\partial f}{\partial \xi_{u,-}} - \frac{\partial g}{\partial \xi_{u,-}}\frac{\partial f}{\partial \xi_{u,+}}\right) \tag{3.63}$$

As a results, we obtain the Normal Forms described independently in Ref. [44, 46, 47]. The general expression of the complex Phase-Space Courant-Snyder variables at a position (b) and after N revolutions, becomes:

$$h_{x,-}^{(b)} = \sqrt{2I_x}e^{i[\mu_x N+\mu_{x,0}^{(b)}]}\left[1 - 2i\sum_{jklm} j f_{jklm}^{(b)} 2I_x^{\frac{j+k}{2}-1} 2I_y^{\frac{l+m}{2}} e^{i[(k-j)(\mu_x N+\mu_{x,0}^{(b)})+(m-l)(\mu_y N+\mu_{y,0}^{(b)})]}\right] \tag{3.64}$$

$$h_{y,-}^{(b)} = \sqrt{2I_y}e^{i[\mu_y N+\mu_{y,0}^{(b)}]}\left[1 - 2i\sum_{jklm} l f_{jklm}^{(b)} 2I_x^{\frac{j+k}{2}} 2I_y^{\frac{l+m}{2}-1} e^{i[(k-j)(\mu_x N+\mu_{x,0}^{(b)})+(m-l)(\mu_y N+\mu_{y,0}^{(b)})]}\right] \tag{3.65}$$

with the particle action $2I_u$, and $\mu_{u,0}^{(b)}$ the initial phase at the observation position (b).

Since the terms $h_{x,\pm}$ and $h_{y,\pm}$ are a sum of exponential, they are transformed into distinct Dirac in the Fourier space, i.e. spectral line. We will note $H_{h\pm}(n_x, n_y)$ and $V_{h\pm}(n_x, n_y)$ the Fourier Transform of respectively $h_{x,\pm}$ and $h_{y,\pm}$ at a frequency of $n_x Q x + n_y Q_y$. From (3.64) and (3.65), it appears that there is a connection between (j,k,l,m) and (n_x, n_y):

$$H_{h\pm}(n_x, n_y) = H_{h\pm}(1+k-j, m-l) \quad \text{with } j \neq 0 \tag{3.66}$$

$$V_{h\pm}(n_x, n_y) = V_{h\pm}(k-j, 1+m-l) \quad \text{with } l \neq 0 \tag{3.67}$$

So, if n_x and n_y are imposed, we can easily find all the Resonance Driving Terms which sum into the same spectral line, i.e. $j = k + 1 - n_x$ and $l = m - n_y$ for the horizontal plane, and $j = k - n_x$ and $l = m + 1 - n_y$ for the vertical plane. Let's focus on Octupolar field contribution to the main spectral line at the frequency $\pm Q_x$ for the horizontal

plane and $\pm Q_y$ for the vertical plane[1]:

$$H^{(b)}_{h-}(1,0) = \sqrt{2I_x}e^{i\mu^{(b)}_{x,0}} \tag{3.68}$$

$$H^{(b)}_{h-}(-1,0) = -2i\sqrt{2I_x}e^{-i\mu^{(b)}_{x,0}} \sum_{j,l\geqslant 0} (j+2) f^{(b)}_{(j+2)jll} 2I_x^j 2I_y^l \quad \approx -2i\sqrt{2I_x}e^{-i\mu^{(b)}_{x,0}} \left[3f^{(b)}_{3100}2I_x + 2f^{(b)}_{2011}2I_y\right] \tag{3.69}$$

$$V^{(b)}_{h-}(0,1) = \sqrt{2I_y}e^{i\mu^{(b)}_{y,0}} \tag{3.70}$$

$$V^{(b)}_{h-}(0,-1) = -2i\sqrt{2I_y}e^{-i\mu^{(b)}_{y,0}} \sum_{j,l\geqslant 0} (l+2) f^{(b)}_{jj(l+2)l} 2I_x^j 2I_y^l \quad \approx -2i\sqrt{2I_y}e^{-i\mu^{(b)}_{y,0}} \left[3f^{(b)}_{0031}2I_y + 2f^{(b)}_{1120}2I_x\right] \tag{3.71}$$

These expressions shows how the octupole magnetic field acts on the main spectral lines of the tune, when looking at the Fourier Transforms of particles positions at one place in the accelerators (usually measured by turn-by-turn BPMs). These lines are usually used to reconstruct the linear parameters of the accelerator, i.e. the beta-function and the phase. Therefore, in presence of non-linear magnetic field this measurement can be biased, and a dependence on the particle action is expected in the same fashion as the variation of the tune with amplitude.

In the following sections we will derive analytical expressions for the variation of tune and for the variation of the measured beta-function with the amplitude of the particle.

3.5 Amplitude detuning

Following Ref. [41], the Direct and Cross Amplitude Detuning (AD) as a function of the normalized amplitude $2J_u$ ($u \in \{x, y\}$) is given by:

$$\Delta Q_u = \frac{1}{2\pi} \oint \frac{\partial \langle \mathcal{H}_p \rangle}{\partial J_u} \, \mathrm{d}i \tag{3.72}$$

with $\langle \mathcal{H}_p \rangle = \mathcal{H}_{AD}$ since the other terms have 0 average, and i the position along the ring. The curvilinear integral is over one revolution in the accelerator.

In this thesis, the kinematic and second order terms will be neglected. Following Ref. [41], the equations for the

[1] A more detailed expression using for quadrupole, octupole and dodecapole contributions is given in Appendix B.

Direct and Cross Amplitude Detuning for the harmonics b_4 and b_6 are:

$$\begin{aligned}\Delta Q_x &= \frac{q}{2\pi p_0 c}\sum_i \Big[\frac{3}{8}\left(\beta_x^2\bar{b}_4\right)_i(2J_x)+\frac{5}{16}\left(\beta_x^3\bar{b}_6\right)_i(2J_x)^2-\frac{3}{4}\left(\beta_x\beta_y\bar{b}_4\right)_i(2J_y)\\ &\quad+\frac{15}{16}\left(\beta_x\beta_y^2\bar{b}_6\right)_i(2J_y)^2-\frac{15}{8}\left(\beta_x^2\beta_y\bar{b}_6\right)_i(2J_x2J_y)\Big] \qquad (3.73)\\ \Delta Q_y &= \frac{q}{2\pi p_0 c}\sum_i \Big[\frac{3}{8}\left(\beta_y^2\bar{b}_4\right)_i(2J_y)-\frac{5}{16}\left(\beta_y^3\bar{b}_6\right)_i(2J_y)^2\\ &\quad-\frac{3}{4}\left(\beta_x\beta_y\bar{b}_4\right)_i(2J_x)-\frac{15}{16}\left(\beta_x^2\beta_x\bar{b}_6\right)_i(2J_x)^2 \qquad (3.74)\\ &\quad+\frac{15}{8}\left(\beta_x\beta_y^2\bar{b}_6\right)_i(2J_x2J_y)\Big]\end{aligned}$$

where the $\overline{b_n}$ indicates that the relative high order field harmonics are averaged for the positions i belonging to the same element and are kept constant over the length of the magnet. They can be computed with finite element codes or measured with rotating coils. Using Table 3.1 and 3.2, the previous equations can be extended to consider the gradient derivatives and different values for the field harmonics along the same element:

$$\Delta Q_x = \frac{1}{\pi}\sum_{j,l} j h_{jjll}(2J_x)^{j-1}(2J_y)^l \qquad (3.75)$$

$$\begin{aligned}&\underset{j+l<3}{=} \frac{1}{2\pi}\sum_i \Big[\frac{3}{8}\left(4\beta_x^2C_{4,s}^{[0]}+2\beta_x\alpha_xC_{2,s}^{[1]}-\frac{2}{3}\beta_x^2C_{2,s}^{[2]}\right)_i 2J_x\\ &-\frac{3}{4}\left(4\beta_x\beta_yC_{4,s}^{[0]}-\frac{1}{3}(\beta_x\alpha_y-\beta_y\alpha_x)C_{2,s}^{[1]}\right)_i 2J_y\\ &+\frac{5}{16}\left(6\beta_x^3C_{6,s}^{[0]}+\frac{3}{2}\beta_x^2\alpha_xC_{4,s}^{[1]}-\frac{9}{20}\beta_x^3C_{4,s}^{[2]}\right)_i(2J_x)^2 \qquad (3.76)\\ &+\frac{15}{16}\left(6\beta_x\beta_y^2C_{6,ts}^{[0]}+\frac{1}{5}\beta_y\left(\frac{\beta_y\alpha_x}{2}-3\beta_x\alpha_y\right)C_{4,s}^{[1]}+\frac{3}{20}\beta_x\beta_y^2C_{4,s}^{[2]}\right)_i(2J_y)^2\\ &-\frac{15}{8}\left(6\beta_x^2\beta_yC_{6,s}^{[0]}-\frac{1}{5}\beta_x\left(\frac{\beta_x\alpha_y}{2}-3\beta_y\alpha_x\right)C_{4,s}^{[1]}-\frac{3}{20}\beta_x^2\beta_yC_{4,s}^{[2]}\right)_i 2J_x2J_y\Big]\end{aligned}$$

$$\Delta Q_y = \frac{1}{\pi}\sum_{j,l} l h_{jjll}(2J_x)^{j}(2J_y)^{l-1} \qquad (3.77)$$

$$\begin{aligned}&\underset{j+l<3}{=} \frac{1}{2\pi}\sum_i \Big[\frac{3}{8}\left(4\beta_y^2C_{4,s}^{[0]}-2\beta_y\alpha_yC_{2,s}^{[1]}+\frac{2}{3}\beta_y^2C_{2,s}^{[2]}\right)_i 2J_y\\ &-\frac{3}{4}\left(4\beta_x\beta_yC_{4,s}^{[0]}-\frac{1}{3}(\beta_x\alpha_y-\beta_y\alpha_x)C_{2,s}^{[1]}\right)_i 2J_x\\ &-\frac{5}{16}\left(6\beta_y^3C_{6,s}^{[0]}-\frac{3}{2}\beta_y^2\alpha_yC_{4,s}^{[1]}+\frac{9}{20}\beta_y^3C_{4,s}^{[2]}\right)_i(2J_y)^2 \qquad (3.78)\\ &-\frac{15}{16}\left(6\beta_x^2\beta_yC_{6,s}^{[0]}-\frac{1}{5}\beta_x\left(\frac{\beta_x\alpha_y}{2}-3\beta_y\alpha_x\right)C_{4,s}^{[1]}-\frac{3}{20}\beta_x^2\beta_yC_{4,s}^{[2]}\right)_i(2J_x)^2\\ &+\frac{15}{8}\left(6\beta_x\beta_y^2C_{6,s}^{[0]}+\frac{1}{5}\beta_y\left(\frac{\beta_y\alpha_x}{2}-3\beta_x\alpha_y\right)C_{4,s}^{[1]}+\frac{3}{20}\beta_x\beta_y^2C_{4,s}^{[2]}\right)_i 2J_x2J_y\Big]\end{aligned}$$

From these equations, it appears clearly that the non-linearities act on amplitude detuning as weighted sum of the multipolar strengths with the Twiss parameters as weight powers. In regions where those weights can vary inside one magnet and/or have big values, not taking into consideration the longitudinal distribution of the non-linear harmonics can bias the prediction for the detuning with Amplitude.

Equations (3.75) and (3.77) will be used in chapter 5 for the analytical prediction and compared to the fit of numerical data from tracking simulations.

3.6 Non-linear variation of the measured betatronic function when computed from the Amplitude of the main Spectral Line

The Beta-Beating is defined as the variation of the measured betatronic function deviation from nominal values. There are two methods to measure the Betatronic function, either using the phase from the main spectral line between N Beam Position Monitors [48] (BPM) or using the amplitude of the main spectral line at 1 BPM [49]. In this section, the non-linear variation of the amplitude beta-beating measured with the latter method is derived.

The starting hypothesis of this method to measure β_u is that the particle is still in the linear regime, as shown in Sec. 3.1. The turn-by-turn position of the particle can be parametrized as (similarly to Eq. (3.13)):

$$u \approx \sqrt{2J_u\beta_u(s)}\cos(2\pi Q_u N + \mu_u(s)) \tag{3.79}$$

Then, through the Fourier Transform of the particle positions measured at a position (b), it is possible to estimate the horizontal and vertical β-function (respectively $\beta_{x,A}$ and $\beta_{y,A}$). In the linear domain, the following expressions can be derived using the actions and the spectral line at Q_x and Q_y, i.e. $H_x^{(b)}(1,0)$ and $V_y^{(b)}(0,1)$ respectively:

$$\beta_{x,A}(b) \approx \frac{|H_x^{(b)}(1,0)|^2}{2J_x} \approx \beta_x(b)\frac{|H_{\tilde{x}}^{(b)}(1,0)|^2}{2J_x} \qquad \beta_{y,A}(b) \approx \frac{|V_y^{(b)}(0,1)|^2}{2J_y} \approx \beta_y(b)\frac{|V_{\tilde{y}}^{(b)}(0,1)|^2}{2J_y} \tag{3.80}$$

The attentive reader might have noticed that here, the action is noted as $2J_u$ while in the previous section, it was $2I_u$. In fact, one of the prerequisites is to know the action before hand which is not the case, particularly in a non-linear regime of motion. So, they are estimated by computing the average over all the BPMs of the machine:

$$2J_x = \left\langle \frac{|H_x^{(b)}(1,0)|^2}{\beta_{x,P}(b)} \right\rangle_{(b)} \qquad 2J_y = \left\langle \frac{|V_y^{(b)}(0,1)|^2}{\beta_{y,P}(b)} \right\rangle_{(b)} \tag{3.81}$$

with $\beta_{x,P}$ and $\beta_{y,P}$ being the horizontal and vertical β-function from the spectral line phase. This aspect is discussed in more detail in Sec. 3.7. For now on, we consider that $2J_u = 2I_u$.

In the section 3.4, the expression of $h_{x,-}$ and $h_{y,-}$ spectral line at the respective frequency $\pm Q_x$ and $\pm Q_y$ has

been given for Octupolar contributions. Since $\tilde{u} = (h^{(b)}_{u,-} + \overline{h^{(b)}_{u,-}})/2$, the spectral lines of the normalized positions follow:

$$2H^{(b)}_{\tilde{x}}(1,0) = H^{(b)}_{h-}(1,0) + \overline{H^{(b)}_{h-}(-1,0)} \qquad = \sqrt{2I_x}e^{i\mu_x(b)}\left[1 + 6i\overline{f^{(b)}_{3100}}2I_x + 4i\overline{f^{(b)}_{2011}}2I_y\right] \tag{3.82}$$

$$2V^{(b)}_{\tilde{y}}(0,1) = V^{(b)}_{h-}(0,1) + \overline{V^{(b)}_{h-}(0,-1)} \qquad = \sqrt{2I_y}e^{i\mu_y(b)}\left[1 + 6i\overline{f^{(b)}_{0031}}2I_y + 4i\overline{f^{(b)}_{1120}}2I_x\right] \tag{3.83}$$

Let's decompose $f^{(b)}_{jklm}$ into polar coordinates with $q^{(b)}_{jklm}$, its phase and $a^{(b)}_{jklm}$, its amplitude. Using $r = jklm$, it can be demonstrated that:

$$\left|1 + 2i\sum_r a_r e^{-iq_r}\right|^2 = 1 + 4\sum_r a_r \sin(q_r) + 4\sum_r a_r^2 + 8\sum_{r<r'} a_r a_{r'} \cos(q_r - q_{r'}) \tag{3.84}$$

$$= 1 + 4\sum_r \Im\{f_r\} + 4\sum_r a_r^2 + 8\sum_{r<r'} \Re\{f_r\overline{f_{r'}}\} \tag{3.85}$$

Thus, applied to Eqs. (3.82) and (3.83), the Octupolar contributions to the spectral line amplitudes in the normalised space follows:

$$|2H^{(b)}_{\tilde{x}}(1,0)|^2 = 2I_x \quad \Big[1 + 12a^{(b)}_{3100}\sin(q^{(b)}_{3100})(2I_x) + 8a^{(b)}_{2011}\sin(q^{(b)}_{2011})(2I_y) + 36a^{(b)2}_{3100}(2I_x)^2$$
$$+16a^{(b)2}_{2011}(2I_y)^2 + 48a^{(b)}_{3100}a^{(b)}_{2011}\cos(q^{(b)}_{3100} - q^{(b)}_{2011})(2I_x)(2I_y)\Big] \tag{3.86}$$

$$= 2I_x \quad \Xi^{(b)}_x(2I_x, 2I_y) \tag{3.87}$$

$$|2V^{(b)}_{\tilde{y}}(0,1)|^2 = 2I_y \quad \Big[1 + 12a^{(b)}_{0031}\sin(q^{(b)}_{0031})(2I_y) + 8a^{(b)}_{1120}\sin(q^{(b)}_{1120})(2I_x) + 36a^{(b)2}_{0031}(2I_y)^2$$
$$+16a^{(b)2}_{1120}(2I_x)^2 + 48a^{(b)}_{0031}a^{(b)}_{2011}\cos(q^{(b)}_{0031} - q^{(b)}_{1120})(2I_x)(2I_y)\Big] \tag{3.88}$$

$$= 2I_y \quad \Xi^{(b)}_y(2I_x, 2I_y) \tag{3.89}$$

The expressions of $\Xi^{(b)}_u(2I_x, 2I_y) - 1$ correspond to the beta-beating measured from the Amplitude of the main spectral line as a function of the particle actions. We call it Direct and Cross Amplitude Beta-beating (ABB). In chapter 6, simulations are made by exciting f_{3100}, and they are compared to the analytical prediction using $\Xi^{(b)}_x(2I_x, 2I_y) - 1$.

3.7 Discussion about the perturbation of the ABB measurement

The formalism developed in section 3.6 is for a perfect circular accelerator and for only the 1st term of the Taylor series of the Lie algebra (Eq. (11) from [47]). In reality, there are different sources of errors distributed along the accelerator (in particular, b_2, b_4, b_6, beam-beam [50], etc...) and high order Resonance Driving Terms that may impact the Amplitude beta-beating. For example, octupoles second order RDTs generate dodecapole-like RDTs. A

more general expression of the amplitude beta-beating is added in Appendix B.

Precision and accuracy of diagnostic elements can affect the measurement of the Amplitude beta-beating. In [51], it is reported that the BPM Calibration errors apply a factor to the measurement of the particle position. This factor can be estimated using the method from the same paper. $C_u^{(ma,b)}$ and $C_u^{(es,b)}$ represent respectively the actual Calibration factor of the BPM (b) and its estimated value in order to take into account possible errors or deviation with time in the estimation of the Calibration factors.

Another source of discrepancy is the noise in the measurements. As shown in Section 6.2.2, it pollutes all spectral line parameters. This is not negligible in the beta-beating computed from the phase of the main spectral line $\Delta\beta/\beta_{u,P}^{(b)}$ at low actions.

All of those also affect the estimation of the action which is not directly measurable. Following Ref. [51], this estimation is given by:

$$2J_x = \left\langle \frac{|2H_{\tilde{x}}^{(b)}(1,0)|^2}{C_x^{(es,b)}((\Delta\beta/\beta)_{x,P}^{(b)}+1)} \right\rangle_{(b)} = 2I_x \left\langle \frac{C_x^{(ma,b)}}{C_x^{(es,b)}} \frac{\Xi_{\tilde{x}}(2I_x,2I_y)}{((\Delta\beta/\beta)_{x,P}^{(b)}+1)} \right\rangle_{(b)} \tag{3.90}$$

$$2J_y = \left\langle \frac{|2V_{\tilde{y}}^{(b)}(0,1)|^2}{C_y^{(es,b)}((\Delta\beta/\beta)_{y,P}^{(b)}+1)} \right\rangle_{(b)} = 2I_y \left\langle \frac{C_y^{(ma,b)}}{C_y^{(es,b)}} \frac{\Xi_{\tilde{y}}(2I_x,2I_y)}{((\Delta\beta/\beta)_{y,P}^{(b)}+1)} \right\rangle_{(b)} \tag{3.91}$$

All taken into consideration, the actual measurement of the beta-beating from the Amplitude of the main spectral line follows:

$$\left(\frac{\Delta\beta}{\beta}\right)_{u,A}^{(b)} = \frac{2I_u}{2J_u}\frac{C_u^{(ma,b)}}{C_u^{(es,b)}}\Xi_{\check{u}}^{(b)}(2I_x,2I_y) - 1 \tag{3.92}$$

Now, let's make a thought experiment and suppose that at one position of the accelerator, all order of all Resonance Driving Terms are set to zero except $f_{3100}^{(b)}$ responsible for Direct Amplitude beta-beating. As the actions increase, the horizontal beta-beating changes with the actions and this implies that particles ellipse should cross each others. This is what is represented as the $f_{3100}^{(b)}$ case in Fig. 3.3.

In fact, the statement *"all order of all Resonance Driving Terms are set to zero excepts $f_{3100}^{(b)}$"* is partially incorrect. It is still correct to assume that higher order RDTs can be compensated by first order RDTs from higher harmonics, but some RDTs cannot be set to zero. By definition, $f_{3100}^{(b)} = \overline{f_{1300}^{(b)}}$ and this prevent ellipses to cross each other by introducing an action smear.

***

In this chapter, the 3D vector potential expression derived in chapter 2 has been used to compute the terms of the perturbative Hamiltonian that are commonly neglected. These terms add to the same resonances terms generated by normal octupole and dodecapole magnetic field.

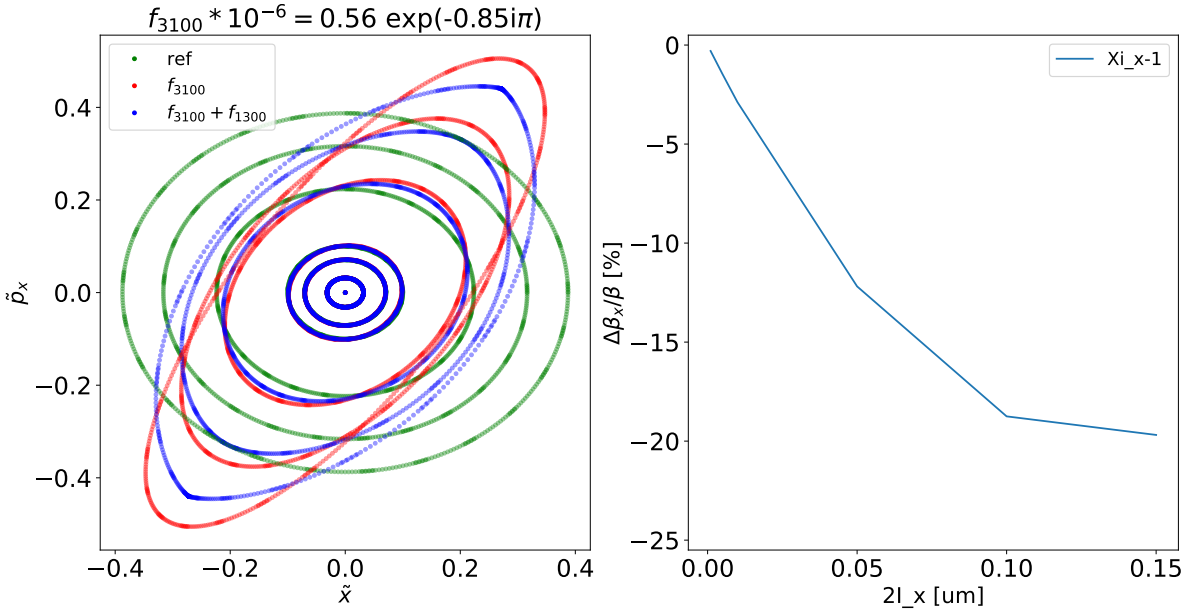

Figure 3.3: The left side shows of the Phase Space, respectively from top to bottom, the perfect linear case (ref), the case with only $f^{(b)}_{3100}$ and with both $f^{(b)}_{3100}$ and $f^{(b)}_{1300}$ in Eq. (3.64). The right side shows the expression of the Direct Amplitude beta-beating Eq. (3.87) for different actions.

The impact of the 3D vector potential on the amplitude detuning is derived analytically. A new quantity is defined as the variation of the beta-function with amplitude, as measured from the amplitude of the main spectral line of Beam Position Monitors. It is called Amplitude Beta-beating.

In the next chapter we will see how the same 3D vector potential can enter in the derivation of a new non-linear transfer map for tracking simulations.

Chapter 4

Transfer Maps models

This chapter describes the different models of Transfer maps that will be compared in this thesis. Each of the next three sections presents what are respectively called Hard Edge, the Hard Edge with Head and the Lie2 models and which effects they can model.

4.1 Definition of the Hard Edge model

As mentioned previously, tracking a particle through a quadrupole end up solving Eq. (3.7). The solution of this ODE is the transfer maps $\mathbf{M}_{HE,Thick}$, also known as Thick lens matrix, computing the particle trajectory from one side to the other of the magnet is:

$$\mathbf{M}_{HE,Thick} = \begin{array}{c} k>0 \\ \left(\begin{array}{cc} \cos(\sqrt{k}L) & k^{-1/2}\sin(\sqrt{k}L) \\ -k^{1/2}\sin(\sqrt{k}L) & \cos(\sqrt{k}L) \end{array} \right) \end{array} \quad \begin{array}{c} k<0 \\ \left(\begin{array}{cc} \cosh(\sqrt{|k|}L) & |k|^{-1/2}\sinh(\sqrt{|k|}L) \\ |k|^{1/2}\sinh(\sqrt{|k|}L) & \cosh(\sqrt{|k|}L) \end{array} \right) \end{array} \tag{4.1}$$

Then, the particles tracking from a position s to $s+L$ is done by $(u, p_u)^T_{s+L} = \mathbf{M}_{HE}\,(u, p_u)^T_s$ with the vector of canonical variables $(u, p_u)^T_s$. As mentioned before, the strength k is consider the same over the whole element magnetic length L. Both of them are symplectic. However, for particle simulations, the computation of the trigonometric and hyperbolic functions is very slow and often replaced by the 1$^{\text{st}}$-order approximation in numerical code. This leads to the following matrix which is not symplectic:

$$\mathbf{M}_{HE,1-oThick} = \begin{pmatrix} 1 & L \\ \pm|k|L & 1 \end{pmatrix} \tag{4.2}$$

Another approach consists in using Thin lens instead, also known as Kick and Drift. As its name suggest, it is

multiplication of two transfer matrices, respectively $\mathbf{K}$ and $\mathbf{D}$. Each of them is symplectic. There are different schools here, either the Kick is between two half Drift, or the inverse or the Kick is followed by a single Drift, respectively:

$$\mathbf{M}_{HE,Thin} = \begin{pmatrix} 1 & L/2 \\ 0 & 1 \end{pmatrix} \begin{pmatrix} 1 & 0 \\ \pm kL & 1 \end{pmatrix} \begin{pmatrix} 1 & L/2 \\ 0 & 1 \end{pmatrix} = \begin{pmatrix} 1 \pm kL^2/2 & L(1 \pm kL^2/4) \\ \pm kL & 1 \pm kL^2/2 \end{pmatrix} \tag{4.3}$$

or

$$\mathbf{M}_{HE,Thin} = \begin{pmatrix} 1 & 0 \\ \pm kL/2 & 1 \end{pmatrix} \begin{pmatrix} 1 & L \\ 0 & 1 \end{pmatrix} \begin{pmatrix} 1 & 0 \\ \pm kL/2 & 1 \end{pmatrix} = \begin{pmatrix} 1 \pm kL^2/2 & L \\ \pm kL(1 \pm kL^2/4) & 1 \pm kL^2/2 \end{pmatrix} \tag{4.4}$$

or

$$\mathbf{M}_{HE,Thin} = \begin{pmatrix} 1 & 0 \\ \pm kL & 1 \end{pmatrix} \begin{pmatrix} 1 & L \\ 0 & 1 \end{pmatrix} = \begin{pmatrix} 1 & L \\ \pm kL & 1 \pm kL^2 \end{pmatrix} \tag{4.5}$$

As can be seen by comparing the Transfer matrices (4.3), (4.4), and (4.5), different transfer maps can be used to describe the same system. In Ref. [1], it is shown that the best way to approximate the Thick matrix with Thin lens is to subdivide the magnet into multiple small Kicks and Drifts with different magnetic lengths (as we move further from the center, the length decrease). In the study, they made the demonstration with the matrix (4.3). The numerical codes Madx/PTC [34] and SixTrack [52], used at CERN for beam dynamic simulations, use the same matrix. For the magnet of interest for this thesis, previous studies at CERN have shown the necessity to use 16 subdivisions with identical magnetic length (see the top panel of Fig. 4.2 at the end of this chapter).

4.2 Definition of the Hard Edge with Head model

A first approach to take into consideration the longitudinal distribution of the harmonics is to add multipole on the two sides of the magnet. With this, the magnet is divided into 3 elements defined as (see the central panel of Fig. 4.2):

- the body, i.e. the section with constant magnetic field along the z-axis, is noted BD;
- the end with the connector[1] side is noted as CS or LE;
- the end with the non-connector side is noted as NC or RE.

The heads (or ends) are defined as $\{z \in \mathbb{R} \ : \ B_z(x,y,z) \neq 0, \ \ \forall \ x,y \in \mathbb{R}\}$ or $\{z \in \mathbb{R} \ : \ A_x(x,y,z) \neq 0$ and/or $A_y(x,y,z) \neq 0, \ \ \forall \ x,y \in \mathbb{R}\}$.

[1] The connector corresponds to the region where the cable separate from the coils and reach the power supplies. The notion of connector side is often used in beam dynamics while for magnet design, it is preferred to speak about Lead and Return End.

In order to have the same integrated harmonics values given by the magnet designers, two conditions must be satisfied. First of all the harmonic strength given to us $b_{n,TT}$ (which is considered as the average value along the magnet) must follows:

$$b_{n,TT} = \frac{b_{n,BD}L_{BD} + b_{n,LE}L_{LE} + b_{n,RE}L_{RE}}{L_{TT}} \tag{4.6}$$

Then, the magnetic length of the whole magnet L_{TT} must be preserved, which lead to:

$$L_{TT} = L_{BD} + L_{LE} + L_{RE} \tag{4.7}$$

In the simulations that will follow, the magnetic lengths of the extremity are computed from the 3D magnetic models. The uncertainty and the random component ($b_{n,u}$ and $b_{n,R}$) of the magnetic field harmonics are considered constant all along the magnet, and assigned completely to the body. The implementation in Madx is made such that the total magnetic length of the element is kept for the body. The body magnetic strength ($b_{n,BD}$) is normalized by L_{BD}/L_{TT} and zero length Kicks are added to the magnet extremities.

4.3 The Lie2 Transfer map

This Lie2 Transfer map and the program computing the vector potential from CERN magnetic field maps were developed at the LEDA laboratory from the CEA. The main goal was to check the impact of non-linear perturbation from z-dependent magnetic field on single particle trajectory.

They are the results of 3 internships and 2 doctorates under the supervision of B. Dalena (CEA, France), J. Payet (CEA, France), O. Napoly (CEA, France) and L. Bonaventura (MOX, Polytechnico di Milano, Italy). The inital step to develop the vector potential computing method from CERN magnetic field maps was made by O. Gabouev. His work were then used and improved in accuracy by A. Simona who develop a C++ algorithm which can compute the vector potential from different type of magnetic field maps [36]. On my side, I developed, optimized and validate the symplecticity of this Lie2 Transfer map which can use the vector potential computed previously. Finally, with the initial help from A. Simona and B. Dalena, we interface our code into SixTrack.

4.3.1 How to generate Transfer Map using Lie algebra.

The Lie2 model developed for this study is derived from the equivalent Hamiltonian (Eq. (3.2)). The Hamiltonian is then divided in 4 terms as follows:

$$\mathcal{K}_{8D}(x, p_x, y, p_x, z, p_z, s, \delta|\sigma) = \underbrace{p_z - \delta}_{\mathcal{K}_1} \underbrace{-a_z}_{\mathcal{K}_2} + \underbrace{\frac{(p_x - a_x)^2}{2(1+\delta)}}_{\mathcal{K}_3} + \underbrace{\frac{(p_y - a_y)^2}{2(1+\delta)}}_{\mathcal{K}_4} \tag{4.8}$$

Using the technique proposed by H. Yoshida in Ref. [53] which demonstrated that $\exp(L:\mathcal{A}+\mathcal{B}:)=\exp(L:\mathcal{A}:)\exp(L:\mathcal{B}:)+O(L^2)$, the operator $\exp(-\Delta\sigma:\mathcal{K}:)$ can be subdivided. However, the terms with $(p_u-a_u)^2$ are problematic since both canonical variables are updated at the same time. To solve this, we need to transform the momenta into mechanical momenta which will be made by $\mathcal{K}_3'=-\int a_x\,\mathrm{d}x$ and $\mathcal{K}_4'=-\int a_y\,\mathrm{d}y$. This leads to the following concatenation of maps:

$$
\begin{aligned}
M(\Delta\sigma) &= \exp(-\Delta\sigma:\mathcal{K}_{8D}:) && (4.9)\\
&= \exp\left(\frac{-\Delta\sigma}{2}:\mathcal{K}_1:\right)\exp\left(-\frac{\Delta\sigma}{2}:\mathcal{K}_2:\right)\exp\left(:\mathcal{K}_3':\right)\exp\left(-\frac{\Delta\sigma}{2}:\mathcal{K}_3:\right)\exp\left(:-\mathcal{K}_3':\right)\\
&\quad \exp\left(:\mathcal{K}_4':\right)\exp\left(-\Delta\sigma:\mathcal{K}_4:\right)\exp\left(:-\mathcal{K}_4':\right)\exp\left(:\mathcal{K}_3':\right)\exp\left(-\frac{\Delta\sigma}{2}:\mathcal{K}_3\right)\exp\left(:-\mathcal{K}_3':\right)\\
&\quad \exp\left(-\frac{\Delta\sigma}{2}:\mathcal{K}_2:\right)\exp\left(-\frac{\Delta\sigma}{2}:\mathcal{K}_1:\right)+O(\Delta\sigma^3) && (4.10)\\
&= M2+O(\Delta\sigma^3) && (4.11)
\end{aligned}
$$

Each Lie transformation modify the canonical pairs as reported in Table 4.1. It can be demonstrated that each

Table 4.1: Non linear transformations of the 2 transverse canonical pairs for the four terms of the quadrupole equivalent Hamiltonian.

	$\exp(:\mathcal{K}_i:)$	x	p_x	y	p_y
$\mathcal{K}_1$	$-\frac{\Delta\sigma}{2}(p_z-\delta)$				
$\mathcal{K}_2$	$\frac{\Delta\sigma}{2}a_z$		$+\frac{\partial a_z}{\partial x}\frac{\Delta\sigma}{2}$		$+\frac{\partial a_z}{\partial y}\frac{\Delta\sigma}{2}$
$\mathcal{K}_3'$	$-\int a_x\,\mathrm{d}x$		$-a_x$		$-\int\frac{\partial a_x}{\partial y}\,\mathrm{d}x$
$\mathcal{K}_3$	$-\frac{\Delta\sigma}{2}\frac{p_x^2}{2(1+\delta)}$	$+\frac{p_x\Delta\sigma}{2(1+\delta)}$			
$-\mathcal{K}_3'$	$\int a_x\,\mathrm{d}x$		$+a_x$		$\int\frac{\partial a_x}{\partial y}\,\mathrm{d}x$
$\mathcal{K}_4'$	$-\int a_y\,\mathrm{d}y$		$-\int\frac{\partial a_y}{\partial x}\,\mathrm{d}x$		$-a_y$
$\mathcal{K}_4$	$-\Delta\sigma\frac{p_y^2}{2(1+\delta)}$			$+\frac{p_y\Delta\sigma}{1+\delta}$	
$-\mathcal{K}_4'$	$\int a_y\,\mathrm{d}y$		$+\int\frac{\partial a_y}{\partial x}\,\mathrm{d}x$		$+a_y$

transfer map corresponding to the terms of this Table is symplectic. In fact, computing the Jacobian of each transfer map leads to: $\mathbf{J}(M)^T\,\mathbf{S}\,\mathbf{J}(M)=\mathbf{S}$.

$$
\mathbf{J}_{\mathcal{K}_1}=\begin{pmatrix}1&0&0&0\\0&1&0&0\\0&0&1&0\\0&0&0&1\end{pmatrix}\qquad
\mathbf{J}_{\mathcal{K}_2}=\begin{pmatrix}1&0&0&0\\0&1&0&0\\\frac{\Delta\sigma}{2}\frac{\partial^2 a_z}{\partial x^2}&\frac{\Delta\sigma}{2}\frac{\partial^2 a_z}{\partial x\partial y}&1&0\\\frac{\Delta\sigma}{2}\frac{\partial^2 a_z}{\partial x\partial y}&\frac{\Delta\sigma}{2}\frac{\partial^2 a_z}{\partial y^2}&0&1\end{pmatrix} \qquad (4.12)
$$

$$\mathbf{J}_{\mathcal{K}_3'} = \begin{pmatrix} 1 & 0 & 0 & 0 \\ 0 & 1 & 0 & 0 \\ \frac{\partial a_x}{\partial x} & \frac{\partial a_x}{\partial y} & 1 & 0 \\ \frac{\partial a_x}{\partial y} & \int \frac{\partial^2 a_x}{\partial y^2}\,\mathrm{d}x & 0 & 1 \end{pmatrix} \qquad \mathbf{J}_{\mathcal{K}_3} = \begin{pmatrix} 1 & 0 & -\frac{\Delta\sigma}{2(1+\delta)} & 0 \\ 0 & 1 & 0 & 0 \\ 0 & 0 & 1 & 0 \\ 0 & 0 & 0 & 1 \end{pmatrix} \tag{4.13}$$

$$\mathbf{J}_{\mathcal{K}_4'} = \begin{pmatrix} 1 & 0 & 0 & 0 \\ 0 & 1 & 0 & 0 \\ \int \frac{\partial^2 a_y}{\partial x^2}\,\mathrm{d}y & \frac{\partial a_y}{\partial x} & 1 & 0 \\ \frac{\partial a_y}{\partial x} & \frac{\partial a_y}{\partial y} & 0 & 1 \end{pmatrix} \qquad \mathbf{J}_{\mathcal{K}_4} = \begin{pmatrix} 1 & 0 & 0 & 0 \\ 0 & 1 & 0 & -\frac{\Delta\sigma}{2(1+\delta)} \\ 0 & 0 & 1 & 0 \\ 0 & 0 & 0 & 1 \end{pmatrix} \tag{4.14}$$

For the moment, we focus only on the transverse canonical pairs. The quadrupole is expected to do not change δ and have a very small effect on s. The final transfer map can be summarised as shown in the scheme of Eq. (4.15):

$$\begin{aligned}
\begin{pmatrix} p_x \\ p_y \end{pmatrix}_{i+1/7} &= \begin{pmatrix} p_x \\ p_y \end{pmatrix}_{i} + \frac{\Delta\sigma}{2} \begin{pmatrix} \frac{\partial a_z\left(x_i, y_i, i\right)}{\partial x} \\ \frac{\partial a_z\left(x_i, y_i, i\right)}{\partial y} \end{pmatrix} - \begin{pmatrix} a_x\left(x_i, y_i, i\right) \\ \int \frac{\partial a_x\left(x_i, y_i, i\right)}{\partial y}\,\mathrm{d}x \end{pmatrix} \\
x_{i+2/7} &= x_{i+1/7} + \frac{\Delta\sigma}{2}\frac{p_{x,i+1/7}}{1+\delta} \\
\begin{pmatrix} p_x \\ p_y \end{pmatrix}_{i+3/7} &= \begin{pmatrix} p_x \\ p_y \end{pmatrix}_{i+2/7} + \begin{pmatrix} a_x\left(x_{i+2/7}, y_{i+2/7}, i\right) \\ \int \frac{\partial a_x\left(x_{i+2/7}, y_{i+2/7}, i\right)}{\partial y}\,\mathrm{d}x \end{pmatrix} - \begin{pmatrix} \int \frac{\partial a_y\left(x_{i+2/7}, y_{i+2/7}, i\right)}{\partial x}\,\mathrm{d}y \\ a_y\left(x_{i+2/7}, y_{i+2/7}, i\right) \end{pmatrix} \\
y_{i+4/7} &= y_{i+3/7} + \Delta\sigma\frac{p_{y,i+3/7}}{1+\delta} \\
\begin{pmatrix} p_x \\ p_y \end{pmatrix}_{i+5/7} &= \begin{pmatrix} p_x \\ p_y \end{pmatrix}_{i+4/7} + \begin{pmatrix} \int \frac{\partial a_y\left(x_{i+4/7}, y_{i+4/7}, i\right)}{\partial y}\,\mathrm{d}x \\ a_y\left(x_{i+4/7}, y_{i+4/7}, i\right) \end{pmatrix} - \begin{pmatrix} a_x\left(x_{i+4/7}, y_{i+4/7}, i\right) \\ \int \frac{\partial a_x\left(x_{i+4/7}, y_{i+4/7}, i\right)}{\partial y}\,\mathrm{d}x \end{pmatrix} \\
x_{i+6/7} &= x_{i+5/7} + \frac{\Delta\sigma}{2}\frac{p_{x,i+5/7}}{1+\delta} \\
\begin{pmatrix} p_x \\ p_y \end{pmatrix}_{i+1} &= \begin{pmatrix} p_x \\ p_y \end{pmatrix}_{i+6/7} + \begin{pmatrix} a_x\left(x_{i+6/7}, y_{i+6/7}, i\right) \\ \int \frac{\partial a_x\left(x_{i+6/7}, y_{i+6/7}, i\right)}{\partial y}\,\mathrm{d}x \end{pmatrix} + \frac{\Delta\sigma}{2} \begin{pmatrix} \frac{\partial a_z\left(x_{i+6/7}, y_{i+6/7}, i\right)}{\partial x} \\ \frac{\partial a_z\left(x_{i+6/7}, y_{i+6/7}, i\right)}{\partial y} \end{pmatrix}
\end{aligned} \tag{4.15}$$

4.3.2 Implementation into SixTrack.

After implementing the integrator from Eq. (4.15), the goal was to patch it into SixTrack without modifying the optics. This Fringe Field module is controlled by the FFIE block. The 4 following subroutine are the main elements for the interface between SixTrack and the code we developed.

- subroutine ffield_parseInputLine(inLine, iLine, iErr):

  This subroutine can be used when the input of SixTrack are read. Using the Keyword FFIE in the input

file fort.3 will automatically prepare our code for the tracking. As shown in Fig. 4.1, it can be followed by 3 flags controlling the Quadrupoles to take into consideration for the study, the multipoles to skip and the files containing the Fringe Field coefficients. The Keyword NEXT delimits the end of the block.

- FFQN quadname in ex

  The FFQN flag selects which quadrupole (name) has a longitudinal description in additional files that will be loaded in the study and links it to the type of Fringe Field that will be used (additional file). Here, quadname is a chain of character corresponding to the name of quadrupole for the Fringe Field study. Those names must be the same as in the single block (SING in fort.2). Following the quadrupole name, two integers (in and ex) correspond to the index of the fringe field file to use respectively at the beginning and end of the quadrupole. Those integers correspond to the order of the Fringe Field files in fort.3 (see FFFI).

- FFMS multname

  The FFMS flag specifies the name of the multipoles to skip in the tracking, in order to not increase the integrated non-linearities if multipole kicks are already added for the quadrupole in the optics definition. We used this flag to remove the additional Kick from the HE+Heads lattice which is replaced by the Lie2 models. Here, multname is a chain of character corresponding to the name of multipole skipped. As previously, the name must be the same as in the single block (SING in fort.2).

- FFFI file length_quad length_tot [aperture]

  The FFFI flag is followed by the files where the different Fringe Field vector potential coefficient are saved. Those coefficient are saved using the format shown in Table 4.2. Here, file corresponds to the path to the fringe field file. length_quad corresponds to the length inside the quadrupole, i.e. integrated magnetic length of the equivalent quadrupole for this file. length_tot corresponds to the Total length of integration inside the file. Those are used to define the longitudinal position of the integrator in the optics definition. Finally, aperture represents the physical aperture of the quadrupole, or the maximum aperture at which you trust the representation of the Vector Potential. This parameter is optional and by default, it is fixed to 0.080 m.

- subroutine ffield_mod_link(iErr):

  If there is the keyword FFIE in fort.3, this subroutine is called. It's goal is to check in the quadrupole and mutlipole selected using the previous procedure exist in the lattice. If the quadrupole is found, then the subroutine ffield_mod_ChckQuad(i,norm,iErr) is called to load the Fringe Field file and normalized the coefficients. The

```
...
NEXT
FFIELD ------------------------------------------------------------
FFQNORMAL    mqxfa.a1l5..1      1      3
FFQNORMAL    mqxfa.b1l5..1      2      4
...
FFMSKIP      mqxfa.b3l5..fl
...
FFFILE    "/afs/cern.ch/user/t/tpugnat/coeffin1.out"     5.91783358704972118e-01    1.420
FFFILE    "/afs/cern.ch/user/t/tpugnat/coeffin2.out"     5.91783358704972118e-01    1.420
FFFILE    "/afs/cern.ch/user/t/tpugnat/coeffout1.out"    6.09915713246783286e-01    1.620
FFFILE    "/afs/cern.ch/user/t/tpugnat/coeffout2.out"    5.71783359230295996e-01    1.420
...
NEXT
...
```

Figure 4.1: Example of keyword command for SixTrack in the input file fort.3.

format of the Fringe Field file lines is specified in Table 4.2.

Arg.	Unit	Description
z	m	Longitudinal position of the kick.
i	–	Exponent of x in the Horner polynomial representation of the vector potential.
j	–	Exponent of y in the Horner polynomial representation of the vector potential.
k	–	Exponent of z in the Horner polynomial representation of the vector potential (0 for quadrupoles).
A_x	$\mathrm{m}^{-(1+\mathrm{i}+\mathrm{j})}$	Coefficient of the Horner polynomial of the vector potential for the axis x (see Eq. (2.18)).
A_y	$\mathrm{m}^{-(1+\mathrm{i}+\mathrm{j})}$	Coefficient of the Horner polynomial of the vector potential for the axis y (see Eq. (2.19)).
A_z	$\mathrm{m}^{-(1+\mathrm{i}+\mathrm{j})}$	Coefficient of the Horner polynomial of the vector potential for the axis z (see Eq. (2.20)).

Table 4.2: Input parameter in the Fringe Field profile files.

- subroutine ffield_enterQuad(ffi) and subroutine ffield_exitQuad(ffi)

  Those last two subroutines are used in SixTrack 6D tracking. The code will automatically detect the beginning and end of the quadrupole and respectively call those subroutines. In order to operate efficiently, the adjacent elements must have a different name!

  The lower frame of Fig. 4.2 schematically represents the process. Once the code detect that the particles are at the beginning of the quadrupole, they are tracked back with an anti-Drift of length length_tot-length_quad. From this point, the particle are tracked with the integrator (4.15) using the vector potential from the file in. Now, the particles are considered inside the quadrupole, so they are tacked back with an anti-Quad computed from the vector potential coefficients. Finally, a Drift of length length_tot-length_quad return the particles to the initial position. Once the particles are at the quadrupole end, the routine is reverse.

  All this process is done in order to not add any extra quadrupolar strength in the optics. Since the anti-quad are δ-dependent, they have been computed for different ranges in $[-\delta, \delta]$ and the adequate matrix is then selected

depending of the particle δ. This was done in order to keep the tracking fast but it is not adapted for multi-type particles tracking that was developed in SixTrack at the end of this thesis.

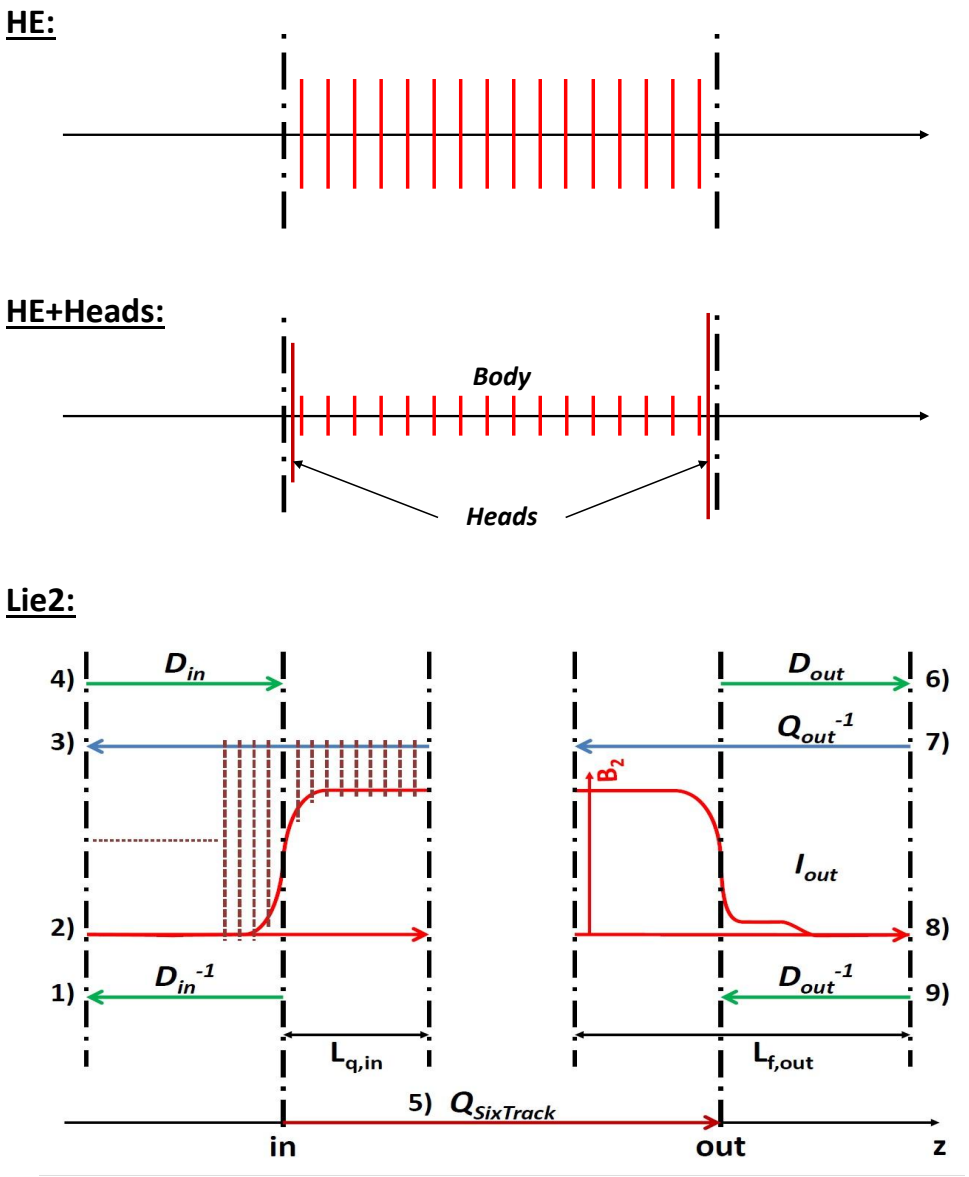

Figure 4.2: Schematic representation of the three models compared in this thesis. HE, HE+Head and Lie2 respectively refer to the Hard Edge, Hard Edge with extra multipole in the magnet ends, and the model develop from the Lie algebra.

***

In this chapter, we have presented a detailed comparison of three different non-linear transfer maps. A graphic representation of these models are represented in Fig. 4.2. The traditional and widely used Hard Hedge model is compared to the Hard Edge + Heads model that introduces in a simplified way the effect of the magnet Fringe Fields.

Finally, a new non-linear transfer map has been derived with the aim to analyse the impact on the particle motion of a more realistic magnetic field description of the magnet ends. In the following three chapters, these three models are used to perform tracking simulations and to compute three different quantities that can also be measured with beam in real accelerators.

Chapter 5

Amplitude detuning and local harmonics correction

In this chapter, the impact of the Fringe Field on the Amplitude Detuning (AD) and its correction will be studied. The AD is a quantity often used during commissioning of the accelerator to quantify the strengths of the higher orders field errors and to derive the correction [5]. The theory behind the AD is described in section 3.5.

In the first section, the prediction for the first and second order amplitude detuning are discussed as well as the non-linear corrector strengths, comparing the 3 models of Chp. 4 for HL-LHC. In the final section, a first attempt to quantify the impact of the longitudinal distribution of the harmonics in LHC is reported.

5.1 HL-LHC first and second order amplitude detuning predictions

In this section, we simulate the particles motion over 10^3 revolutions purely on the vertical or horizontal plane, without the dodecapole correction. The initial positions are set to be below the Dynamic Aperture value (i.e. $0 < 2J_u \leq 0.05\,\mu$m for a normalized emittance of $2.5\,\mu$m), and their initial momentum offset δ is 0. As a comparison, the maximum measured amplitude reached in the LHC is of the order of $0.3\,\mu$m for a β^* of $25\,$cm (see Ref. [54, 55, 5]).

For the sake of the graphic visibility, the b_4 multipole error components have been removed from the simulation. And the linear amplitude detuning from the main sextupole second order has been subtracted in the AD using the linear coefficient C1 (about $1.8 \pm 0.1 \times 10^{-2}\,\mu\text{m}^{-1}$ and $1.75 \pm 0.1 \times 10^{-2}\,\mu\text{m}^{-1}$, in the x and y-planes respectively) compatible with the 1^{st} order anharmonicity given by MADX PTC (Ref. [34]).

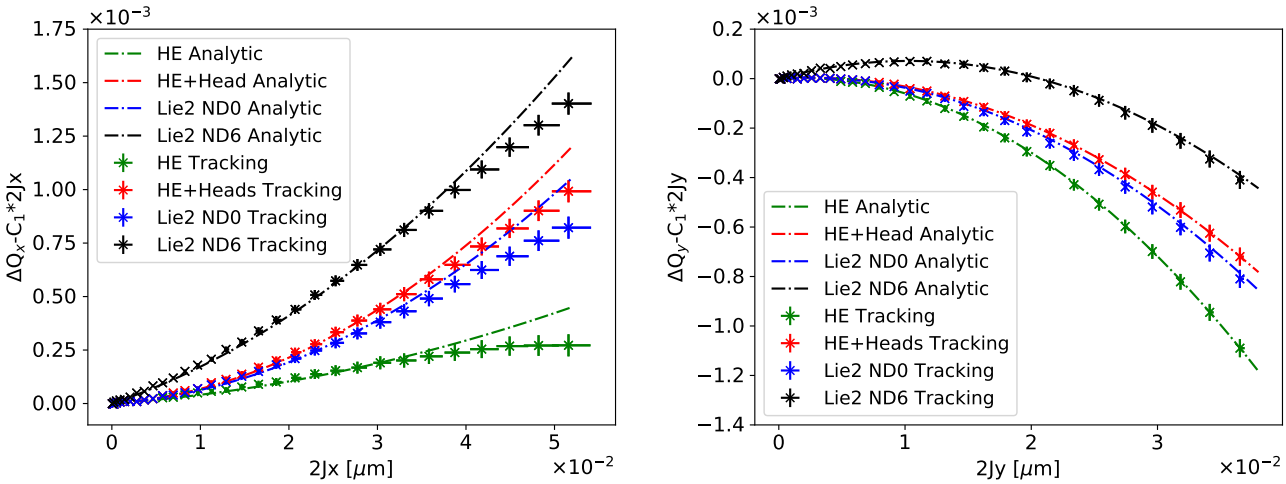

Figure 5.1: Amplitude detuning for the horizontal (left) and the vertical plane (right).

5.1.1 Amplitude detuning with all the harmonics

Figure 5.1 shows the simulated Amplitude Detuning in both planes with all the non-linear errors (except for b_4) for all the models. The horizontal error bars correspond to the minimum and maximum amplitude over the 10^3 revolutions and are centered on the initial amplitude. The vertical error bars correspond to the uncertainty of the correction for linear detuning due to second order effects from main sextupoles. Table 5.1 shows the fitted values with respect to the predicted ones. For each model, the simulated AD is compared to the theoretical AD from equations (3.75) and (3.77). The simulated detuning with amplitude is fitted with a 4$^{\text{th}}$ order polynomial (motivated by using smallest degree for the best score, and its robustness over fitting procedures).

Table 5.1: Amplitude detuning coefficients from Fig. 5.1 fitted with a 4^{th}-order polynomial and for an Amplitude in μm.

	Fit		Analytical	
Case	$\partial Q_x/\partial(2J_x)$	$\partial^2 Q_x/\partial(2J_x)^2$	$\partial Q_x/\partial(2J_x)$	$\partial^2 Q_x/\partial(2J_x)^2$
HE	$(0.1 \pm 0.3) \times 10^{-3}$	0.08 ± 0.03	0	0.11
HE+Heads	$(0.1 \pm 0.4) \times 10^{-3}$	0.38 ± 0.03	0	0.39
Lie2 ND0	$(0.9 \pm 0.4) \times 10^{-3}$	0.22 ± 0.03	0	0.33
Lie2 ND6	$(9.2 \pm 0.4) \times 10^{-3}$	0.25 ± 0.03	10.9×10^{-3}	0.33
Case	$\partial Q_y/\partial(2J_y)$	$\partial^2 Q_y/\partial(2J_y)^2$	$\partial Q_y/\partial(2J_y)$	$\partial^2 Q_y/\partial(2J_y)^2$
HE	$(0.2 \pm 0.4) \times 10^{-3}$	-0.98 ± 0.05	0	-0.90
HE+Heads	$(0.0 \pm 0.4) \times 10^{-3}$	-0.63 ± 0.05	0	-0.62
Lie2 ND0	$(0.4 \pm 0.5) \times 10^{-3}$	-0.79 ± 0.06	0	-0.67
Lie2 ND6	$(10.7 \pm 0.4) \times 10^{-3}$	-0.67 ± 0.05	10.9×10^{-3}	-0.67

It appears clearly in Fig. 5.1 and Tab. 5.1 that the Amplitude Detuning is sensible to the longitudinal distribution of the harmonics in the magnet, i.e. the model. This is also confirmed by the fact that the simulations agree well with the analytical prediction up to an amplitude of $\sim 3.0 \times 10^{-2}\,\mu$m.

The good agreement between the HE+Heads and the Lie2 ND0 model shows that one additional kick in each of the extremity gives a good approximation of the longitudinal distribution of the expected non-linearities. Nevertheless, the Lie2 model yields the best representation, if accuracy is more important than computational cost.

The discrepancy between the Lie2 models with and without derivatives (ND0 and ND6, respectively) shows an additional linear detuning generated by the 1^{st} and 2^{nd} derivatives of the b_2 harmonics, as expected from equations (3.75) and (3.77). We just note that this effect is of the same order as the effect due to the 2nd-order Sextupoles for the ATS optics [56] with 15 cm β^*, foreseen for HL-LHC project.

5.1.2 Amplitude detuning for only the b_6 harmonics

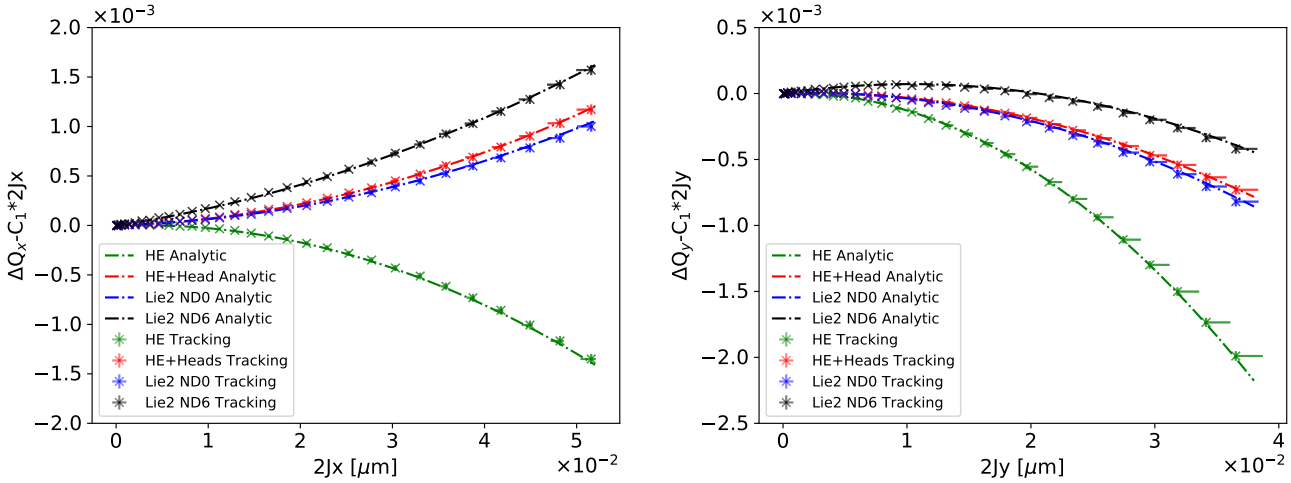

Figure 5.2: Amplitude detuning for the horizontal plane (left) and the vertical plane (right).

In order to understand the origin of the discrepancy for amplitude higher than $3.0 \times 10^{-2}\,\mu$m in Fig. 5.1, the same analysis is repeated considering only the b_6 harmonics error in the final focus quadrupoles. Since the error are generated using random number as explained in 4, the second order AD will be different from the previous section. The results are shown in Fig. 5.2 and Tab. 5.2.

In this case, there is no discrepancy between the theory and the simulation for all the models. This comforts us in the idea that the previous discrepancy comes from higher order harmonics that are not taken into consideration in the analytic calculation.

5.1.3 Precision of the Lie2 model and optimal order of the Generalized Gradient derivatives

In Ref. [57], the accuracy and efficiency of different integration and interpolation methods were studied and compared, including the Lie2 model presented here. In this section, we compare the tracking using the Lie2 transfer map with the reference model from [57], a 6th order Gauss method, using AD as figure of merit. Figure 5.3 shows

Table 5.2: Amplitude detuning coefficients from Fig. 5.2 fitted with a 4^{th}-order polynomial and for an Amplitude in μm.

	Fit		Analytical	
Case	$\partial Q_x/\partial(2J_x)$	$\partial^2 Q_x/\partial(2J_x)^2$	$\partial Q_x/\partial(2J_x)$	$\partial^2 Q_x/\partial(2J_x)^2$
HE	$(0.8 \pm 0.3) \times 10^{-3}$	-0.64 ± 0.03	0	-0.58
HE+Heads	$(0.6 \pm 0.3) \times 10^{-3}$	0.38 ± 0.03	0	0.39
Lie2 ND0	$(0.7 \pm 0.4) \times 10^{-3}$	0.28 ± 0.03	0	0.33
Lie2 ND6	$(11.4 \pm 0.4) \times 10^{-3}$	0.34 ± 0.04	10.9×10^{-3}	0.33
Case	$\partial Q_y/\partial(2J_y)$	$\partial^2 Q_y/\partial(2J_y)^2$	$\partial Q_y/\partial(2J_y)$	$\partial^2 Q_y/\partial(2J_y)^2$
HE	$(-0.2 \pm 0.5) \times 10^{-3}$	-1.64 ± 0.07	0	-1.59
HE+Heads	$(-0.5 \pm 0.5) \times 10^{-3}$	-0.59 ± 0.06	0	-0.62
Lie2 ND0	$(-0.3 \pm 0.5) \times 10^{-3}$	-0.74 ± 0.07	0	-0.67
Lie2 ND6	$(11.0 \pm 0.4) \times 10^{-3}$	-0.80 ± 0.05	10.9×10^{-3}	-0.67

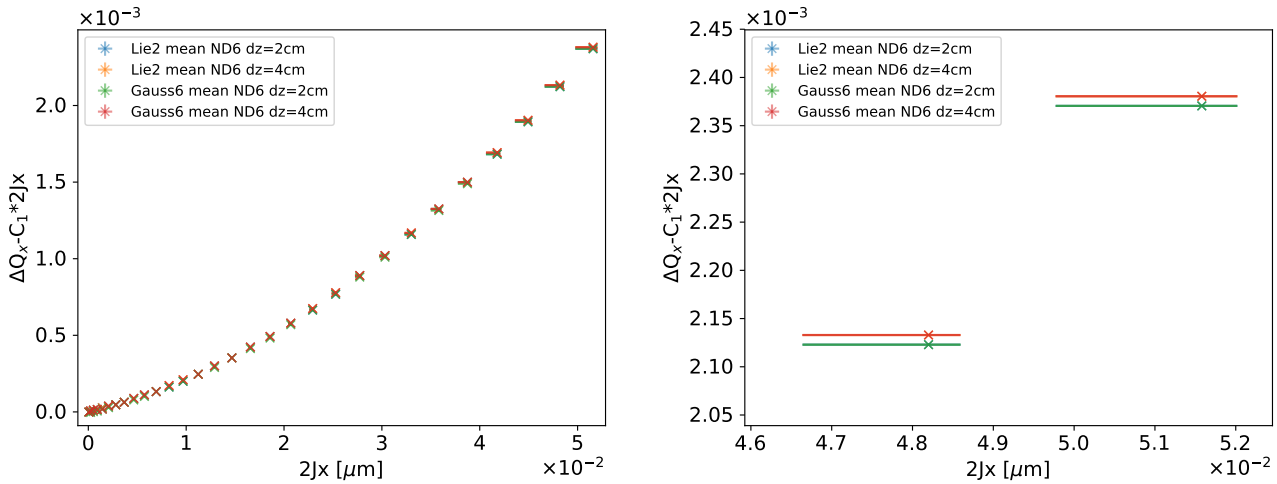

Figure 5.3: Comparison of the Lie2 model (for ND6) with the referential model (Gauss6) from Ref. [57] on the Amplitude Detuning for two different step sizes in z. The right plot is a zoom over the high amplitude. For each step size, the values for the model are superposed.

the impact on the AD for the two integration methods and two step sizes. A small difference of about 10^{-5} appears when going at amplitude higher than $0.02\,\mu$m, which is due to the step size in z. The two integration methods reproduce the same detuning with amplitude for a non-linear transfer map of $2\,$cm step size. In Fig. 5.4, two interpolation methods (mean and spline) are compared for two step sizes. The mean interpolation method seems more stable, with an error of the order of 10^{-5} which is also the precision of the frequency analysis of turn by turn BPMs data. We conclude that the step size in z has more impact on the precision of the model than the integration or the interpolation method chosen, which is also consistent with the results published in Ref. [57].

Figure 5.5 shows the impact of the order of gradients derivatives on the Amplitude Detuning. It appears that the 1st derivative generates half of the 1st-order Amplitude Detuning. This is not observed for the Horizontal plane

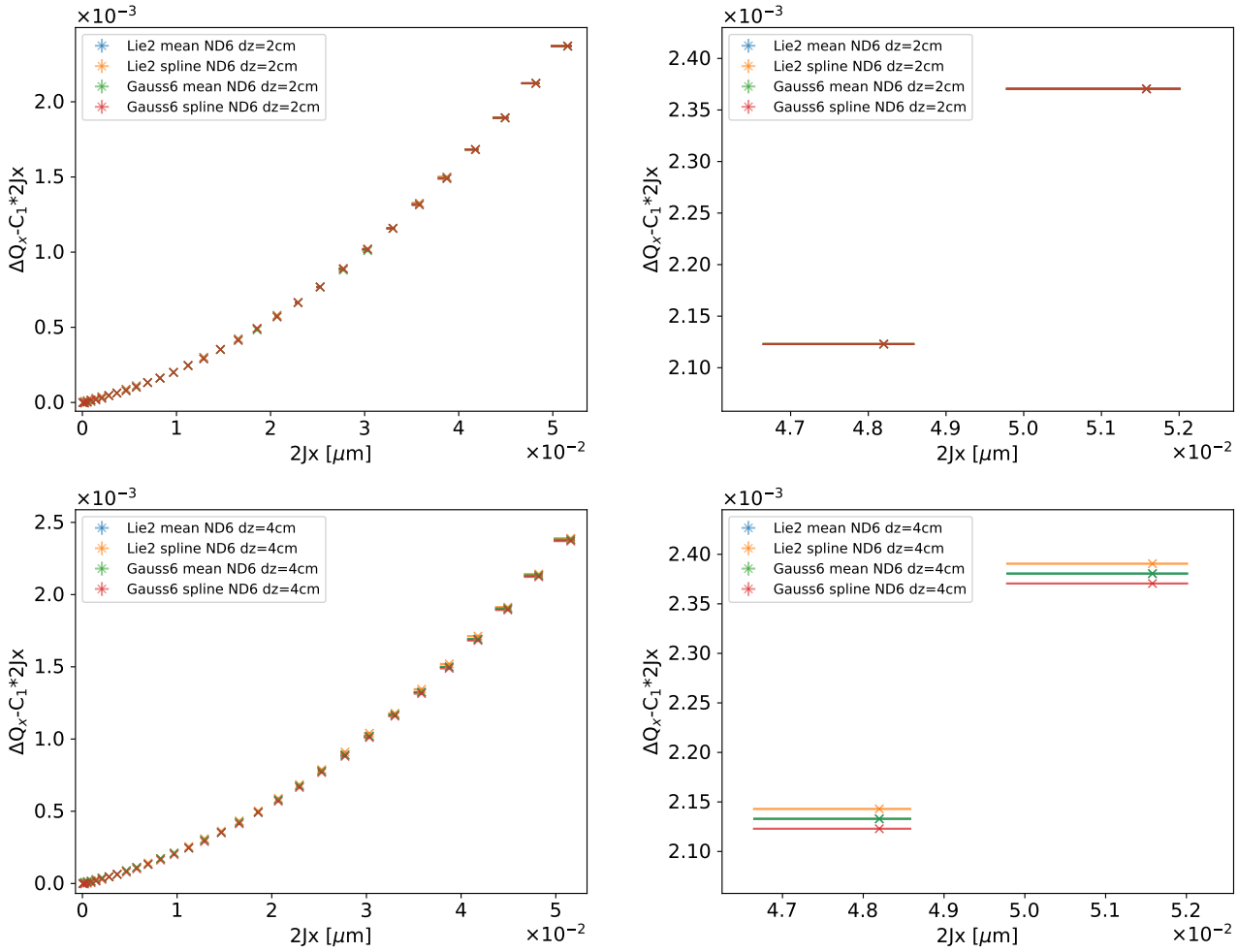

Figure 5.4: Comparison of the Lie2 model (for ND6) with the referential model (Gauss6) from Ref. [57] on the Amplitude Detuning for dz =2 cm (top) and 4 cm (bottom). The right plot is a zoom over the high amplitude. All the points for dz =2 cm and the mean points for dz =4 cm are superposed.

because of the Gauge used. In fact, in order to further speed-up tracking the horizontal-free Coulomb gauge is chosen, which requires in general between 20% and 25% less coefficients evaluation of the vector potential in Eq. (2.18), (2.19) and (2.20) with respect to the azimuthal-free gauge [57]. Nevertheless for even number of derivatives all the gauges produce exactly the same magnetic field by definition, and as a consequence will result in the same amplitude detuning. It is also important to note that no significant discrepancy can be observed for a number of derivatives higher than 2.

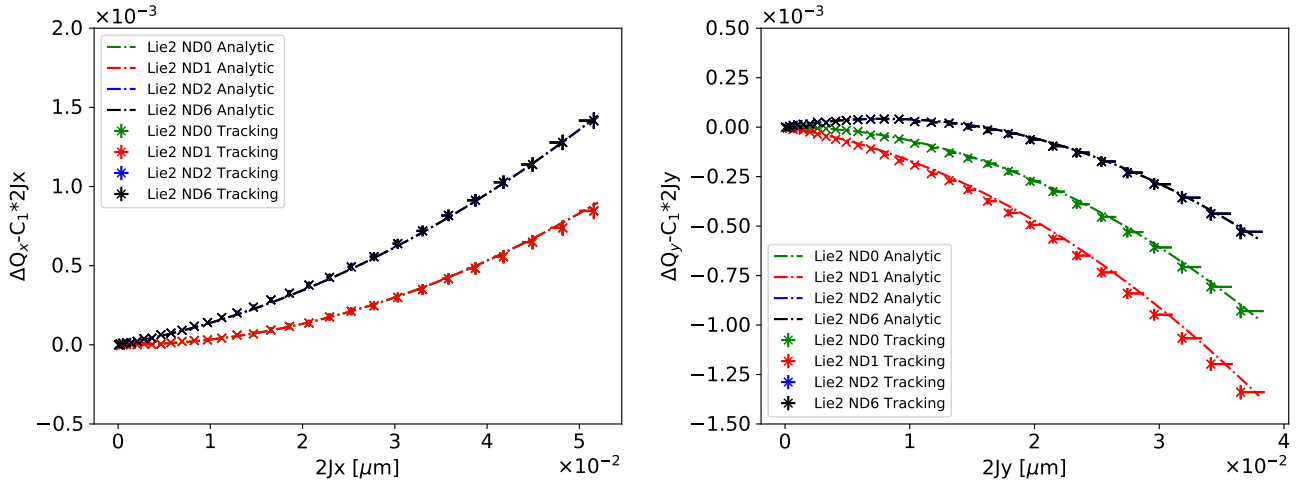

Figure 5.5: Horizontal (left) and vertical (Right) Amplitude Detuning for different numbers of gradients derivatives considered in the Lie2 model. The Vector Potential is computed with the Horizontal Free Coulomb gauge (see Ref. [57]).

5.1.4 Correction of non-linearities

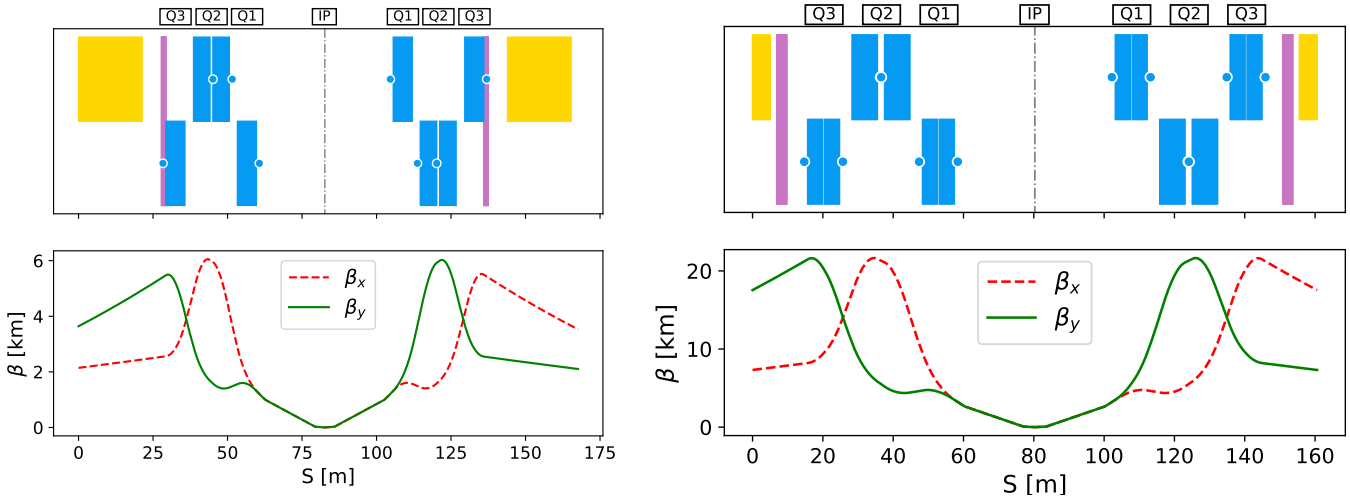

Figure 5.6: Single aperture elements in LHC (left) and HL-LHC (right) insertion regions. The three (splitted) quadrupoles composing each inner triplet (Q1, Q2 and Q3) are in blue, blue dots represent the position of the quadrupoles connectors, the first separation dipole is in yellow and the non-linear correctors are in purple (top panel). The horizontal and vertical β functions are shown in the bottom panel.

In LHC and HL-LHC, there is one corrector on each side of each Interaction Point (the purple elements shown in the top panel of Fig. 5.6 for LHC and HL-LHC).

Following Ref. [58, 59], a simple correction procedure of the resonance driving terms can be done by setting the

following coefficients to 0 (respectively normal and skew):

$$c(b_n;p,q,k,m) = \int_{IR} \mathrm{d}s\ K_{n-1}(s)\beta_x^{p/2}\beta_y^{q/2}e^{\pm i[(p-2k)\Delta\mu_x \pm (q-2m)\Delta\mu_y]} \tag{5.1}$$

$$c(a_n;p,q,k,m) = \int_{IR} \mathrm{d}s\ KS_{n-1}(s)\beta_x^{p/2}\beta_y^{q/2}e^{\pm i[(p-2k)\Delta\mu_x \pm (q-2m)\Delta\mu_y]} \tag{5.2}$$

The normal and skew errors can be identified by their strength, K_{n-1} and KS_{n-1}, respectively. We can easily see that the Resonance Driving Terms f_{jklm} (see Eq. (3.62)) is proportional to $c(b_n;p,q,k,m)$ and $c(a_n;p,q,l,m)$. This is especially true, if we enlighten that $p=j+k$ and $q=l+m$.

As it is the amplitude detuning that we want to correct here, we only focus on $c(b_n;p,q,k,m)=0$ with $p=2l$ and $q=2m$. Let's write the equation for the horizontal $(p=2k, q=0)$ and vertical $(p=0, q=2m)$ amplitude detuning (for $k,m \in \mathbb{N}^*$). This selection makes the complex exponential of Eq. (5.1) to be equal to 1 and since $p+q=j+k+l+m=n$, the equation can be simplified. Finally, let's separate the correctors from the rest of the errors by identifying their positions as L and R, respectively for the Left and Right side of the Interaction Point:

$$\begin{cases} c(b_n;n,0,n/2,0) = K_{n-1,L}\beta_{x,L}^{n/2} + K_{n-1,R}\beta_{x,R}^{n/2} + \displaystyle\int_{IR} \mathrm{d}s\ K_{n-1}(s)\beta_x^{n/2} = 0 \\ c(b_n;0,n,0,n/2) = K_{n-1,L}\beta_{y,L}^{n/2} + K_{n-1,R}\beta_{y,R}^{n/2} + \displaystyle\int_{IR} \mathrm{d}s\ K_{n-1}(s)\beta_y^{n/2} = 0 \end{cases} \tag{5.3}$$

We end up with an inverse problem easily solvable, $\mathbf{A}\vec{K}+\vec{h}=0$. We define:

- $\vec{K}$ as a vector that contains the correctors strength that need to be find;

$$\vec{K} = \begin{pmatrix} K_{n-1,L} \\ K_{n-1,R} \end{pmatrix} \tag{5.4}$$

- $\mathbf{A}$ as a matrix that contains the correctors factor contributing to the coefficients $c(b_n;p,q,k,m)$;

$$\mathbf{A} = \begin{pmatrix} \beta_{x,L}^{n/2} & \beta_{x,R}^{n/2} \\ \beta_{y,L}^{n/2} & \beta_{y,R}^{n/2} \end{pmatrix} \tag{5.5}$$

- $\vec{h}$ as a vector that contains the contributing to the coefficients $c(b_n;p,q,k,m)$ from the element of the Interaction Region.

$$\vec{h} = \int_{IR} K_{n-1}(s) \begin{pmatrix} \beta_x^{n/2}(s) \\ \beta_y^{n/2}(s) \end{pmatrix} \tag{5.6}$$

The solution of this inverse problem provides the Left (L) and Right (R) side corrector strengths:

$$\begin{pmatrix} K_{n-1,L} \\ K_{n-1,R} \end{pmatrix} = -\begin{pmatrix} \beta_{x,L}^{n/2} & \beta_{x,R}^{n/2} \\ \beta_{y,L}^{n/2} & \beta_{y,R}^{n/2} \end{pmatrix}^{-1} \int_{IR} K_{n-1,s} \begin{pmatrix} \beta_{x,s}^{n/2} \\ \beta_{y,s}^{n/2} \end{pmatrix} \tag{5.7}$$

As mentioned in the previous section, the Detuning with Amplitude and similarly all the RDTs are sensitive to the longitudinal distribution of the high order field harmonics. Since the non-linear corrections are computed in order to cancel the main RDTs, as a result, the correctors strength used to correct them is also sensitive to the longitudinal distribution of the non-linearities.

Figure 5.7 shows the correlation of the non-linear correctors strength at both sides of the high luminosity IPs for these 60 seeds. Since only the systematic component of the error as a longitudinal distribution (while the uncertainty and random component are equally distributed), it results in a systematic shift between the HE model and the others.

The octupole-like generated by b_2' and b_2'' produces a systematic shift in the octupole corrector strength of about 4% with respect to the b_4 corrector specification given in Ref. [9]. In the case of b_6 correction, the systematic shift is around 13%, always with respect to the present corrector specification. The shifts are symbolised by arrows in Fig. 5.7.

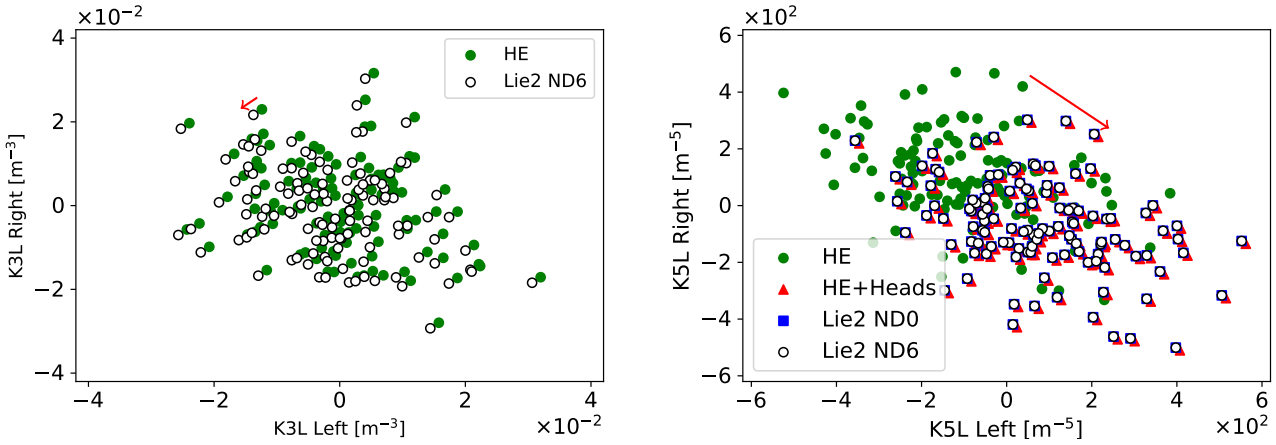

Figure 5.7: Integrated strength of the b_4 (called KCOX, left) and b_6 (called KCTX right) corrector computed for different models in IR1 and IR5, with 60 seeds.

The shift stays within the correctors specification also for the dodecapole corrector. The difference between the shift for the HE+Heads and the Lie2 models, as well as the effect of the gradients derivatives, is negligible in this case.

As explained in the previous chapter, only the longitudinal distribution of the systematic part of the errors is studied. The random part of the harmonics is considered equally distributed in the magnet, since this random component is computed using 2D Monte Carlo simulations. Therefore, measurements of the longitudinal profile for all the harmonics (above all the ones that do not have a systematic component) is essential to be able to model

them accurately in the calculation of the correction.

5.2 Octupole and dodecapole correction in LHC

During the LHC commissioning while using amplitude detuning and feed-down data, the beam based values for the octupole corrector strengths have been estimated for both side of the ATLAS and CMS interaction points (respectively IP1 and IP5). A discrepancy is found between beam-based values for the octupole correctors and predicted ones from magnetic field measurements [5]. At collision energy, the main source of this octupole errors are the final focus quadrupoles composing the inner triplet (IT) of the LHC optics.

The Final Focusing quadrupoles in those regions are composed of two families, named MQXA and MQXB. The former have been developed and built at the KEK (Japan) while at FermiLab (USA) for the latter. The IT quadrupoles Q_1 and Q_3 are from the MQXA family while the Q_2 are from the MQXB family. Different potential sources have been studied to explain this discrepancy (detector solenoid Fringe Field, Beam Screen, magnets manufacturing imperfection, etc.). In the CERN magnets documentation [24], it is reported that because of its geometry, the MQXA type quadrupoles have an ovalization of its iron and coil. This generates a systematic b_4, which is normally not allowed. It is also worth noticing that the Beam Screen geometry generates another b_4 harmonics in the Final Focusing quadrupoles.

In section 5.1, we have shown that considering the Fringe Field, i.e. the longitudinal harmonics distribution inside the HL-LHC Inner Triplet could give a change up to 13% in the non-linear corrector strength. The goal here is to repeat this study for the LHC Inner Triplet. Our starting point is the Return End (RE) of the 3D magnetic model (made with the CERN Roxie code [60], used for magnetic field computation and magnet design) and the mechanical drawings of the MQXA magnets, given to us by H. Nakamoto (KEK). We aim to reconstruct a model for the MQXA as built in the machine. This is the result of S. Bagnis internship in collaboration with C. Lorin from CEA IRFU/DACM/LEAS. Unfortunately, none of this information could be found for the MQXB magnet.

5.2.1 The 3D magnetic model of MQXA

The aim is to reconstruct the machine-like 3D model of the magnet including the coil, the collar, the yoke as well as the Beam Screen (BS) as oriented in the machine. The BS is a $1\,\mathrm{mm}$ thick cut circle with a $0.5\,\mathrm{mm}$ thick cooling tube on each flat side. The material of the Beam Screen corresponds to a magnetic permeability of 1.0025 as for the collar. The one of IP1 is vertically oriented while in IP5 it is horizontally oriented as shown in Fig. 5.8. The BS radius is different in Q_3 and Q_1, passing from diameters $(28.90\,\mathrm{mm}/24.00\,\mathrm{mm})$ in Q_3 to $(23.85\,\mathrm{mm}/18.95\,\mathrm{mm})$ in Q_1 (respectively, the circle inner radius and semi-major/ the flat side inner distance to the aperture center).

The systematic values of the b_4, b_8, etc was supposed to come from an ovalization due to a dipole-like yoke

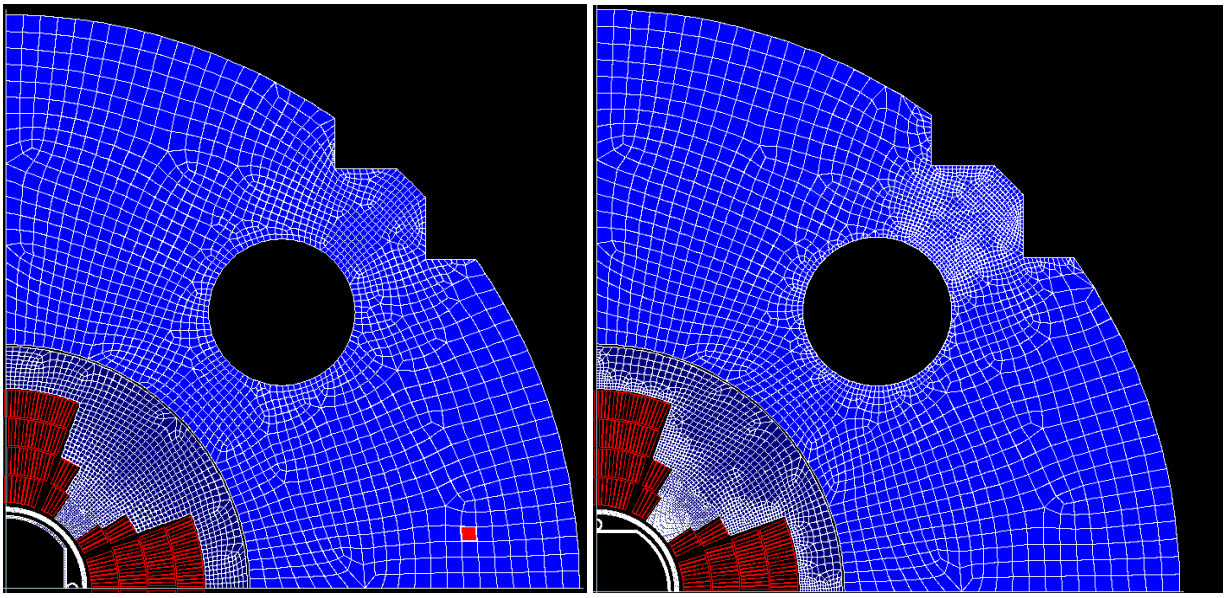

Figure 5.8: Cross-section of the Q_3 magnet, the IP1 Right side (3R1, left) and the IP5 Left side (3L5, right) with their Beam Screen are shown.

assembly [61]. In order to simulate this ovalization in the Roxie magnetic model, the coils blocks have been displaced homogeneously by $50\,\mu\mathrm{m}$ (positive for the x-axis and negative for the y-axis) and the iron yoke elliptically deformed.

The design of the magnet RE is straightforward to generate in Roxie. Its dimensions were extract from mechanical drawings with a precision of about $1\,\mathrm{mm}$ in the longitudinal position of each block. The Lead End (LE) of the magnet is more complex to reconstruct in Roxie. The layer jumps, the internal splice due to the conductor grading in the second layer, and the conductors leads have been carefully modeled. A specificity of the MQXA magnet is the use of normal and mirror coils that breaks the quadrupolar symmetry in the layer jump area and more generally all over the LE. This specificity is another source of b_4. Figure 5.9 shows the 3D reconstruction of the coil return and lead ends.

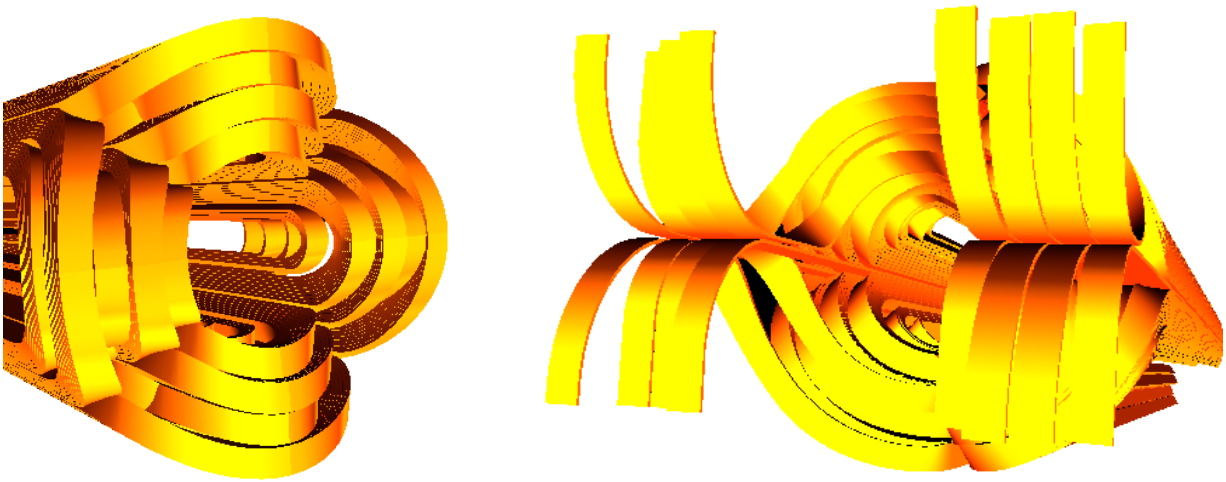

Figure 5.9: MQXA Return Ends (RE, left) and Lead Ends (LE, right).

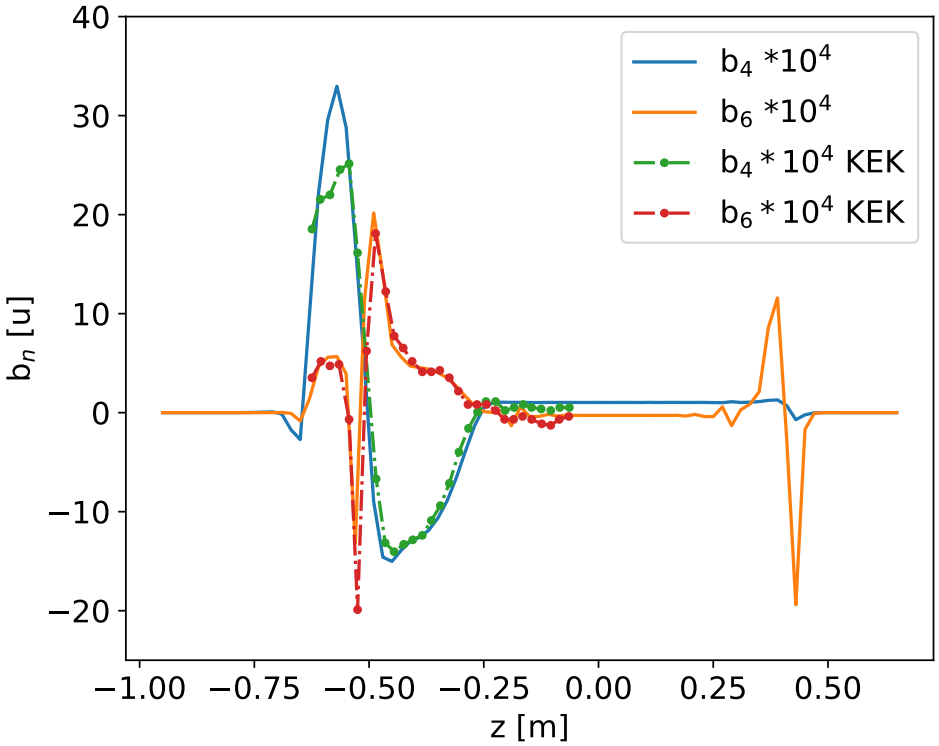

Figure 5.10: Comparison of the harmonics longitudinal distribution from the Roxie 3D machine-like model (continuous lines) and the longitudinal magnetic measurements performed at the KEK (dots). Courtesy of H. Nakamoto (KEK).

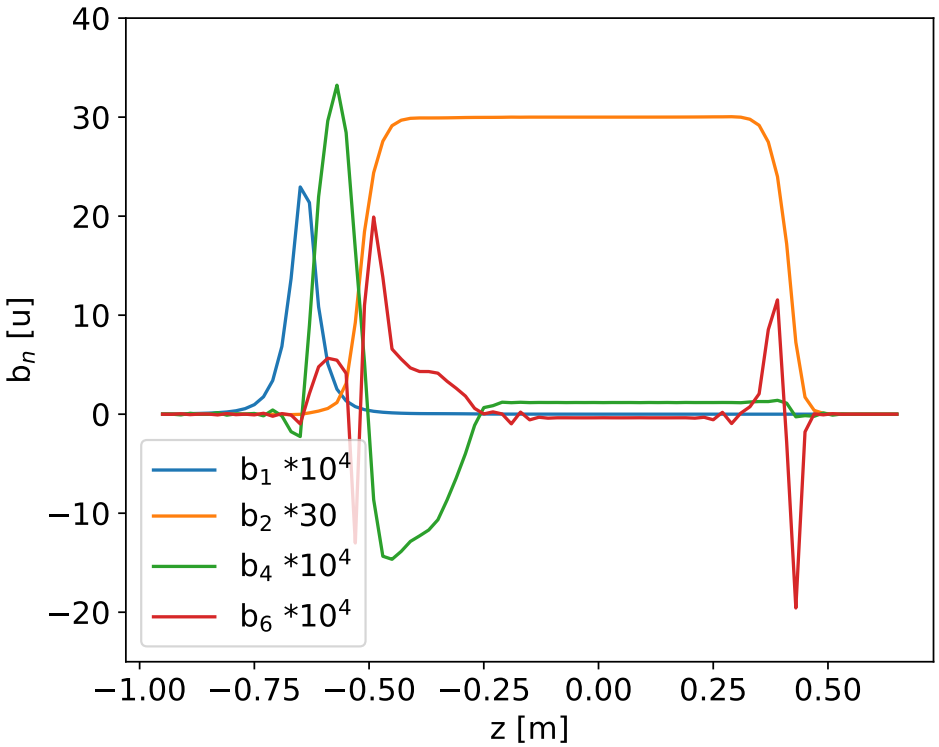

Figure 5.11: Longitudinal profile of the harmonics in the Q_3 magnet from the Left side of IP5.

5.2.2 MQXA field quality

With the Roxie, it is possible to compute Field Harmonics and, in particular, the longitudinal distribution of such Harmonics with the desired step in z. Figure 5.10 shows a comparison of the longitudinal b_4 and b_6 harmonics computed from the 3D magnetic model described in the previous section and the values for the Lead End, as measured at KEK with the rotating coil technique for steps of $2\,\mathrm{cm}$. In order to speed up the computation, we have shorten the length of the central and constant field of the magnet. The model and the measurements agree pretty well in the case of b_6 harmonics. They show overall good agreement in the case of b_4 harmonics, with a visible difference in the region between -0.75 and -0.5 m.

Table 5.3: Harmonics in the different sections of the MQXA magnet. C+I refer to the magnet with only the iron, 3R1 and 3L5 refer to the Beam Screen type and orientation.

Struc.	Roxie	L_{mag}	b_1	b_3	b_4	b_6
C+I	Total	6.37	0.30	0.02	1.05	0.03
	Body	–	0.00	0.00	1.03	-0.28
	LE	0.41	4.68	0.38	1.33	4.45
	RE	0.20	0.00	0.00	1.01	-0.19
C+I+3L5	Total	6.37	0.30	0.02	1.19	-0.05
	Body	–	0.00	0.00	1.17	-0.36
	LE	0.41	4.68	0.38	1.44	4.39
	RE	0.20	0.00	0.00	1.21	-0.30
C+I+3R1	Total	6.37	0.30	0.02	0.93	-0.05
	Body	–	0.00	0.00	0.90	-0.37
	LE	0.41	4.68	0.38	1.48	4.68
	RE	0.20	0.00	0.00	0.82	-0.30

The integrated value of b_4, considering the ovalization of the Coils and Iron, and the detailed description of the LE, is slightly lower with respect to the total integrated measured value, including its error (i.e. 1.30 ± 0.11 units). The Beam Screens impact the b_4 and b_6 harmonics as can be seen in Table 5.3. While no major difference is visible in the longitudinal harmonics distribution, as shown in Fig. 5.11. The Beam Screen contributions are close to the ones considered in the WISE database[1] (i.e. +0.14 for IP5 and -0.12 for IP1).

The WISE total values for the Q_3 magnets are bigger than the total ones from our machine-like 3D model of 0.2 units (or more), as shown in Fig. 5.12.

5.2.3 Effect of 3D magnetic field on non-linear corrector strength

Figures 5.13 and 5.14 shows the correlation of the non-linear correctors strength (respectively octupole and dodecapole correctors) at both sides of the high luminosity IPs for 60 machine configurations (given by the b_2 random errors).

[1] WISE is the database which contains the measured integrated harmonics for each element of the LHC ring, as mentioned in section 1.1.2.

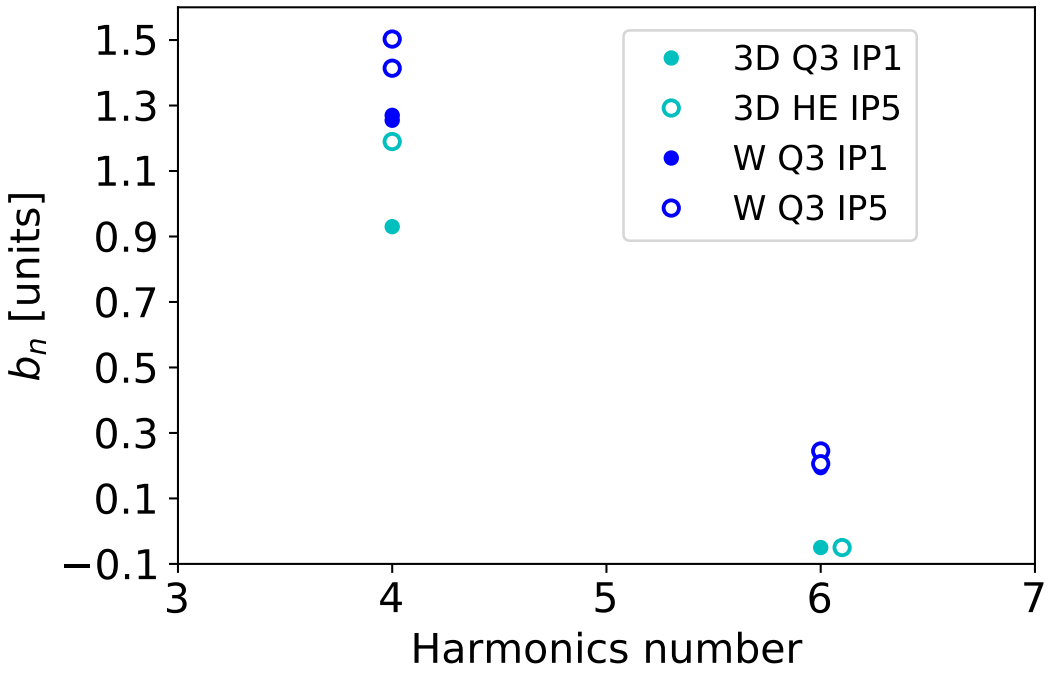

Figure 5.12: Total harmonics values from the WISE database and from the Roxie machine-like 3D model.

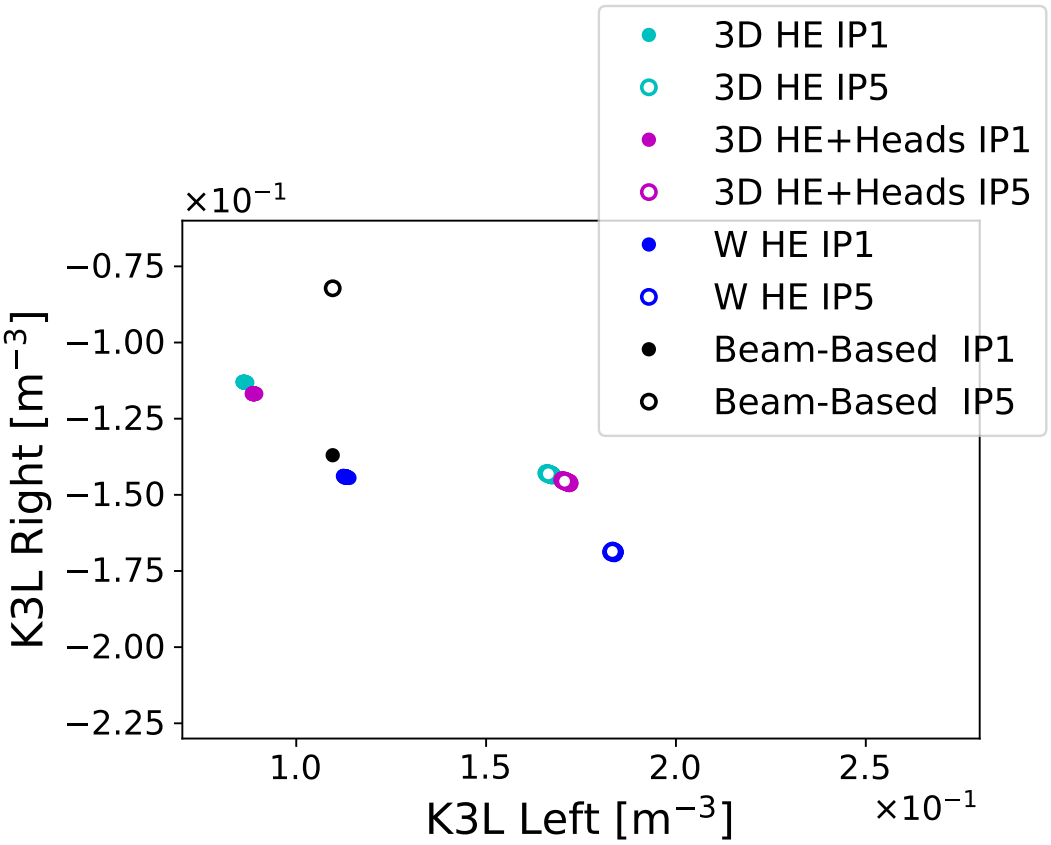

Figure 5.13: Integrated strength of the b_4 corrector computed for different models in IR1 and IR5, and 60 slightly different b_2 values.

Figure 5.13 shows the comparison between the beam-based estimations, the predicted values using the reference WISE total harmonics (W) and the predictions using our machine-like 3D model, reported in Tab. 5.3. The Roxie simulation with the smaller Beam Screen of the Q_1 magnet didn't converge, so the same values as Q_3 are used in this analysis. Its impact is expected to be less important than the Q_3 and the Q_2 (of type MQXB), due to the lower β-function in Q_1. Since we have no information of the MQXB Fringe Field, we use the WISE values for these magnets. As explained in [5], the WISE prediction are pretty accurate for IP1 while pretty far for IP5. With this approximation the 3D HE model predict values shift to the upper left, decreasing the accuracy for IP1 but improving for IP5. Taking into consideration the harmonic longitudinal distribution apply a small shift in the lower left direction so it cannot explained the discrepancy with the Beam-Based measurements.

In Fig. 5.13, the prediction for the HE and HE+Heads obtained by our 3D magnetic analysis are shown, together with the WISE predictions but without the beam-based values. There is no clear evidence of second order amplitude detuning from Beam-Based measurements in LHC. While, using the WISE values quite a strong correction should be needed in both IPs. In this respect, it is worth noticing that our 3D magnetic model gives a total b_6 which is significantly lower than the WISE values, going in the direction of the Beam-Based measurements. The HE+Heads model produce a shift in the same direction found for b_4 but bigger.

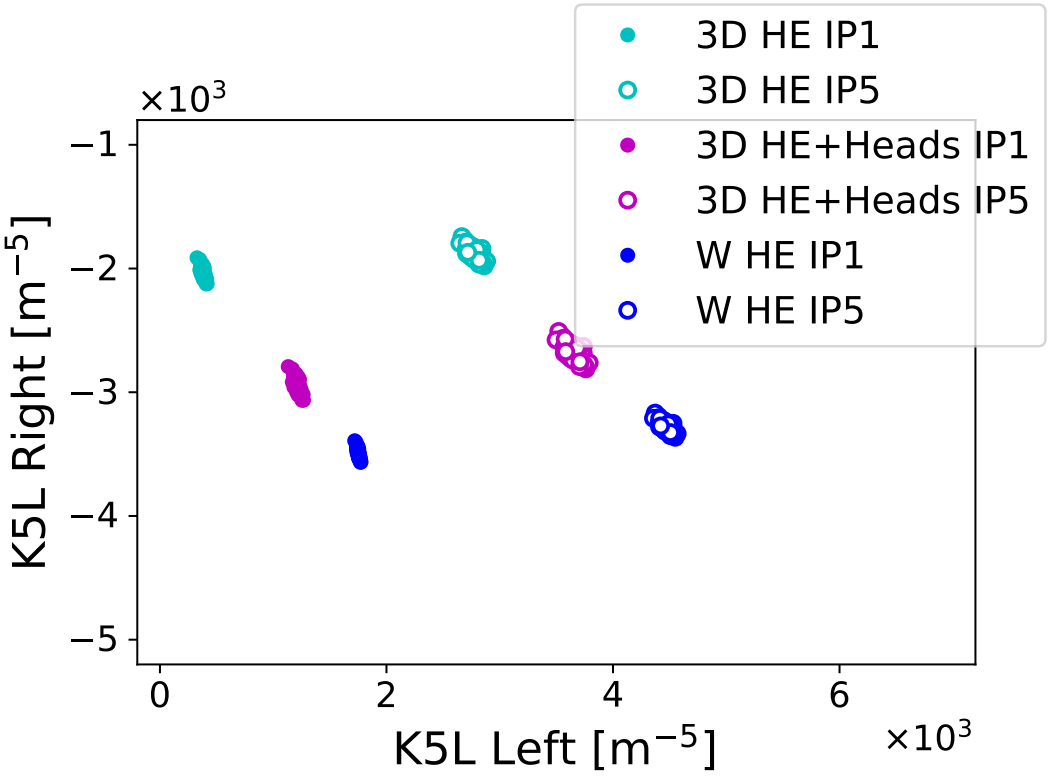

Figure 5.14: Integrated strength of the b_6 corrector computed for different models in IR1 and IR5, and 60 slightly different b_2 values.

As a conclusion, the 3D magnetic model of the MQXA type quadrupoles for the Q_1 and Q_3 LHC Inner Triplet

seems to be conform to the KEK magnetic measurement of the Connector Side (or Lead End). It appears that the LHC ellipsoidal Beam Screen not only add a b_4 harmonics along the magnet but also a b_6 one. The BS contribution doesn't necessarily sum in the same way in the body and in the ends of the magnet. Our analysis goes in the direction of the Beam-Based measurements concerning the b_6 integrating values of the MQXA type quadrupoles. It shows that it is important to take into consideration all the possible sources of the high order harmonics in order to reproduce Beam-Based values with the model of the machine. It claims for very accurate magnetic measurements (i.e. $\leq$ 0.1 units) of the Inner Triplet quadrupoles field quality.

***

In this chapter, we have evaluated the impact of the 3D realistic description of the inner triplet magnetic field on the amplitude detuning and on the calculation of the non-linear correctors strengths. In the case of HL-LHC, using computed longitudinal harmonics provided by magnet designers and tracking simulations, we show that the impact of the derivatives of the main quadrupole field (octupole-like) is small ($\sim 4\%$), while the impact of the longitudinal distribution of the dodecapole harmonics can be as high as $\sim 13\%$ with respect to the maximum corrector strength. Our preliminary studies for the case of LHC show similare results. The effects of the longitudinal distribution of the octupole harmonics is small while the dodecapole one is high.

In the next chapter, we look at a more local observable in order to define another way to evaluate the non-linear field strengths in the accelerator, that is the variation of the measured beta-function with the particle amplitude.

Chapter 6

Amplitude Beta-Beating

In this chapter, a new beam-based observable called the Amplitude Beta-Beating (ABB), is studied numerically. The theory is described in section 3.6, where it is explained that Resonance Driving Terms acting on the Spectral Ray H(-1,0) and V(0,-1) are respectively associated to the horizontal (HABB) and vertical beta-beating (VABB).

In the first section, predictions for HL-LHC are presented, using tracking simulations. For this, the simulation from the amplitude detuning analysis are reused to extract the turn-by-turn positions of the particle at each Beam Position Monitors (BPM). Those positions are then analysed by the BetaBeat.src, a CERN code for beam based measurements data analysis [62], in order to extract the beta-beating at each BPMs for different horizontal actions. In the second section, some data taken in LHC Machine Developments (MD) studies are analysed, to check if ABB is actually visible in the real machine. This analysis is then compared to what we should expect from the BPMs noise. In the last section, three configurations of the LHC using octupole to generate an HABB stronger than the noise are proposed.

6.1 HL-LHC predictions

While studying the impact of the longitudinal harmonics distribution inside HL-LHC Inner Triplet on Amplitude detuning and Dynamic Aperture using the HLLHCv1.0 optics (see chapter 5 and 7), we have also checked if Amplitude beta-beating could be measured.

As shown in Fig. 6.1, the foreseen b_4 harmonics in the Interaction Region Inner Triplet generates a linear Amplitude beta-beating of the order of 1 to $3\,\%$ at an action of $0.04\,\mu$m.

In Figure 6.2 is shown what happen when only the b_6 is considered. This time a 2^{nd}-order Amplitude beta-beating appears but once again very small (a discrepancy of less than $1\,\%$ at an action of $0.04\,\mu$m). Both figures are for the Hard-Edge model.

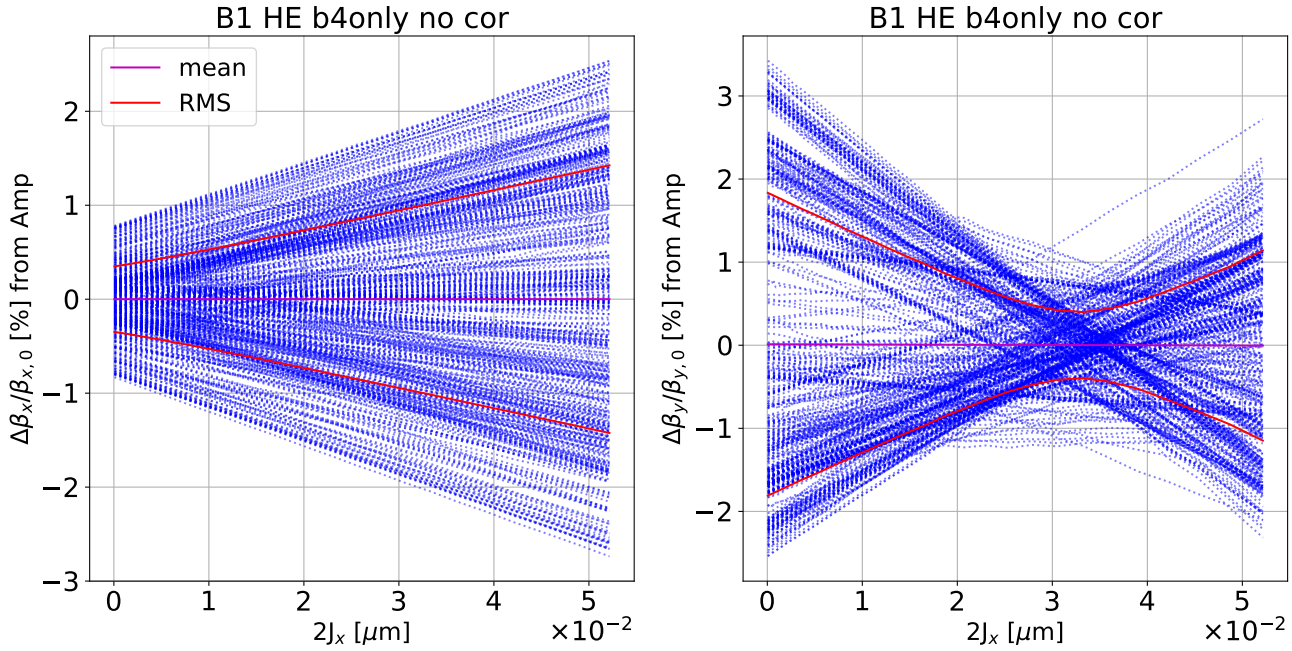

Figure 6.1: Projection of simulated Horizontal (left) and Vertical (right) beta-beating computed from the spectral amplitude for different action on the horizontal axis, for all the HL-LHC BPMs, when the b_4 harmonics is not corrected, and for the HE model.

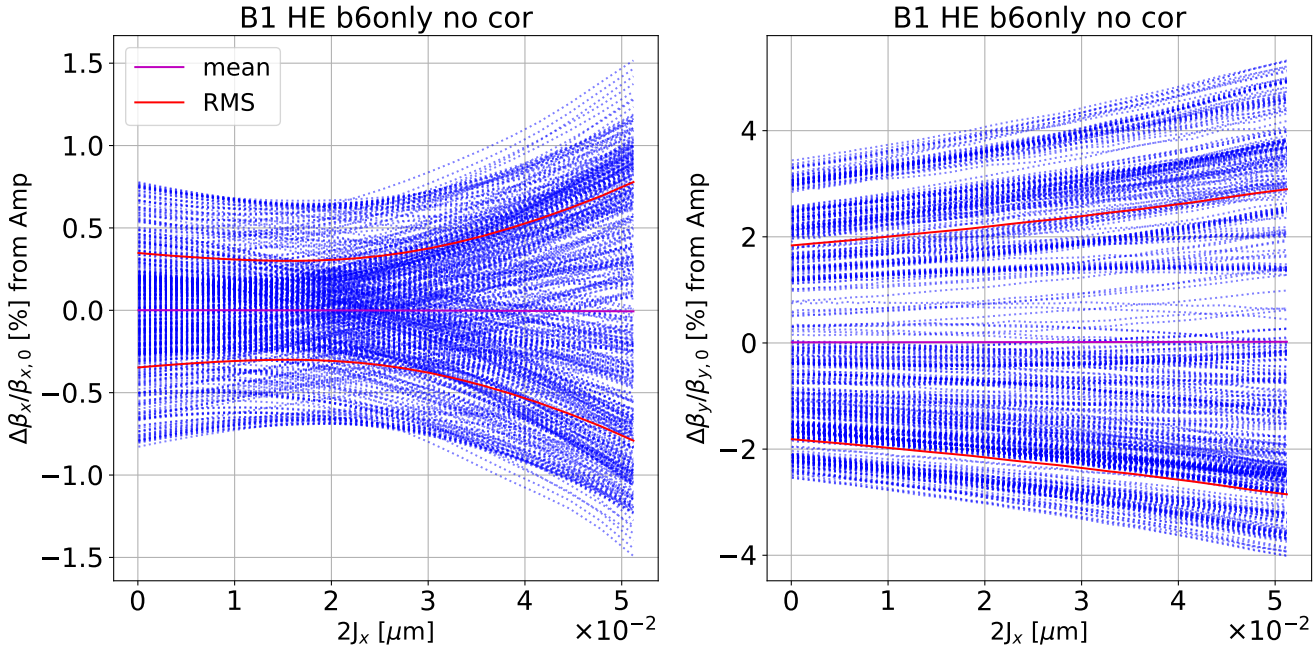

Figure 6.2: Projection of simulated Horizontal (left) and Vertical (right) beta-beating computed from the spectral amplitude for different action on the horizontal axis, for all the HL-LHC BPMs, when the b_6 harmonics is not corrected, and for the HE model.

Now, let's see what happen if the distribution of the harmonics is not uniform along the magnet. For HL-LHC, the systematic b_4 harmonics is not expected by design therefore we concentrate our Fringe Field study on the b_6.

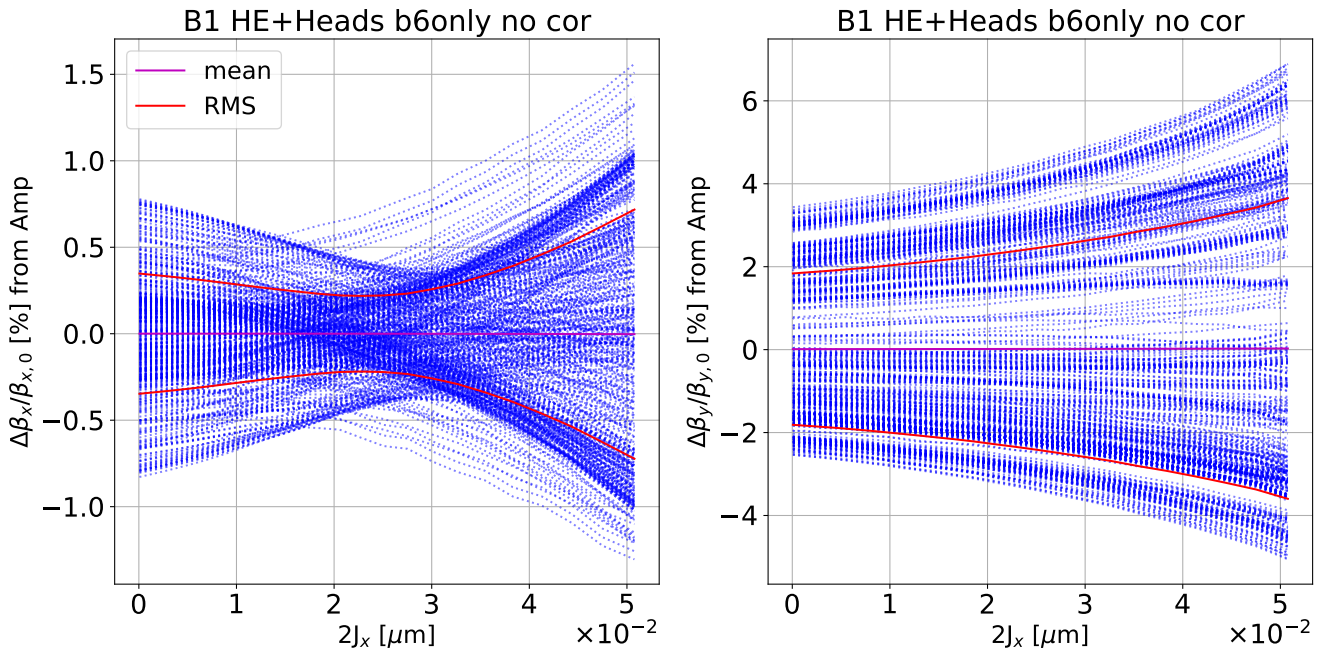

Figure 6.3: Projection of simulated Horizontal (left) and Vertical (right) beta-beating computed from the spectral amplitude for different action on the horizontal axis, for all the LHC BPMs, when the b_6 harmonics is not corrected, and for the HE+Heads model.

Figure 6.3 shows the effect of the same b_6 as in Fig. 6.2 for the HE+Heads model. In this case, the 2^{nd}-order Amplitude beta-beating is stronger but still very small, a discrepancy of $\sim 1\,\%$ at an action of $0.04\,\mu$m. Nonetheless, the discrepancy between the two models can hardly be seen in the RMS (red line in both plots), particularly for the horizontal plane. This is caused by the fact that most of the time, the horizontal Amplitude beta-beating tends to decrease the original beta-beating instead of increasing. In the vertical plane, it might be possible to see the difference but for that we have to compare with the precision of the measurements.

6.2 Search for Amplitude Beta-beating in the LHC

The first time this phenomena has been hypothesized was during a HL-LHC WP2 meeting at CERN in 2018 where we presented our first results of the Fringe Field impact on the Amplitude Detuning and Dynamic Aperture. During this meeting, the question was raised if a variation of the deviation of the Betatronic functions from the model (i.e. Beta-Beating) could be observed with the action, and used to detect local variation of multipoles strengths in the machine.

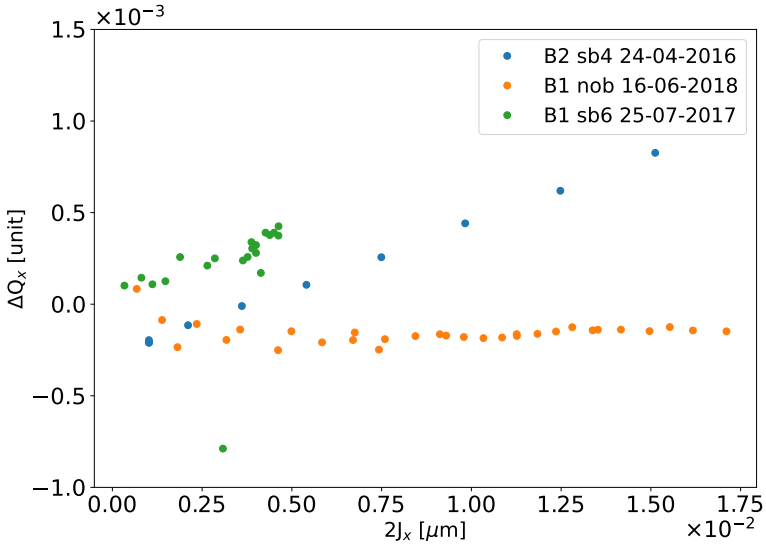

Figure 6.4: Measurements of the Amplitude detuning on horizontal axis for different Machine Development (MD) on the LHC. nob means a flat Amplitude detuning, sb4 and sb6 mean that there are respectively uncorrected b_4 and b_6..

6.2.1 Analysis of LHC turn-by-turn data

Our preliminary step was to check if this phenomena has already been observed during one of the Machine Development (MD). During those tests on the LHC, the beam physicists team uses the AC dipole [63] to increase the particle action in order to measure Amplitude detuning, as shown in Fig. 6.4. In the following plots, *nob* means that amplitude detuning has been corrected using the non-linear correctors in the insertion regions, *sb4* and *sb6* mean that there are, respectively, uncorrected first and second order amplitude detuning (Ref. [54, 5, 55, 64]).

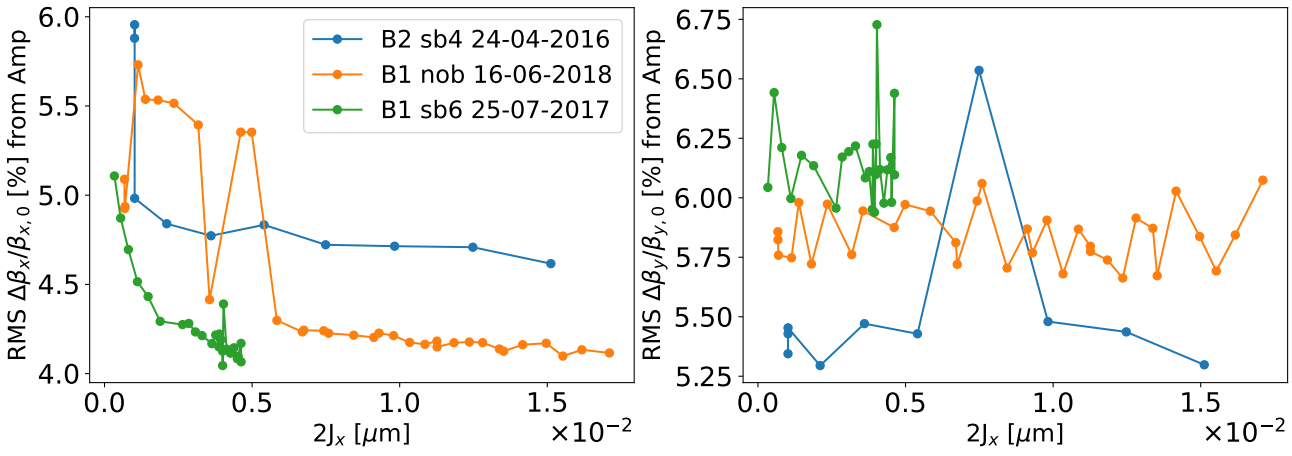

Figure 6.5: Variation of the Horizontal (left) and Vertical (right) RMS beta-beating computed from the spectral line amplitude for different actions on horizontal axis, for different LHC MD data.

Figure 6.5 shows the variation of both Horizontal and Vertical RMS beta-beating while the action in the horizontal axis increases. It appears that the horizontal beta-beating varies with the action but the decrease in $1/2J_x$ of the

RMS beta-beating can mainly be explained by the signal-to-noise improvement (see in Section 6.2.2).

This is particularly clear when looking at the evolution of beta-beating for each of the BPMs, as shown in the right side of Fig. 6.6 for the MD 2158 (25-07-2017) (where the amplitude detuning has been computed using as reference the tunes from the model). If we look at certain BPMs, it might be possible to see Amplitude beta-beating but it is covered by the noise when all the BPM are considered. Some BPMs stand out such as "BPM.14L3.B1" whose horizontal beta-beating strongly increases for low action and then, decrease a bit slower. From the theory, this could be explained by very strong b_4 and b_6 near the BPM with the right phase advance between them but we can hardly see the same behaviour in the nearby BPMs, and as far as we known no such strong harmonics where reported.

If we compared it to the behaviour in a latter Machine Development shown in the left side of Fig. 6.6 (MD 3311 made the 16/06/2018), it appears that the initial beta-beating greatly improved for this BPM (even if over the whole machine the beta-beating stays within $\pm 20\%$ in both axis). A linear Horizontal Amplitude Beta-Beating might appears of the order of few percents. With the noise mentioned previously, we cannot ascertain with great confidence if this is the case. More data are needed.

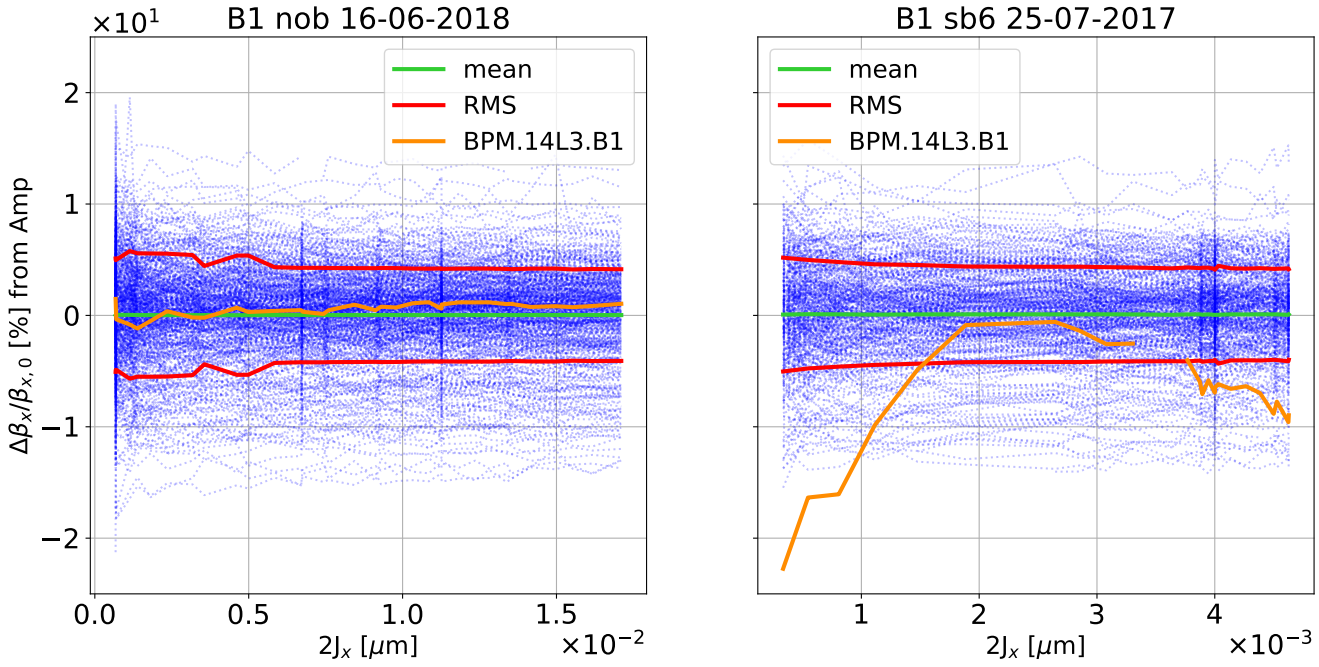

Figure 6.6: Projection of measured Horizontal beta-beating computed from the spectral line amplitude for different actions on horizontal axis. Those values were measured for the MD 3311 of 16/06/2018 (Left) and the MD 20158 of 25/07/2017. The blue dash lines correspond to the individual LHC BPMs while the beta-beating mean and RMS are respectively in green and red. The BPM named BPM.14L3.B1 is unlighted in orange.

6.2.2 Impact of the BPMs noise

In this section we try to quantify how much the noise impacts our observables and the accuracy of the algorithm, used in the previous section to analyze the LHC turn-by-turn data. In this section, we will try to answer the following question: Can the level of noise σ_{BPM} be estimated directly from the spectrum and what are the incertitude of the reconstructed signal parameters (i.e. frequency Q, amplitude A and phase P) of a noised sinusoidal signal $x(t)$?

$$x(t) = A\ \cos(Qt + P) + \sigma_{BPM}\mathcal{N}(0, 1) \tag{6.1}$$

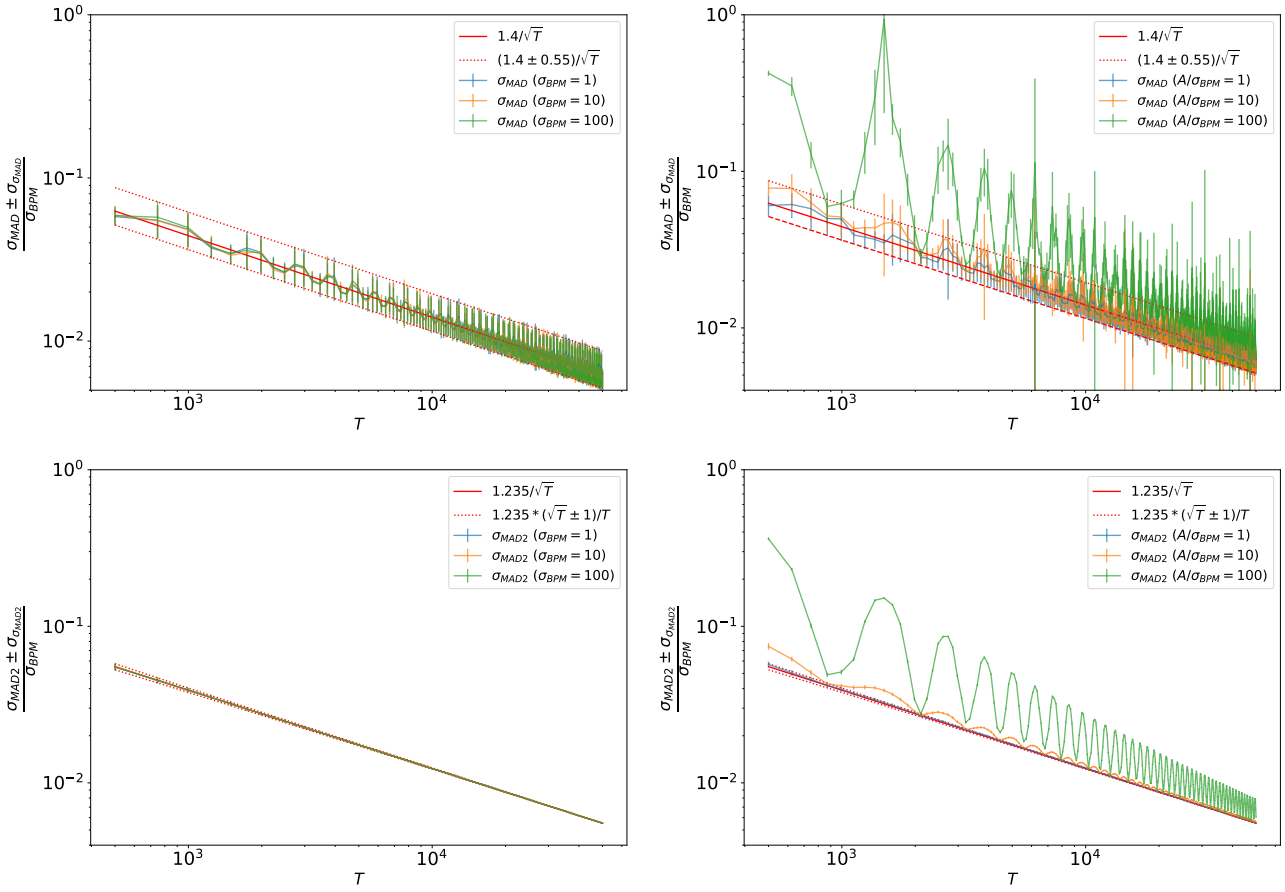

Figure 6.7: Evolution of the measured noise using the MAD (top) and MAD2 (bottom) formula as a function of the sample size with (right) and without (left) a signal with $Q = 0.62002\pi$.

In Ref. [65], J. L. Starck presents a method to measure the noise sigma. It is called the Median Absolute Deviation (MAD) and one option to define the reconstructed noise sigma from the FFT of the signal $x(t)$ is:

$$\sigma_{\text{MAD}} = 1.4826 \times \text{median}\left(|\text{fft}(x) - \text{mean}\left(\text{fft}(x)\right)|\right) \tag{6.2}$$

The Fourier Transform of a signal is very sparse and for high amplitude signal. This can have a non-trivial impact

on the mean over the different frequency of the FFT. This raises the questions: what information this averaged FFT provides, and how does it affect the median of the FFT amplitudes. So, another MAD algorithm is proposed:

$$\sigma_{\text{MAD2}} = 1.4826 \times \text{median}\left(|\text{fft}(x)|\right) \tag{6.3}$$

Figure 6.7 shows the evolution of statistics of σ_{MAD} divided by σ_{BPM} as a function of the size (T) of the sample for the FFT. Different noise levels with and without a sinusoidal signal are compared. The statistics was computed using 100 seeds and the RMS value of σ_{MAD} is noted as $\sigma_{\sigma_{\text{MAD}}}$. The red lines correspond to the result of a fit of the mean value and the RMS (dashed line) without sinusoidal signal.

Without sinusoidal signal, there is a direct relation between the ratio $\sigma_{\text{MAD}}/\sigma_{BPM}$ and the sample size. MAD2 gives much more stable results than MAD with also a ratio $\sigma_{\text{MAD}}/\sigma_{BPM}$ closer to $1/\sqrt{T}$ in average. As can be seen in the plots on the right side of Fig. 6.7, the resulting error in the sigma noise is less than $1/100$ of ratio signal amplitude over sigma noise. The expressions of the fit are:

- For the original MAD equation:

$$\sigma_{\text{MAD}} = \sigma_{BPM} \times (1.4 \pm 0.55)/\sqrt{T} \tag{6.4}$$

- For our approximation MAD2:

$$\sigma_{\text{MAD2}} = \sigma_{BPM} \times 1.235(\sqrt{T} \pm 1)/T \tag{6.5}$$

If a sinusoidal signal is added, a similar offset and a sinusoidal response are observed for both MAD evaluations. Removing the mean in the expression of MAD only affect the RMS. Since MAD and MAD2 have in average a similar behaviour, this can only come from the median of the FFT amplitudes. It seems to be correlated with the size of the sample and the sinusoidal signal Amplitude and Frequency. A first explanation actually studied, could come from the Fourier Transform formalism where, as reported in Ref. [66]:

$$\int_{-T/2}^{T/2} \frac{Ae^{i(\omega-\nu)t}}{T}\,\mathrm{d}t = \frac{2A\sin((\omega-\nu)T/2)}{(\omega-\nu)T} \tag{6.6}$$

Figure 6.8 shows the statistics of the discrepancy between the actual and measured spectral line parameters as a function of the signal amplitude divide by σ_{BPM}. Two Frequency Analysis algorithms are compared: NAFF (Ref. [67]) and SUSSIX (Ref. [68, 69]). Those two algorithms are based on iterative routines to measure the tune frequency and are widely used in the accelerator community. The NAFF algorithm has mostly been developed by J. Laskar in the nineties while SUSSIX is based on the TUNEWT algorithm developed by A. Bazzani in the mid-nineties and further developed and tested since then [70]. The statistics has been obtained using 100 seeds and with samples of size $T = 1000$. The red line correspond to the fitted RMS value. It is known that there is an offset on the frequency given by the NAFF algorithm. As it is not related to this study, it has been taken into account in our

theory as an offset (Offset$_{NAFF}$).

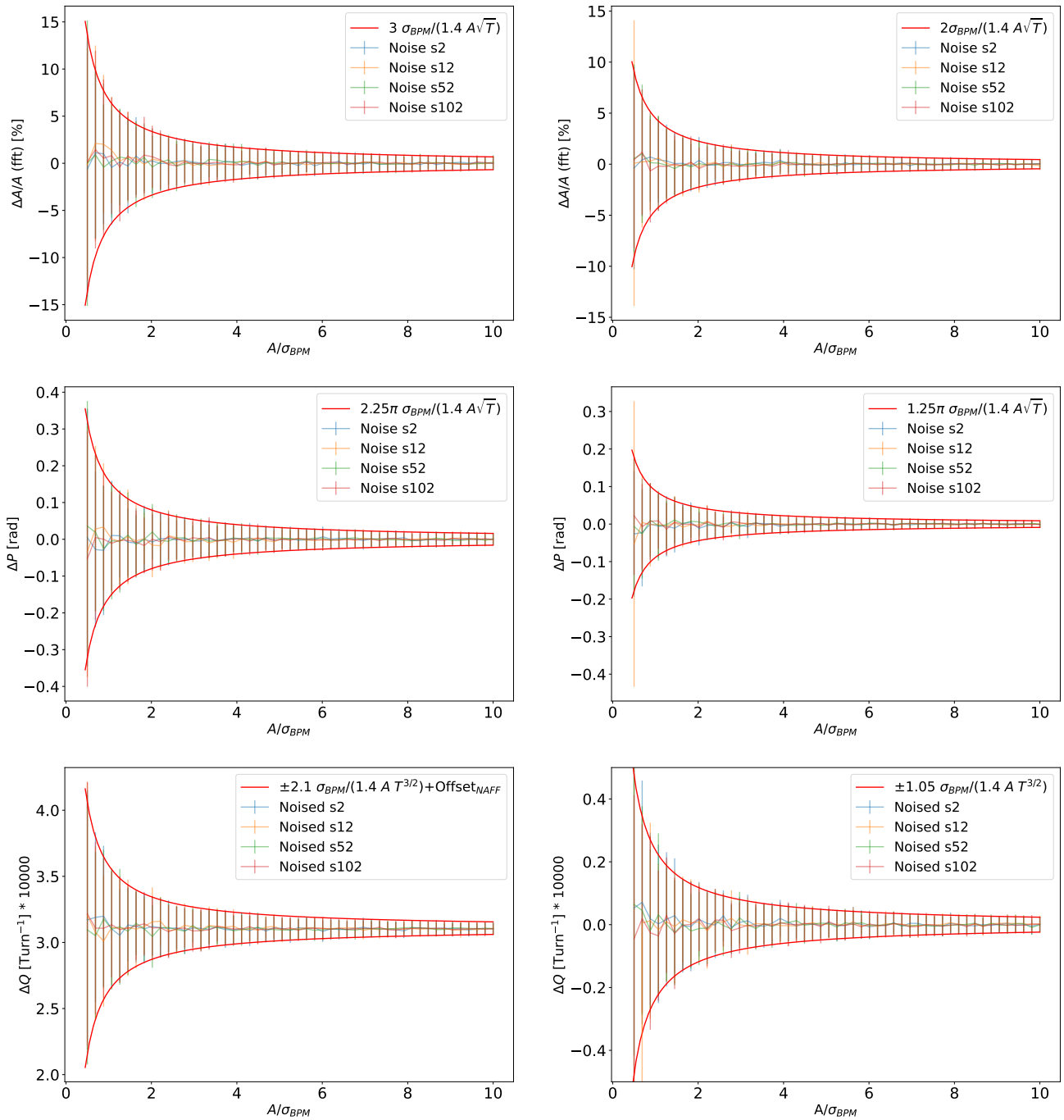

Figure 6.8: Evolution of the spectral line parameters (top: Amplitude, middle: Phase, bottom: Frequency) as a function of the sample size when measured with NAFF (left) or SUSSIX (right).

	$\Delta A/A$	ΔP	ΔQ
NAFF	$\pm 3\frac{\sigma_{BPM}}{1.4A\sqrt{T}}$	$\pm 2.25\pi\frac{\sigma_{BPM}}{1.4A\sqrt{T}}$	$\pm 2.1\times 10^{-4}\frac{\sigma_{BPM}}{1.4A\sqrt{T}} + \text{Offset}_{NAFF}$
SUSSIX	$\pm 2\frac{\sigma_{BPM}}{1.4A\sqrt{T}}$	$\pm 1.25\pi\frac{\sigma_{BPM}}{1.4A\sqrt{T}}$	$\pm 1.05\times 10^{-4}\frac{\sigma_{BPM}}{1.4A\sqrt{T}}$

Clearly, the $1/2J_x$ decrease observed in the RMS of all the LHC BPMs (Fig. 6.5) is correlated to the improvement of the ratio signal over noise. Compared to NAFF, the SUSSIX algorithm gives better results with a gain of a factor 2 in the fit coefficient for the reconstructed tune and phase, and a factor 1.5 for the reconstructed amplitude.

6.3 Machine Development proposal in the LHC with controlled Amplitude Beta-Beating

In this section, we are going to test the theory developed in Sec. 3.6. The aim is to increase on purpose the measured amplitude beta-beating using the octupoles installed in the LHC machine, without first order amplitude detuning. In order to be above the BPM noise level discussed in the previous section, 5% horizontal amplitude beta-beating at $0.01\,\mu$m is used as target value. To do so, we use the same approach as in Section 5.1.4 and solve the system $\vec{h} = \mathbf{A}\vec{K}$ with :

- $\vec{h}$: a vector of target Hamiltonian contributions described in Eq. (3.62) which act on Amplitude detuning and Resonance Driving Terms (at a reference BPM (b)), i.e. $(h_{2200}, h_{1111}, h_{0022}, \Re(f_{3100}^{(b)}), \Im(f_{3100}^{(b)}), \dots)$;
- **A**: a matrix of respectively Amplitude detuning and Resonance Driving Terms coefficients between the source of the b_4 (octupole correctors o_i) and the BPM (b);

$$\mathbf{A} = \begin{pmatrix} \beta_x^2|_{o_1} & \beta_x^2|_{o_2} & \beta_x^2|_{o_3} & \beta_x^2|_{o_4} & \beta_x^2|_{o_5} & \dots \\ \beta_x\beta_y|_{o_1} & \beta_x\beta_y|_{o_2} & \beta_x\beta_y|_{o_3} & \beta_x\beta_y|_{o_4} & \beta_x\beta_y|_{o_5} & \dots \\ \beta_y^2|_{o_1} & \beta_y^2|_{o_2} & \beta_y^2|_{o_3} & \beta_y^2|_{o_4} & \beta_y^2|_{o_5} & \dots \\ \beta_x^2\cos(-2\Delta\phi_x)|_{o_1} & \beta_x^2\cos(-2\Delta\phi_x)|_{o_2} & \beta_x^2\cos(-2\Delta\phi_x)|_{o_3} & \beta_x^2\cos(-2\Delta\phi_x)|_{o_4} & \beta_x^2\cos(-2\Delta\phi_x)|_{o_5} & \dots \\ \beta_x^2\sin(-2\Delta\phi_x)|_{o_1} & \beta_x^2\sin(-2\Delta\phi_x)|_{o_2} & \beta_x^2\sin(-2\Delta\phi_x)|_{o_3} & \beta_x^2\sin(-2\Delta\phi_x)|_{o_4} & \beta_x^2\sin(-2\Delta\phi_x)|_{o_5} & \dots \\ \vdots & \vdots & \vdots & \vdots & \vdots & \ddots \end{pmatrix} \tag{6.7}$$

- $\vec{K}$: a vector of octupole o_i integrated strengths.

In $\vec{h}$, we fix $h_{2200}, h_{1111}, h_{0022}$ to be zeros. The terms $\Im(f_{3100}^{(b)})$ is defined such that it generates the $5\,\%$ horizontal amplitude beta-beating, using the expressions for Ξ_u in Eq. (3.87-3.89). The other terms can be either fixed to zeros or free parameters. As the target values of $\vec{h}$ are fixed at a Reference BPM, the system has a unique solution.

In the LHC, there are three types of octupoles: the main octupoles in the Arc cells used for Landau damping (named MO); the octupole correctors attached to every-other dipoles in the Arc cells (named MCO); and the octupole correctors in the Interaction Regions (named MCOX). Using these types of octupoles, we have defined 3 different configurations of the machine, that are described in the following subsections. The optics used for the tracking simulation is the Injection LHC 2018 with $\beta^* = 11\,\text{m}$ and the particles tracked are on momentum.

6.3.1 Octupolar correctors in IRs and "BPM.34R8.B1" as reference

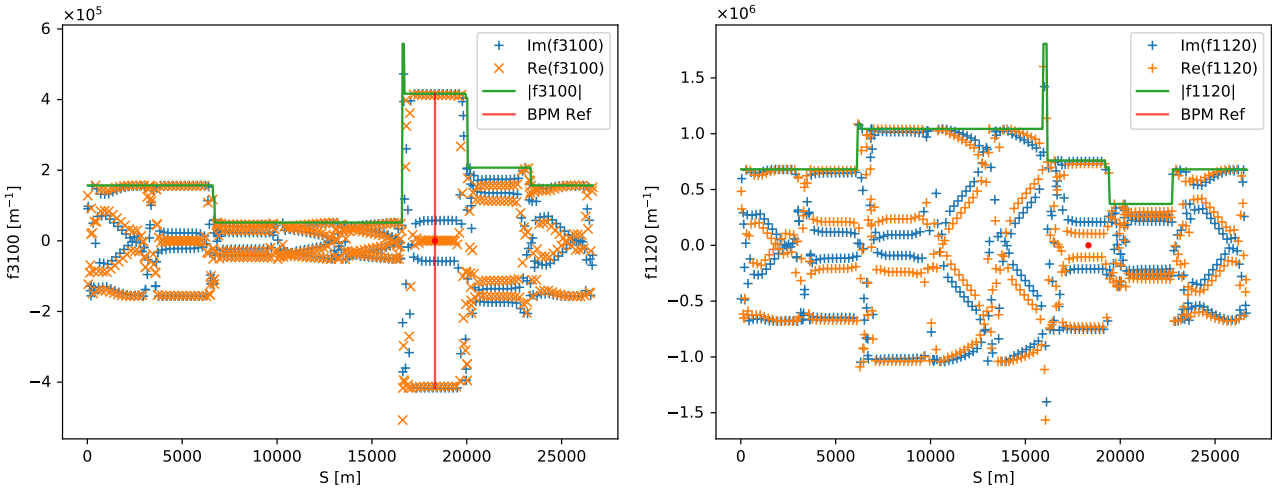

Figure 6.9: Prediction for case 1 of the values of the Resonance Driving Terms f_{3100} (left) and f_{1120} (right) at all the BPM positions. The reference BPM "BPM.34R8.B1" (S$=$ 18 325.04 m) is marked in red.

In the first configuration studied, called HABB case 1, $\vec{h}$ is composed of:

- h_{2200}, h_{1111} and h_{0022} equal to zeros such that they don't generate the direct and cross amplitude detuning;
- the Resonance Driving terms $f^{(b)}_{3100}$ with its real and imaginary parts respectively equal to zeros and $5/12\,\mu\text{m}^{-1}$ such that the direct horizontal amplitude beta-beating increase by $5\,\%$ when the action reach $0.01\,\mu$m;
- the Resonance Driving terms $f^{(b)}_{0031}$ is also set to zero such that the direct vertical amplitude beta-beating is trivial.

All the other Resonance Driving Terms are unconstrained in the inversion of $\vec{h} = \mathbf{A}\vec{K}$. The reference BPM, called "BPM.34R8.B1", is at the position S$=$ 18 325.04 m. It is located near the middle of the arc between the IP8 and IP1. Figure 6.9 shows only the values of the Resonance Driving Terms related to the direct (f_{3100}) and cross (f_{1120}) amplitude beta-beating when the action increase in the x-plane. Those values are plot for each BPMs across the LHC and the reference BPM is marked in red (if the Resonance Driving Term is let free, only red dot is shown at the BPM position). Since the vector $\vec{h}$ has a size of 7 in this case (3 for the Amplitude Detuning terms and 2×2 for the

Table 6.1: Integrated strength (K in m^{-3}) of octupole correctors for case 1.

Name	MCOX3.L5	MCOX3.R5	MCOX3.L8	MCOX3.R8	MCOX3.L1	MCOX3.R1	MCOX3.R2
K	1739.11	-207.69	1468.17	-2142.16	-148.01	-1384.10	680.42

Resonance Driving Terms), we choose to use only the octupole correctors (MCOX) in IR1, IR2, IR5 and IR8. Their respective integrated strengths are reported in Table 6.1.

Figure 6.10 shows how both beta-beating vary across the LHC when the horizontal action increases using the configuration of octupolar correctors mentioned before (see Table 6.1). The tracking simulation where made using SixTrack and the position at each BPMs are analysed with the BetaBeat.src code. The color of the dots corresponds to the particle action given by BetaBeat.src. As the action is computed using the linear approximation, as discussed in Sec. 3.7, it is noted as $2J_x$.

With this octupole configuration, the model and the simulation agree pretty well for the direct Amplitude Beta-Beating ($\Delta\beta/\beta_x$) even at high action. Three regions of the LHC have visible different behaviour (corresponding to

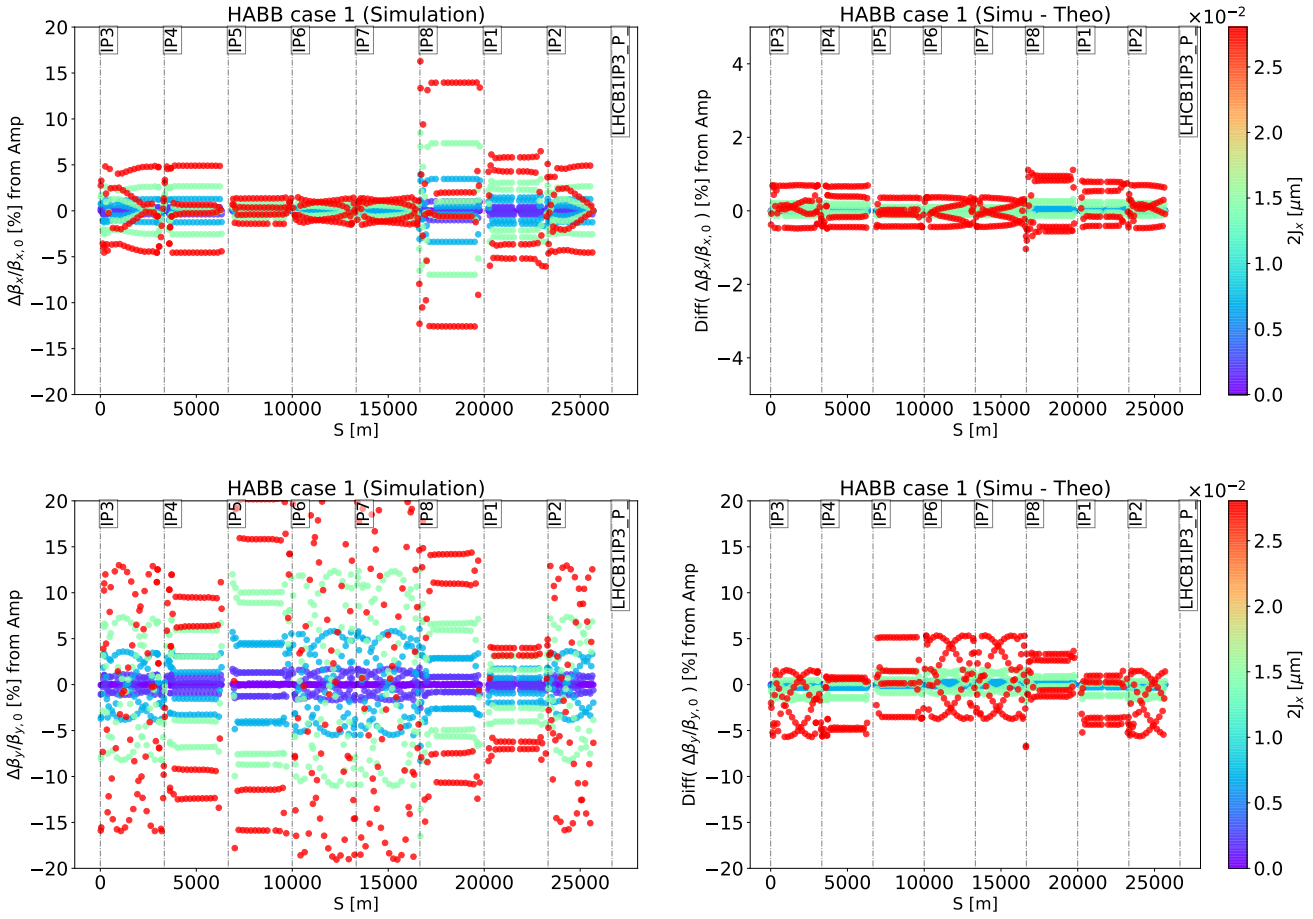

Figure 6.10: Direct (top) and cross (bottom) Amplitude Beta-Beating from spectral line amplitude for case 1. On the left are the results of the simulations, and on the right the difference between the simulations and Ξ_u from Sec. 3.6. The action (noted $2J_x$) is the average over BPMs measured from spectral line amplitude.

three direct ABB values): from Interaction Point IP8 to IP1, from IP1 to IP5 and from IP5 to IP8. The first region has strongest direct Amplitude Beta-Beating, the smallest value is in the third region. It is interesting to note that IP1, IP5 and IP8 are the region where the strongest correctors are located.

The simulated cross Amplitude Beta-Beating ($\Delta\beta_y/\beta_y$) also agrees well with the theory for low action, but a discrepancy appears at high action. The three regions observed previously, are not clearly defined here. But it can still be noted that the cross Amplitude Beta-Beating is smaller between IP1 and IP2. As a reminder, f_{2011} is not minimized in this case.

6.3.2 Octupolar correctors in IRs and "BPM.34R3.B1" as reference

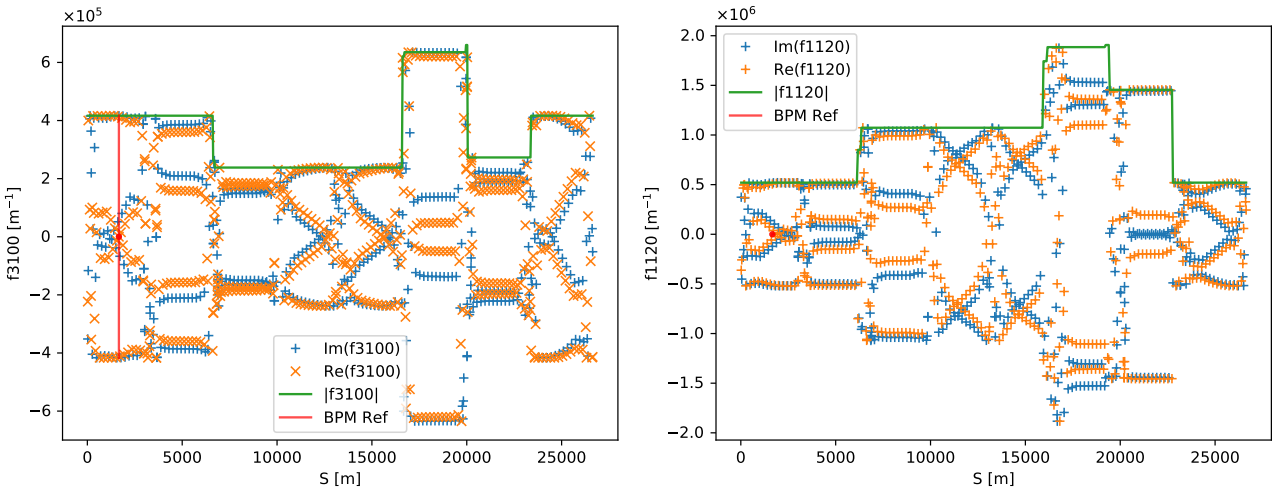

Figure 6.11: Prediction for case 2 of the values of the Resonance Driving Terms f_{3100} (left) and f_{1120} (right) at all the BPMs position. The reference BPM "BPM.34R3.B1" (S= 1663.60 m) is marked in red.

The second configuration studied, called Amplitude Beta-Beating axe X case 2, is very similar to case 1 but we decide to choose a different reference BPM in order to check how the machine responds. In this case, the reference BPM is "BPM.34R3.B1" at the position S= 1663.60 m. It is located near the middle of the arc between the IP3 and IP4. Similarly to the previous subsection, the Resonance Driving Terms responsible for the direct and cross Amplitude Beta-Beating are shown in Figure 6.11 for all the BPMs across the LHC. Once again, only the octupole correctors in IR1, IR2, IR5 and IR8 are used. Their respective integrated strengths are shown in Table 6.2.

Table 6.2: Integrated strength (K in m^{-3}) of octupole correctors for case 2.

Name	MCOX3.L5	MCOX3.R5	MCOX3.L8	MCOX3.R8	MCOX3.L1	MCOX3.R1	MCOX3.R2
K	-1383.16	-600.26	-1516.33	-266.81	-277.32	2243.62	1799.75

Figure 6.12 shows how both beta-beating vary across the LHC when the horizontal action increases using the configuration of correctors mentioned before (see Table 6.2). In this case, the direct Amplitude Beta-Beating is almost the same along the machine compared to case 1 in which most of the direct ABB is concentrated between

IP8 and IP1. Also, the section with the lowest cross Amplitude Beta-Beating amplitude is now between IP2 and IP5. Regions delimited by the strongest octupoles can still be seen.

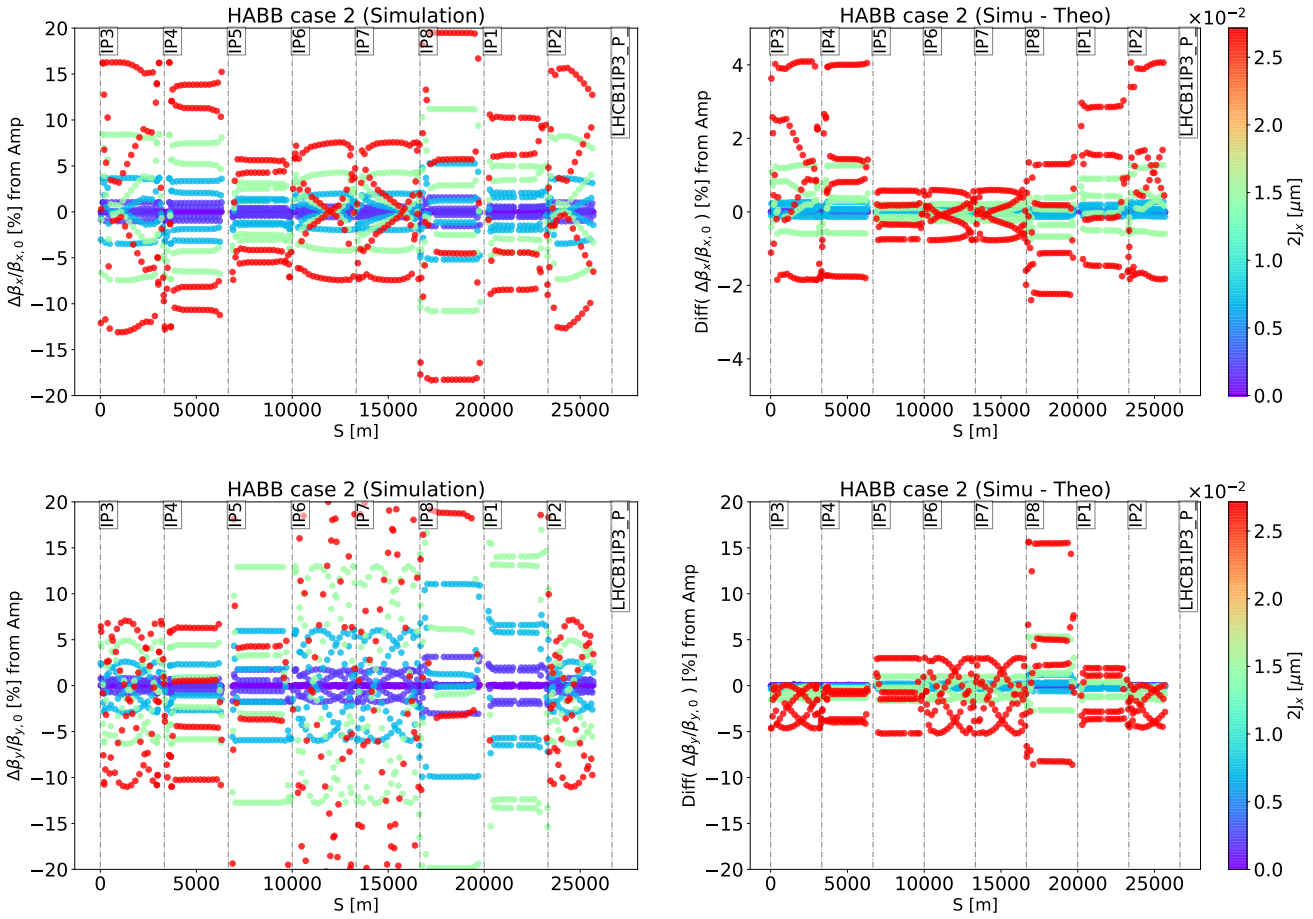

Figure 6.12: Direct (top) and cross (bottom) Amplitude Beta-Beating from spectral line amplitude for case 2. On the left are the results of the simulations, and on the right the difference between the simulations and Ξ_u from Sec. 3.6. The action (noted $2J_x$) is the average over BPMs measured from spectral line amplitude.

As the action increases, a discrepancy between the prediction from the model and the simulation appears, in particular between the IP2 and IP4. For the cross Amplitude Beta-Beating, a phenomena equivalent to an offset can be observed between IP3 and IP5 which is not predicted by the theory. This configuration generates a strong ABB across the accelerator and particularly between IP8 and IP1 where it can reach a direct and cross Amplitude Beta-Beating of respectively 10 and $20\,\%$ or more around an action of $0.01\,\mu$m.

6.3.3 Octupolar correctors in the IRs and in the Arcs, and "BPM.34R3.B1" as reference

In the third configuration studied, called HABB axe X case 3, the goal is to check if constraining all octupolar Resonance Driving Terms while solving $\vec{h} = \mathbf{A}\vec{K}$, improve the Beam dynamic. The reference BPM is the same as in case 2, ("BPM.34R3.B1"). The Resonance Driving Terms responsible for the direct and cross Amplitude

Table 6.3: Integrated strength (K in m^{-3}) of octupole correctors for case 3.

Name	MCOX3.L5	MCOX3.R5	MCOX3.L8	MCOX3.R8	MCOX3.L1	MCOX3.R1	MCOX3.R2
K	41.16	157.02	1790.83	-132.91	57.64	-1029.57	-861.83
Name	MOF.A34B1	MOF.A45B1	MOF.A67B1	MOF.A78B1	MOF.A12B1	MOF.A23B1	
K	-482.22	603.50	40.75	-180.60	247.70	-248.26	
Name	MOD.A34B1	MOD.A45B1	MOD.A67B1	MOD.A78B1	MOD.A12B1	MOD.A23B1	
K	-482.22	603.50	40.75	-180.60	247.70	-248.26	
Name	MCO.A34B1	MCO.A56B1	MCO.A67B1	MCO.A81B1	MCO.A12B1	MCO.A23B1	
K	92.48	-248.54	66.49	-35.61	-153.18	266.23	

Beta-Beating when the horizontal action increases, are shown in Figure 6.13. In this case, all the octupole types are needed in order to constrain all the octupolar Amplitude Detuning and Resonance Driving Term contributions. Their respective strengths are shown in Table 6.3. Figure 6.14 shows how both beta-beating vary across the LHC when the horizontal action increases.

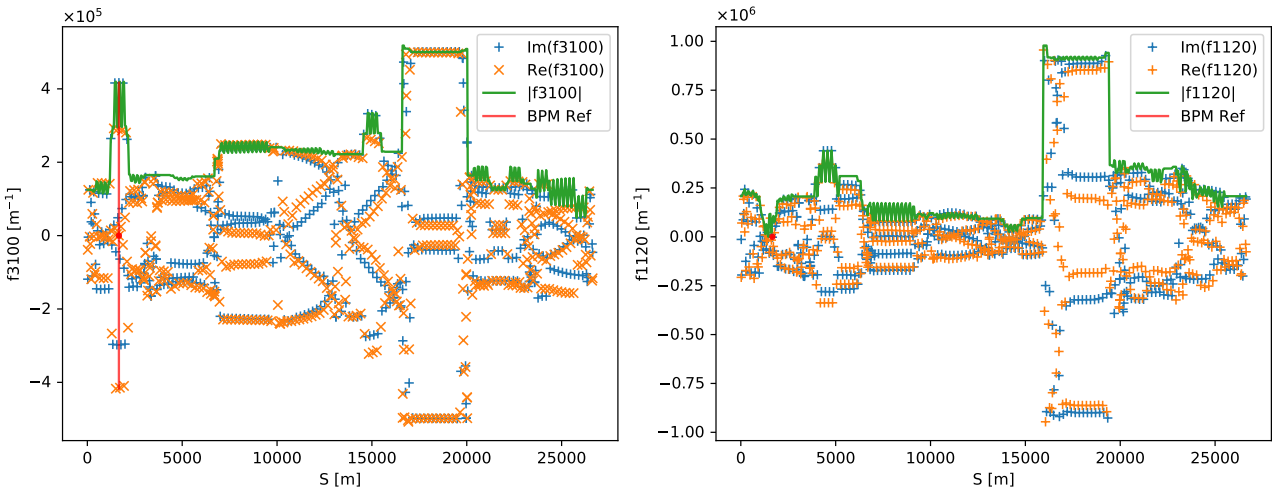

Figure 6.13: Prediction for case 3 of the values of the Resonance Driving Terms f_{3100} (left) and f_{1120} (right) at all the BPMs positions. The reference BPM "BPM.34R3.B1" (S$=$ 1663.60 m) is marked in red.

In this case, both direct and cross Amplitude Beta-Beating are the strongest between IP8 and IP1 where it can be expected to reach a bit more than $10\,\%$ ABB around an action of $0.01\,\mu$m. Around the reference BPM (between IP3 and IP4), the value of the direct Amplitude Beta-Beating change a lot. This can be explained by the presence of correctors used to constrain the Resonance Driving Term all across this section.

Here, the discrepancy between the simulation and the theory is more evident as the action increases with respect to previous cases. Only the direct Amplitude Beta-Beating in the arc between IP8 and IP1 is still relatively well predicted. At high action, the discrepancy is more an oscillation and an amplification of the predicted direct and cross ABB.

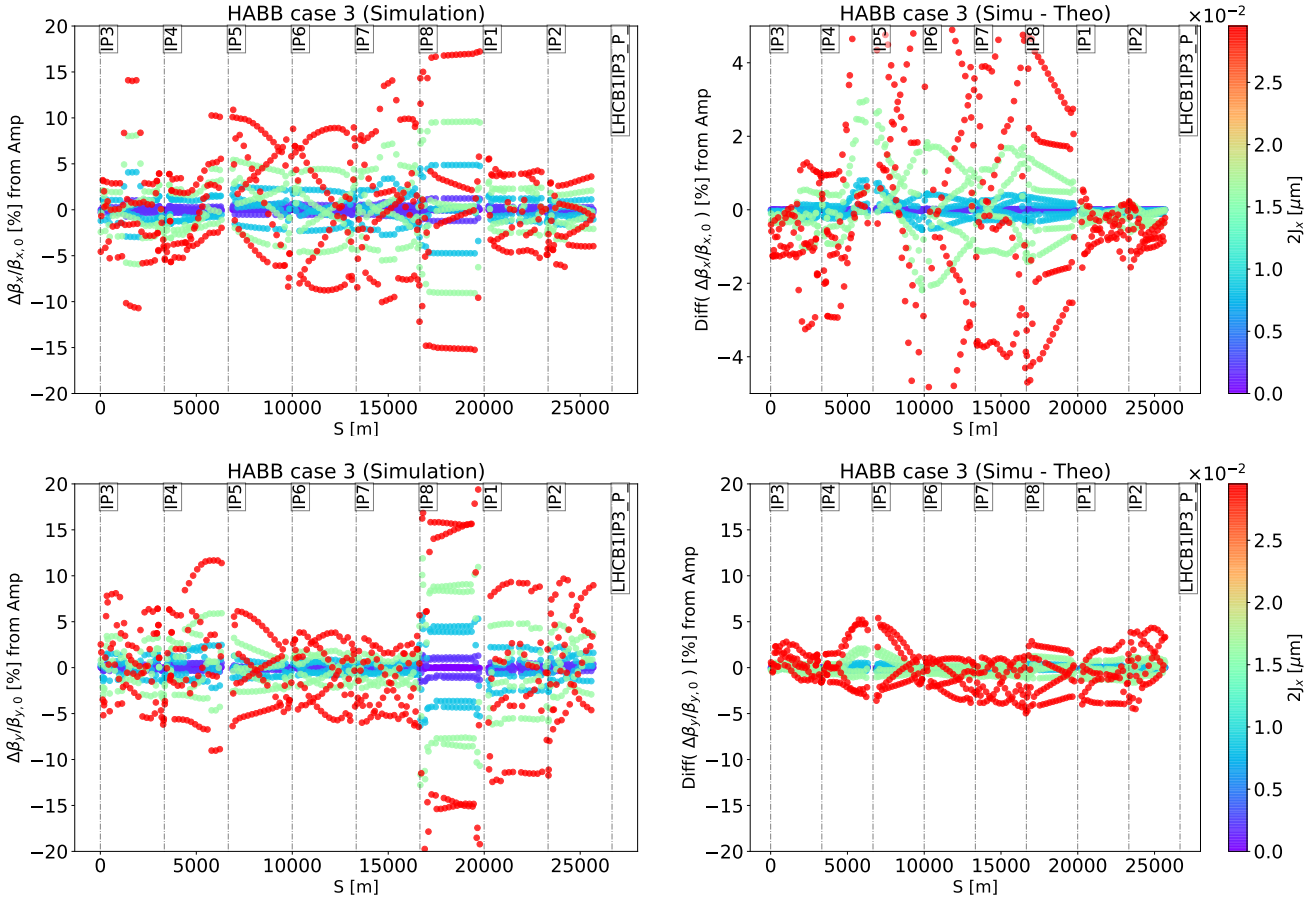

Figure 6.14: Direct (top) and cross (bottom) Amplitude Beta-Beating from spectral line amplitude for case 3. On the left are the results of the simulations, and on the right the difference between the simulations and Ξ_u from Sec. 3.6. The action (noted $2J_x$) is the average over BPMs measured from spectral line amplitude.

6.3.4 Comparison between tracking simulations and theory for the different configurations

Figure 6.15 shows the direct and cross amplitude detuning for the three simulated cases. No linear amplitude detuning generated from the octupole 1st order is observed as expected but the octupole 2nd-order is clearly visible, particularly in the cross Amplitude detuning. In the Case 3, a 3^{rd}-order amplitude detuning can also be seen. This can change the values of the Resonance Driving Terms by an order of 1-2 $\%$. This has been taken into account by using the reconstructed tune instead of the model one, in equation (3.62).

Figure 6.16 shows the evolution of horizontal and vertical beta-beating measured at the reference BPMs, as a function of the horizontal action. The linear direct and cross Amplitude Beta-Beating is well predicted by the theory. The discrepancy observed could be explained by the octupole 2nd-order Resonance Driving Terms which act as dodecapolar RDTs, as shown in [71]. This possibility has not been implemented in our analytical code yet.

Figure 6.17 shows how horizontal and vertical RMS beta-beating vary as the horizontal action increases. Both beta-beating have a very linear behaviour, as we would expect having octupolar errors. The second order Amplitude

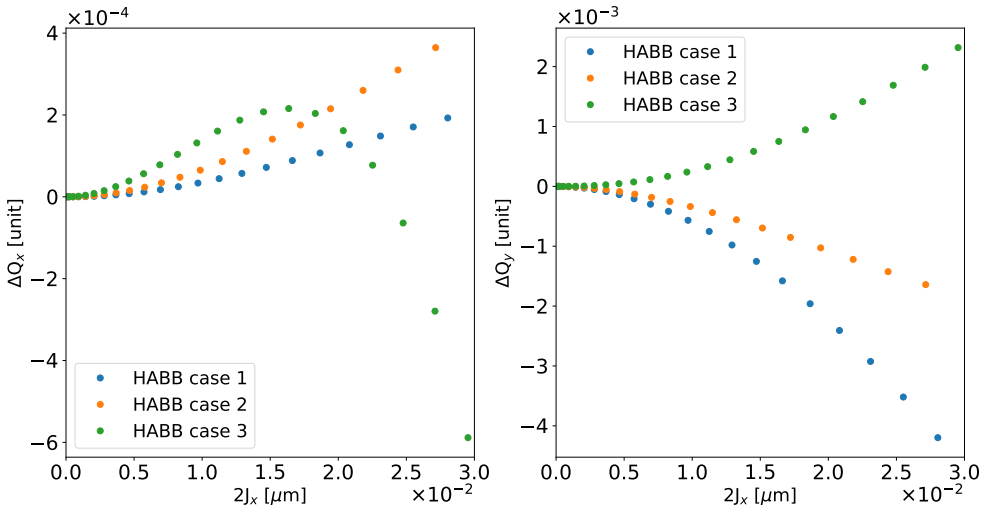

Figure 6.15: Direct (left) and cross (right) amplitude detuning for both cases.

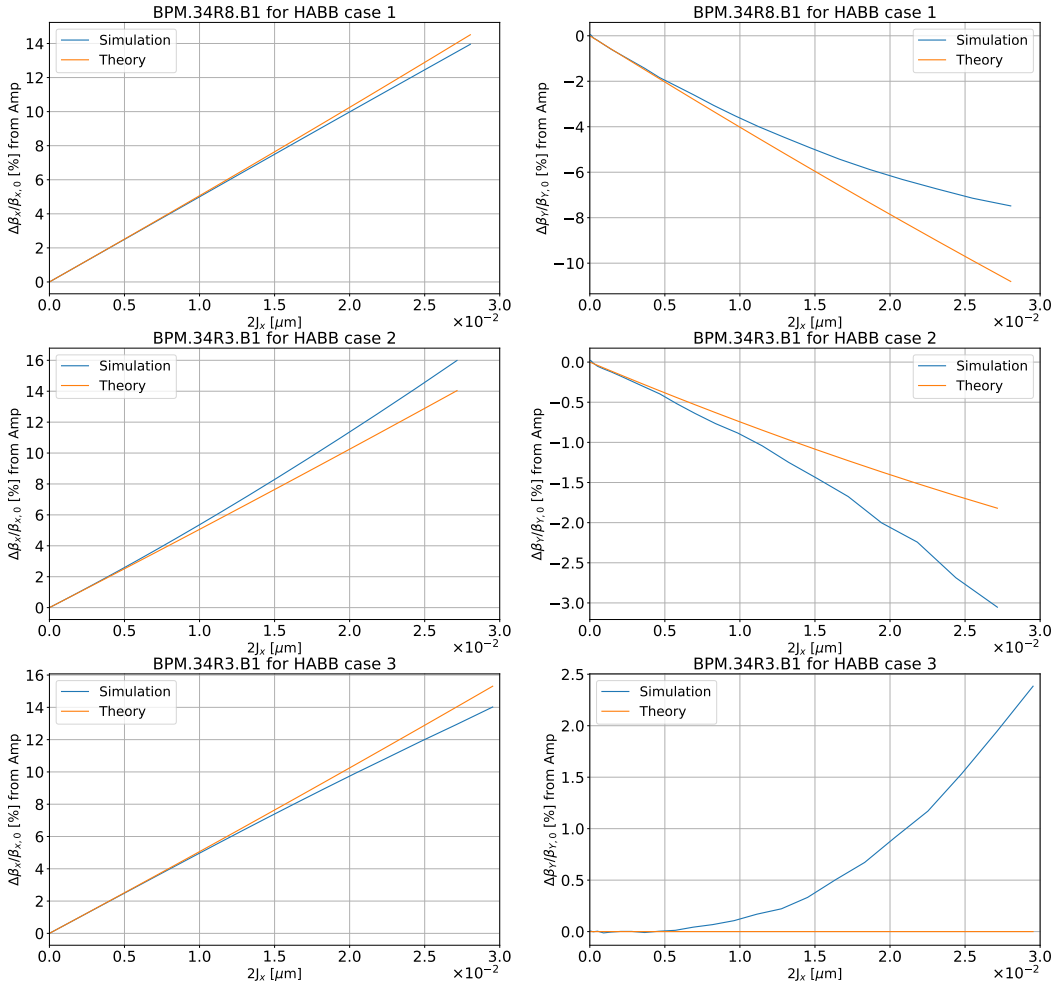

Figure 6.16: Direct (left) and cross (right) Amplitude Beta-Beating from spectral line amplitude at the reference BPM named ”BPM.34R8” for case 1 and ”BPM.34R3” for cases 2 and 3.

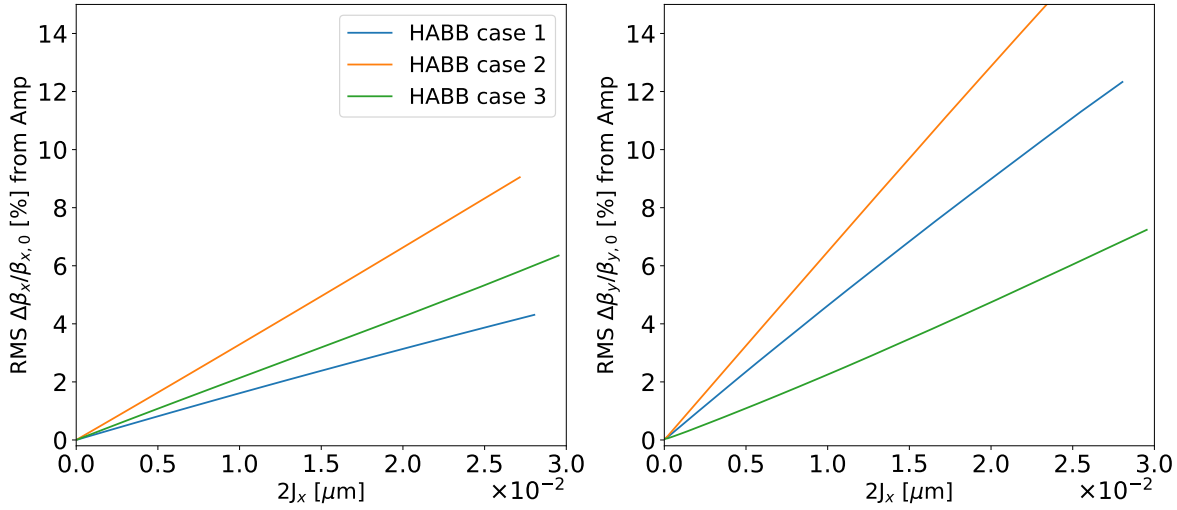

Figure 6.17: Direct (left) and cross (right) RMS Amplitude Beta-Beating from spectral line amplitude.

Beta-Beating observed at the BPM doesn't appear here. It can also be noted that even if the same constraints are imposed (case 1 and 2), the evolution of the RMS beta-beating with the action can be very different and the goal of $5\,\%$ horizontal beta-beating at $0.01\,\mu$m is not necessarily reached in the RMS beta-beating.

Up to now, we have only studied the amplitude beta-beating when it is computed from the spectral line amplitude. Another method is possible using the phase advance between 3 BPMs[1] with the following relation:

$$\left(\frac{\Delta\beta_{u,1}}{\beta_{u,1}}\right)_P = \frac{\cot\left(\Delta\mu_u^{me}(s_2,s_1)\right) - \cot\left(\Delta\mu_u^{me}(s_3,s_1)\right)}{\cot\left(\Delta\mu_u^{mo}(s_2,s_1)\right) - \cot\left(\Delta\mu_u^{mo}(s_3,s_1)\right)} - 1 \tag{6.8}$$

with $\Delta\mu_u(s_j,s_k)$ the phase advance between the BPMs j and k. Figure 6.18 shows how the direct beta-beating computed from the phase of the main spectral line and its discrepancy with respect to the one computed from the amplitude of the main spectral line, vary across the LHC for the three configurations studied. We are still working on the theory for this measurement method of the amplitude beta-beating. Using Eq. (6.8) for the reconstruction of the beta-beating has many limits. First of all, if the phase advance between the BPMs is $\sim 90^\circ$ or if $\Delta\mu_u^{mo}(s_2,s_1) \sim \Delta\mu_u^{mo}(s_3,s_1)\ mod(2\pi)$, the measurement is greatly sensible to the noise. Secondly, Eq. (6.8) work really well when there are no non-linear error between the BPMs.

Nonetheless, since the two methods should behave similarly, using the difference between them could be used to detect local errors. In fact, the major differences between the methods are where the strongest octupoles are located, as shown in Fig. 6.18.

[1] The results could be improved using the N BPMs methods.

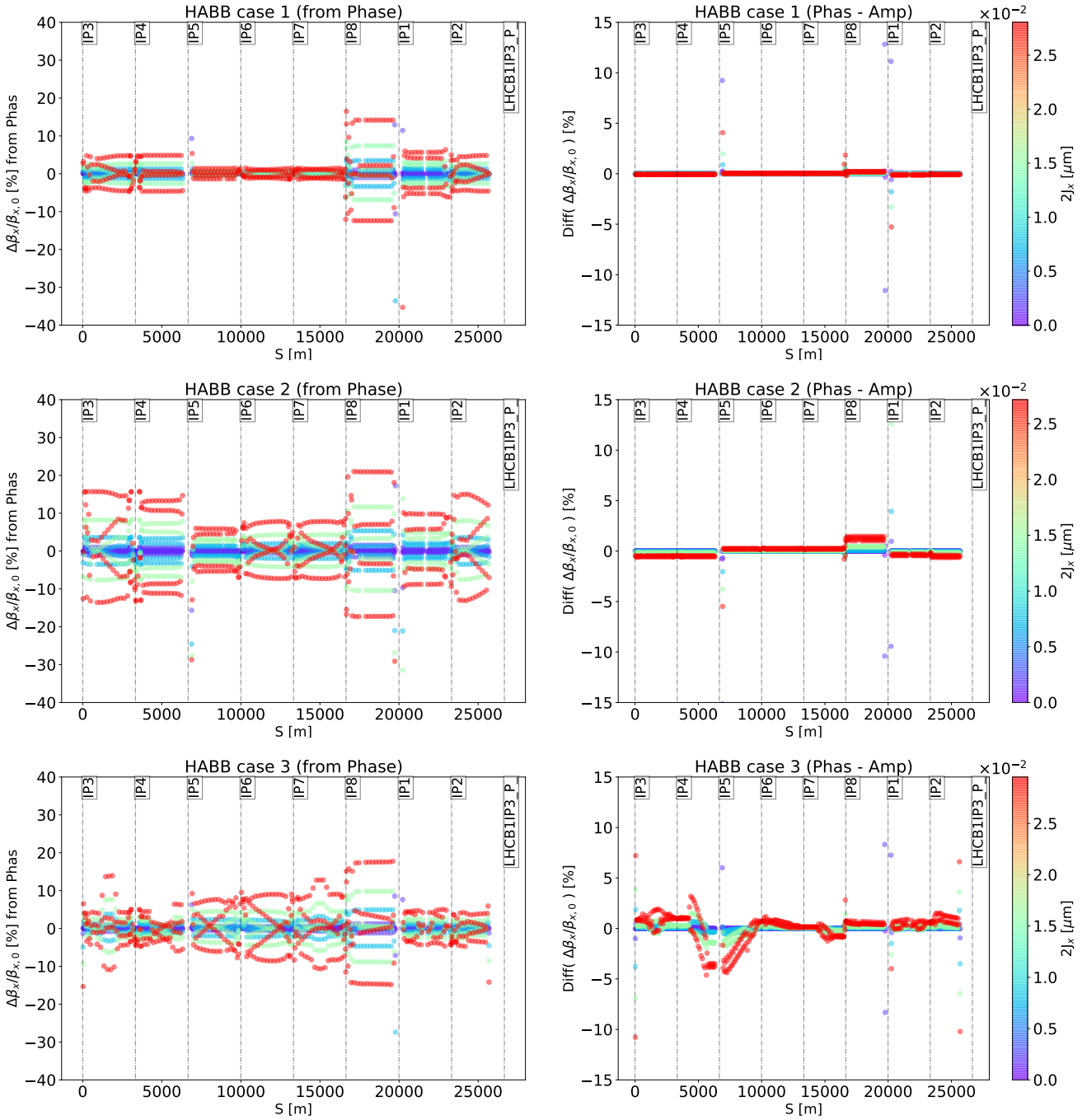

Figure 6.18: Direct Amplitude Beta-Beating from spectral line phase (left) and its difference with the Amplitude Beta-Beating computed from the spectral line amplitude (right). The results are shown for the 3 different cases.

***

In this chapter, we have evaluated the impact of the HE+Heads model on the variation of the measured beta-function with the particle amplitude. Using tracking simulations for the HL-LHC project, we found that the effect is very small (of the order of few per cent). When looking at the LHC machine development data, we show that this effect can be hardly seen given the present Beam Position Monitors noise levels. The possibility to enhance the

variation of the measured beta-function with the amplitude of the particle is studied using different octupole corrector configurations of LHC and compared with the theory developed in chapter 3. The limits of the theory and of the procedure to enhance the measured amplitude beta-beating are discussed.

In the following and last chapter, we study the impact of the 3D realistic magnetic field description on the third observable, i.e. Dynamic Aperture. No analytic description of this observable is possible. Contrary to detuning and beta-beating that vary according to even multipole and multipole-like errors, the Dynamic Aperture is a cumulative effect of all the multipoles errors present in the accelerator and their mutual interference.

Chapter 7

Dynamic aperture

Dynamic aperture (DA) is a quantity often used to define the performance of an accelerator against magnets imperfections. It is defined as the area of the stable phase-space region spanned by a particle in an accelerator and it is evaluated using particle tracking simulations [72] or measured by different techniques [73].

In this chapter, we study the impact of the three different models described in section 4 on the computation of Dynamic Aperture, focusing in particular on the effect of the b_6 correctors. In the first section, the impact of the number of generalized gradient derivatives on DA is discussed. In the second section, the impact of the 3 models on Dynamic Aperture is studied for different angles in the x-y plane. Finally, in the last section, we study their impact on the time evolution of the DA. In both case, we also observe what happen when the non-linear correctors are applied.

The Dynamic Aperture is computed simulating the particles motion over 10^4 revolutions with initial conditions distributed on a polar grid, so as to have 30 pairs of particles (different initial conditions) for each interval of 2σ (beam size[1]) from 0 to 28. Eleven angles in the x-y phase space are scanned, where x and y are in units of linear beam dimensions. The initial momentum offset δ is set to 27×10^{-5} (which is equivalent to 2/3 of the LHC RF bucket design). The Dynamic Aperture values are defined as the initial amplitudes (in number of beam size σ) of particles lost in 10^4 turns. This procedure for the DA simulations is the same used for LHC DA studies [74] and it was found to provide a precision of about 0.5 beam σ at 10^5 turns [75]. Since in the machine configurations we study in this paper the Dynamic Aperture converges very quickly to its asymptotic value, we expect the same type of precision in the DA results for this comparison between models.

[1] The relation between σ and the particle action in the normalized phase-space $2J_u$ is: $\sigma = \sqrt{2J_u}$.

7.1 Impact of the Generalized Gradient derivatives on beam stability

As discussed in section 4, in the case of Lie2 the numbers of gradients derivatives can be specified in the reconstruction of the vector potential used for the tracking. Figure 7.1 shows the impact of different number of derivatives on Dynamic Aperture. All 60 seeds and the line joining the minimum value for each angle are shown on the left panel, while the comparison for one configuration of the machine is shown on the right. All derivatives above the second do not change Dynamic Aperture, meaning that only the first two derivatives can be used. Finally, even these first two derivatives have very small impact on the Dynamic Aperture.

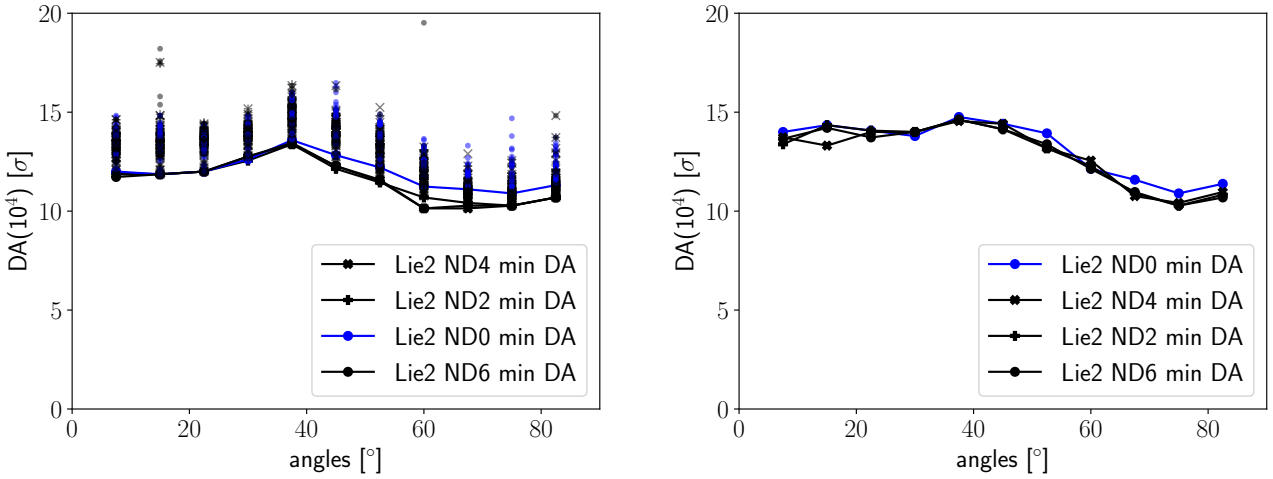

Figure 7.1: Dynamic Aperture as a function of phase space angles (with b_6 correction) for different numbers of gradients derivatives considered in the Lie2 model. All the 60 seeds simulated are shown on the left, while the comparison for one configuration of the machine is shown on the right.

7.2 Impact of the model on Dynamic Aperture as a function of angles in the x-y space for HL-LHC

The Dynamic Aperture values for the eleven x-y space angles scanned in the simulations are shown in Fig. 7.2 for one configuration of the machine. The cases without and with b_6 correction are compared. Dynamic Aperture without b_6 correction is pretty similar for all the model in the pure x and y axis, while it can differ up to 3 σ at around 40°. The impact of b_6 correction is different according to the model considered. There is no improvement in Dynamic Aperture for the HE+heads model while can be significant for the HE or Lie2, according to the angle.

The statistics of all the 60 different configurations of the machine simulated is shown in Fig. 7.3. Dots represent the values corresponding to the 60 seeds, while the continuous line joins the minimum Dynamic Aperture values for each angle. All high order fields errors are considered and correction for b_3, b_4, b_5, a_3, a_4, a_5 of the inner triplets, as well as b_3, b_4, b_5 of the arc dipole, are applied. The b_6 correction is included in the results shown in the right panel

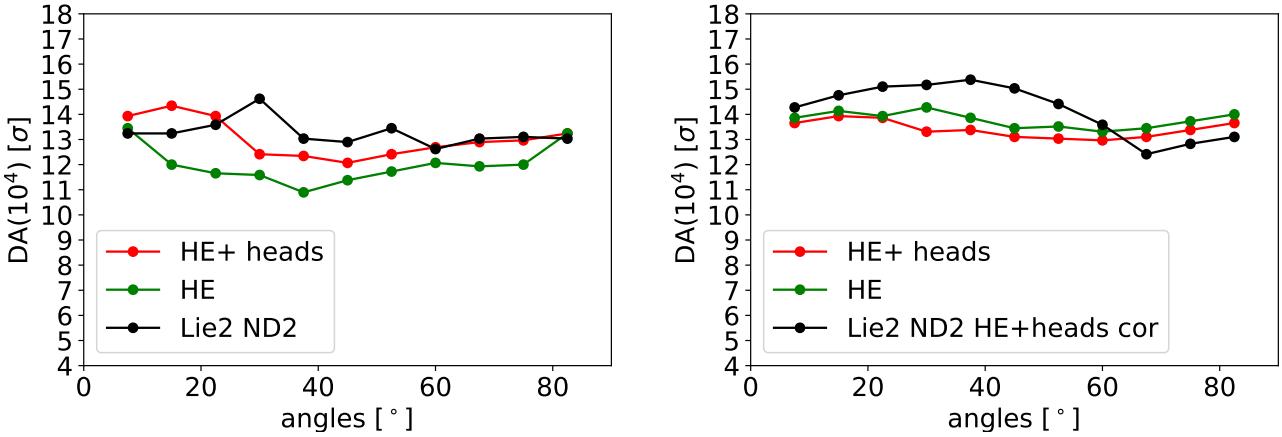

Figure 7.2: Dynamic Aperture at 10^4 as a function of x-y space angles with b_6 correctors OFF (left), and with b_6 correctors ON (right) for one configuration of the machine. The HE+Heads model has been used to compute correction of b_6 in the case of Lie2 ND2 tracking.

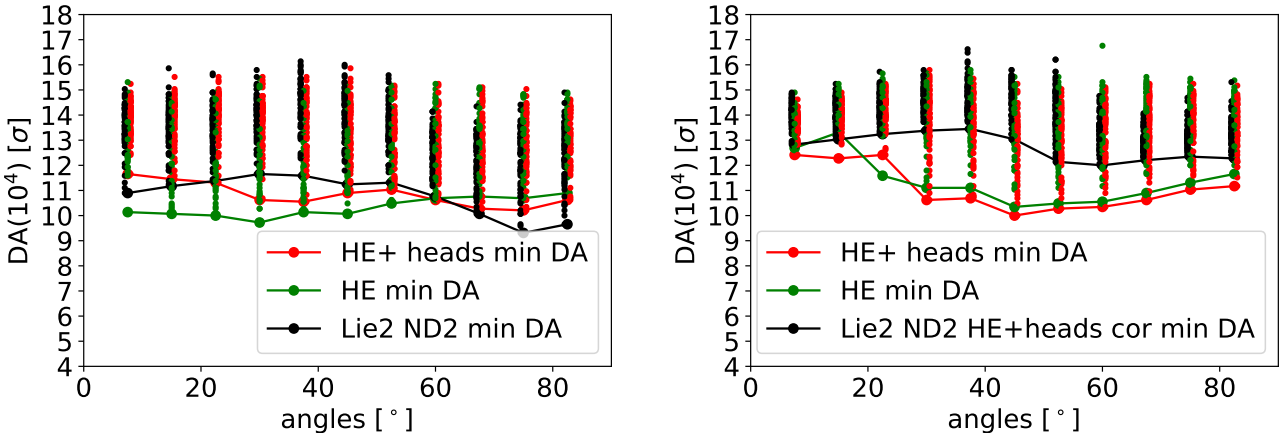

Figure 7.3: Dynamic Aperture at 10^4 as a function of phase space angles with b_6 correctors OFF (left), and with b_6 correctors ON (right). Dots represents the 60 different configurations of the machine according to random component of the magnets errors.

of Fig. 7.3. Its effect on Dynamic Aperture is slightly different according to the angle and the model. A major positive impact of b_6 correction is visible towards the horizontal plane for the HE model. When the HE+ Heads model is considered the gain in Dynamic Aperture is smaller, and in particular the correction does not improve DA for angles around 40°. In the case of the Lie2 model the correction gives a positive impact toward the vertical plane. Averaging over the angles, the impact of the b6 correction is of 0σ for the HE+Heads model, 1σ for the HE model and 2σ for the Lie2 model. Finally, a difference between Lie2 model and the two others is visible at 40° when looking at all machine configurations.

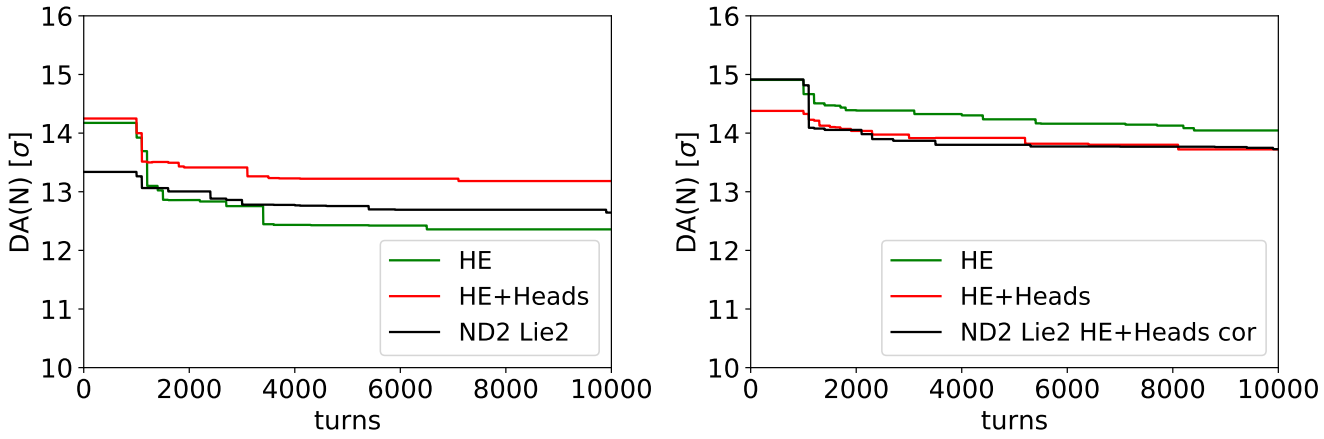

Figure 7.4: Dynamic Aperture as a function of particle revolutions (turns) with b_6 correctors OFF (left), and with b_6 correctors ON (right) for one machine configuration. The HE+Heads model is used to compute the correction in the Lie2 ND2 case.

7.3 Evolution of the Dynamic Aperture with number of revolution

Starting from the ensemble of initial amplitude of particles losts in the x-y phase space, which define the Dynamic Aperture shown in the previous section, the DA as a function of turns can be defined as [73]:

$$DA(N) = \frac{2}{\pi} \int_0^{\pi/2} r_s(\theta; N)\, \mathrm{d}\theta \tag{7.1}$$

where N is the number of revolutions of the particle in the accelerator (called turns), r_s is the last stable particle (disregarding stability islands non-connected to the origin) and θ is the angle in the x-y phase space. Thus, a value of DA can be calculated for each turn, which is shown in Fig. 7.4 for one configuration of the machine. In this configuration of the machine (seed), the Lie2 model maintains a higher DA value for longer numbers of turns (above 2000). The impact of the b_6 correction varies according to the model as in the case of the DA vs angle. Once again when the b_6 correction is applied no improvement in the Dynamic Aperture evolution is visible for the HE+Heads model.

Figure 7.5 shows statistics from the 60 different machine configurations. As for the case Dynamic Aperture at 10^4 revolutions as a function of the angle, the random part of the errors dominates over the systematic part, resulting in much less difference between the models when looking at their mean values. The only significant difference seems to be on the spread between the minimum and maximum DA values, which is reduced in the Lie2 model, as one can also glimpse in Fig. 7.3.

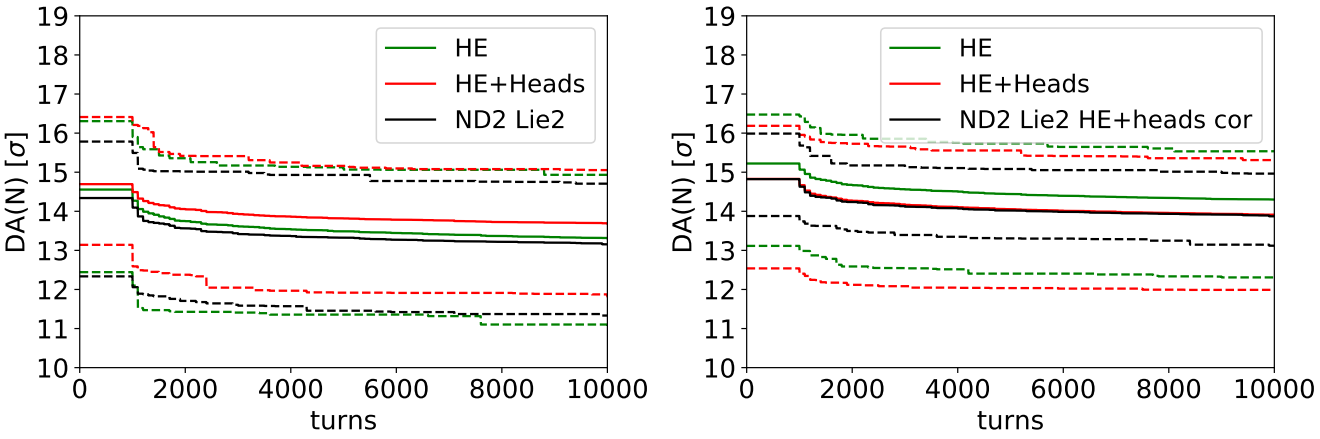

Figure 7.5: Dynamic Aperture as a function of particle revolutions (turns) with b_6 correctors OFF (left), and with b_6 correctors ON (right). The minimum and maximum (dashed lines) together with the mean values (full lines) over 60 different configurations of the machine according to random component of the magnets errors are shown for each model.

***

In this chapter, the impact of the 3D realistic magnetic field of the HL-LHC inner triplet magnet has been quantified on the Dynamic Aperture. The effect is small and well inside the spread in the DA values given by the random component of the multipole errors. Nevertheless, The different model predict a different impact of the dodecapole corrector of about 2σ. In particular, the Hard Edge model is the one that provides less efficient correction, suggesting that the effect of the Fringe Field could provide compensation of resonances excitation.

Conclusion

The main goal of this thesis is to quantify the impact of the quadrupole fringe fields on the protons beam dynamics of LHC upgrade in Luminosity. We focus our studies on the final focus quadrupoles of the high luminosity insertions of LHC and HL-LHC. They are the main sources of non-linearities at collision energy and the variation of the beta function along these magnets is not small. As discussed in chapter 2, the concept of Fringe Field has diverged from its former definition to be only the magnetic field B_z. Using the 3D vector potential from generalized gradients defined in Ref. [3], an analytic expression for Amplitude Detuning and RDTs have been derived, for the first time. The measurements of Amplitude Detuning and RDTs during commissioning of the accelerator are used to measure the effective strength of high order harmonics seen by the beam in the accelerator, and to estimate correctors values. In this thesis, we have also explored the possibility to use a new beam-based observable to measure and correct local sources of non-linear errors. An analytic expression of the non-linear variation of the beta-beating measurement with the action, called amplitude beta-beating, have been derived for the first time. The analytical studies have been complemented with numerical simulations of particle tracking in the accelerator.

For these simulations, an accurate, symplectic and efficient non linear transfer map have been derived for the representation of the quadrupole vector potential and implemented into the CERN tracking code, SixTrack. This new transfer map has been compared to 2 other representations of the magnetic field: the Hard-Edge model with a uniform distribution of the harmonics along the magnet; and the Hard-Edge with Heads model, similar to the Hard-Edge model but with two additional Kicks in the magnet ends. This allows to quantify the impact of the 3D distribution of the magnetic fields on beam dynamics. We consider three beam based observable: the amplitude detuning with the correctors strength, the amplitude beta-beating, and the dynamic aperture.

Applied in the case of HL-LHC project, the impact of the 3D magnetic field distribution is not negligible and has to be taken into account, especially when comparing computed with beam based measured values. The impact on the b_6 corrector strength can be up to about 13% with respect to the present corrector specification. The impact of the first and second derivatives of the quadrupole field (octupole-like) accounts for 4% of present octupole corrector specification. The modification to the corrector strength is in the present design specification, so no big impact is expected from the design point of view. State of art measurements of Dynamic Aperture in the LHC presents an

agreement in the order of $20\,\%$ [76] with respect to prediction by numerical simulations using measured integrated values of non-linearities. This value is higher than the difference found between the Dynamic Aperture prediction from the different models in the case of HL-LHC. In particular, being able to reproduce accurately the longitudinal profile of each of the harmonics of the final focus magnets is more important than higher order derivatives.

The possibility to see the effect of the 3D magnetic field distribution on the LHC beam-based measurements has also been studied. In particular in the case of the amplitude detuning and beta-beating measurements. During the LHC commissioning while using amplitude detuning and feed-down data, the beam based values for the octupole corrector strengths have been estimated for both side of the ATLAS and CMS interaction points (respectively IP1 and IP5). A discrepancy is found between beam-based values for the octupole correctors and predicted ones from magnetic field measurements [5]. This has triggered us to reconstruct a machine-like 3D model of the magnet including the coil, the collar, the yoke as well as the Beam Screen. This has only been possible for the Q_3 and Q_1 final focus quadrupole of LHC, which are called MQXA type magnets. The simulations agree quite well with the KEK measurements of the Connector Side (Lead End). It appears that the LHC ellipsoidal Beam Screen not only add a b_4 harmonics along the magnet (as previously reported) but also the b_6. Its contribution doesn't necessarily sum in the same way in the body and the in connector side. Unfortunately, the Q_1 simulation with the Beam Screen never converged so the same values as the Q_3 have been used for its heads in our analysis. Also, no mechanical drawing for the Q_2 have been found so only the Hard Edge model have been used for the Tracking simulations. Our analysis of the impact of the Fringe Field on the amplitude detuning correction, goes in the direction of the Beam-Based measurements concerning the b_6 integrating values of the MQXA type quadrupoles. It shows that it is important to take into consideration all the possible sources of the high order harmonics in order to reproduce Beam-Based values with the model of the machine. It claims for very accurate magnetic measurements of the Inner Triplet quadrupoles.

Concerning the Amplitude Beta-Beating, the prediction for HL-LHC is of the order of few percents when the action increase up to $0.01\,\mu$m, depending on the Beam Position Monitors localization in the machine. The impact of the Fringe Field on the Amplitude Beta-Beating is of the same order of magnitude.

By analysing LHC machine development data, it appears that the main obstacle to observe this phenomena is the noise. If the amplitude beta-beating could be observed for some Beam Position Monitors, those behaviour was not observed in the nearby ones.

To be able to observe it over the noise level, three octupole configurations using the LHC correctors are proposed, without first order amplitude detuning. Through the tracking simulations, the amplitude beta-beating agree quite well with the theory, the discrepancies being explained by the fact that the 2^{nd} order of the RDTs was not taken into consideration for the predictions. Changing the octupoles strengths could make the amplitude beta-beating more or less localized along the accelerator and drastically deteriorate the dynamic aperture.

Precise description of the non-linear beam dynamics of the large hadronic machine, such as LHC and its upgrades requires accurate magnetic fields measurement of the key element of the accelerator and their realistic magnetic fields modeling in the optics model of the machine. Similarly, the impact of the longitudinal distribution of the field on feed-down effect due to crossing angle or magnet displacements, should also be studied in the future.

Appendix A

Python functions to compute the Hamiltonian coefficients

In this appendix are presented two python functions which calculate the Hamiltoninan contribution to the RDTs. In order to operate, the python script need to import the sympy library for the symbolic real, complex and functions, and numpy for the general functions. The particle parameters are defined as follows:

```
from sympy import *
import numpy as np
# Particle position and momentum inside the magnet
#------------------------------------------------------------------------------
x, y, px, py                        = symbols('x y px py', real=True)
zeta_xm, zeta_xp, zeta_ym, zeta_yp = symbols('zeta_xm zeta_xp zeta_ym zeta_yp', complex=True)


# Twiss parameter
#------------------------------------------------------------------------------
betx, bety, alpx, alpy,Dphix,Dphiy = symbols('betx bety alpx alpy Dphix Dphiy', real=True)
```

Given the perturbative Hamiltonian of Eq. (3.4) with the vector potential defined in Eq. (2.18,2.19,2.20), and using the parameters previously defined, the two following functions prints the $h^{(b)}_{jklm}$ of Eq. (3.62), for respectively the normal and skew component of the vector potential.

```
def Print_hjklm_Normal(V,N)
    # V  : Perturbative part of the Hamiltonian
    # N  : Order of the multipole hjklm that will be printed (N=j+k+l+m)
```

```
int_N = N/2
Vn=expand(V.subs({
        x:  sqrt(betx)*(zeta_xm + zeta_xp)/2 ,
        y:  sqrt(bety)*(zeta_ym + zeta_yp)/2 ,
        px: ( I*(zeta_xm - zeta_xp) - alpx*(zeta_xm + zeta_xp) )/(2*sqrt(betx)) ,
        py: ( I*(zeta_ym - zeta_yp) - alpy*(zeta_ym + zeta_yp) )/(2*sqrt(bety))
    }).doit())
for exp_x in (int_N-np.linspace(0,int(np.floor(N/2)),int(np.floor(N/2))+1)):
    exp_y=N/2-exp_x
    for k in range(int(2*exp_x)+1):
        j=int(2*exp_x)-k
        Vn_tp1=Vn
        for i in range(j):
            Vn_tp1=Derivative(Vn_tp1,zeta_xm).doit()
        for i in range(k):
            Vn_tp1=Derivative(Vn_tp1,zeta_xp).doit()
        for m in range(int(2*exp_y)+1):
            l=int(2*exp_y)-m
            Vn_tp=Vn_tp1
            for i in range(l):
                Vn_tp=Derivative(Vn_tp,zeta_ym).doit()
            for i in range(m):
                Vn_tp=Derivative(Vn_tp,zeta_yp).doit()
            Vn_tp =Vn_tp.subs({zeta_xm:0,zeta_xp:0,zeta_ym:0,zeta_yp:0})
            div=factorial(j)*factorial(k)*factorial(l)*factorial(m)
            h_jklm=simplify(expand(
                    (Vn_tp*exp(I*(j-k)*Dphix + I*(l-m)*Dphiy))/div
            ).doit()).doit()
            print(f"h{j},{k},{l},{m} ="); pprint(h_jklm)
```

```
def Print_hjklm_Skew(V,N):
    # V  : Perturbative part of the Hamiltonian
    # N  : Order of the multipole hjklm that will be printed (N=j+k+l+m)
    int_N = N/2
    Vn=expand(V.subs({
            x:  sqrt(betx)*(zeta_xm + zeta_xp)/2 ,
            y:  sqrt(bety)*(zeta_ym + zeta_yp)/2 ,
            px: ( I*(zeta_xm - zeta_xp) - alpx*(zeta_xm + zeta_xp) )/(2*sqrt(betx)) ,
            py: ( I*(zeta_ym - zeta_yp) - alpy*(zeta_ym + zeta_yp) )/(2*sqrt(bety))
            }
        ).doit())
    for exp_x in (int_N-.5-np.linspace(0,int(np.floor(N/2)),int(np.floor(N/2))+1)):
        exp_y=N/2-exp_x
        for k in range(int(2*exp_x)+1):
            j=int(2*exp_x)-k
            Vn_tp1=Vn
            for i in range(j):
                Vn_tp1=Derivative(Vn_tp1,zeta_xm).doit()
            for i in range(k):
                Vn_tp1=Derivative(Vn_tp1,zeta_xp).doit()
            for m in range(int(2*exp_y)+1):
                l=int(2*exp_y)-m
                Vn_tp=Vn_tp1
                for i in range(l):
                    Vn_tp=Derivative(Vn_tp,zeta_ym).doit()
                for i in range(m):
                    Vn_tp=Derivative(Vn_tp,zeta_yp).doit()
                Vn_tp =Vn_tp.subs({zeta_xm:0,zeta_xp:0,zeta_ym:0,zeta_yp:0})
                div=factorial(j)*factorial(k)*factorial(l)*factorial(m)
                h_jklm=simplify(
                    expand(
                        (Vn_tp*exp(I*(j-k)*Dphix + I*(l-m)*Dphiy))/div
                    ).doit()
                ).doit()
```

```
print(f"h{j},{k},{l},{m} ="); pprint(h_jklm)
```

Appendix B

Expression of the Amplitude beta-beating for b_2, b_4 and b_6 errors

Using only the first order of the RDTs for b_2, b_4 and b_6, the expression of the spectral lines at the frequency $-Q_u$ is:

$$2H^{(b)}_{\tilde{x}}(-1,0) = \sqrt{2I_x}e^{i\psi^{(b)}_{x,0}}\left[1+4i\bar{f}^{(b)}_{2000}+6i\bar{f}^{(b)}_{3100}2I_x+4i\bar{f}^{(b)}_{2011}2I_y+8i\bar{f}^{(b)}_{4200}2I_x^2+6i\bar{f}^{(b)}_{3111}2I_x2I_y+4i\bar{f}^{(b)}_{2022}2I_y^2\right] \quad \text{(B.1)}$$

$$2V^{(b)}_{\tilde{y}}(0,-1) = \sqrt{2I_y}e^{i\psi^{(b)}_{y,0}}\left[1+4i\bar{f}^{(b)}_{0020}+6i\bar{f}^{(b)}_{0031}2I_y+4i\bar{f}^{(b)}_{1120}2J_x+8i\bar{f}^{(b)}_{0042}2I_y^2+6i\bar{f}^{(b)}_{1131}2I_x2I_y+4i\bar{f}^{(b)}_{2220}2I_x^2\right] \quad \text{(B.2)}$$

This implies the following expressions for the beta-beating:

$$\begin{aligned}
\Xi^{(b)}_{\tilde{x}}(2I_x,2I_y) = \; & 1+8|f^{(b)}_{2000}|\sin(q^{(b)}_{2000})+16|f^{(b)}_{2000}|^2 \\
& +2I_x\left[12|f^{(b)}_{3100}|\sin(q^{(b)}_{3100})+48|f^{(b)}_{2000}f^{(b)}_{3100}|\cos(q^{(b)}_{2000}-q^{(b)}_{3100})\right] \\
& +2I_y\left[8|f^{(b)}_{2011}|\sin(q^{(b)}_{2011})+48|f^{(b)}_{2000}f^{(b)}_{2011}|\cos(q^{(b)}_{2000}-q^{(b)}_{2011})\right] \\
& +2I_x^2\left[16|f^{(b)}_{4200}|\sin(q^{(b)}_{4200})+64|f^{(b)}_{2000}f^{(b)}_{4200}|\cos(q^{(b)}_{2000}-q^{(b)}_{4200})+36|f^{(b)}_{3100}|^2\right] \\
& +2I_x2I_y\left[12|f^{(b)}_{3111}|\sin(q^{(b)}_{3111})+48|f^{(b)}_{2000}f^{(b)}_{3111}|\cos(q^{(b)}_{2000}-q^{(b)}_{3111})+48|f^{(b)}_{3100}f^{(b)}_{2011}|\cos(q^{(b)}_{3100}-q^{(b)}_{2011})\right] \\
& +2I_y^2\left[8|f^{(b)}_{2022}|\sin(q^{(b)}_{2022})+32|f^{(b)}_{2000}f^{(b)}_{2022}|\cos(q^{(b)}_{2000}-q^{(b)}_{2022})+16|f^{(b)}_{2011}|^2\right] \\
& +O((2I_x+2I_y)^3)
\end{aligned} \quad \text{(B.3)}$$

$$
\begin{aligned}
\Xi_{\tilde{y}}^{(b)}(2I_x, 2I_y) \quad = \quad & 1 + 8|f_{0020}^{(b)}|\sin(q_{0020}^{(b)}) + 16|f_{0020}^{(b)}|^2 \\
& +2I_y\left[12|f_{0031}^{(b)}|\sin(q_{0031}^{(b)}) + 48|f_{0020}^{(b)}f_{0031}^{(b)}|\cos(q_{0020}^{(b)} - q_{0031}^{(b)})\right] \\
& +2I_x\left[8|f_{1120}^{(b)}|\sin(q_{1120}^{(b)}) + 48|f_{0020}^{(b)}f_{2011}^{(b)}|\cos(q_{0020}^{(b)} - q_{1120}^{(b)})\right] \\
& +2I_y^2\left[16|f_{0042}^{(b)}|\sin(q_{0042}^{(b)}) + 64|f_{0020}^{(b)}f_{4200}^{(b)}|\cos(q_{0020}^{(b)} - q_{0042}^{(b)}) + 36|f_{0031}^{(b)}|^2\right] \\
& +2I_x2I_y\left[12|f_{1131}^{(b)}|\sin(q_{1131}^{(b)}) + 48|f_{0020}^{(b)}f_{1131}^{(b)}|\cos(q_{0020}^{(b)} - q_{1131}^{(b)}) + 48|f_{0031}^{(b)}f_{1120}^{(b)}|\cos(q_{0031}^{(b)} - q_{1120}^{(b)})\right] \\
& +2I_x^2\left[8|f_{2220}^{(b)}|\sin(q_{2220}^{(b)}) + 32|f_{0020}^{(b)}f_{2022}^{(b)}|\cos(q_{0020}^{(b)} - q_{2220}^{(b)}) + 16|f_{1120}^{(b)}|^2\right] \\
& +O((2I_x + 2I_y)^3)
\end{aligned}
\tag{B.4}
$$

But, in Appendix C of [71], it is reported that:

$$
2H_{\tilde{x}}^{(b)}(1,0) \quad = \quad \sqrt{2I_x}e^{i\psi_{x,0}^{(b)}}\left[\cosh(4|f_{2000}^{(b)}|) - i\sinh(4|f_{2000}^{(b)}|)\right] \tag{B.5}
$$

$$
2V_{\tilde{y}}^{(b)}(0,1) \quad = \quad \sqrt{2I_y}e^{i\psi_{y,0}^{(b)}}\left[\cosh(4|f_{0020}^{(b)}|) - i\sinh(4|f_{0020}^{(b)}|)\right] \tag{B.6}
$$

and:

$$
\left|2H_{\tilde{x}}^{(b)}(1,0)\right|^2/2I_x = 1 - 2\sinh(4|f_{2000}^{(b)}|)\sin(q_{2000}^{(b)}) + \sinh^2(4|f_{2000}^{(b)}|) \tag{B.7}
$$

$$
\approx 1 + 8|f_{2000}^{(b)}|\sin(q_{2000}^{(b)}) + 32|f_{2000}^{(b)}|^2 + O(|f_{2000}^{(b)}|^4) \tag{B.8}
$$

$$
\left|2V_{\tilde{y}}^{(b)}(0,1)\right|^2/2I_y = 1 - 2\sinh(4|f_{0020}^{(b)}|)\sin(q_{0020}^{(b)}) + \sinh^2(4|f_{0020}^{(b)}|) \tag{B.9}
$$

$$
\approx 1 + 8|f_{0020}^{(b)}|\sin(q_{0020}^{(b)}) + 32|f_{0020}^{(b)}|^2 + O(|f_{0020}^{(b)}|^4) \tag{B.10}
$$

The difference for the coefficient in front of $|f_{0020}^{(b)}|^2$ between (B.3-B.4) and (B.8-B.10) comes from the appendix of Ref. [77]. In this paper, it is shown that an emittance sharing can be observed between the horizontal and vertical plane because of $f_{1001}^{(b)}$ and $f_{1010}^{(b)}$, using the normal form transformation $F = \sum_{jklm} f_{jklm}^{(b)}\zeta_{x,+}^j\zeta_{x,-}^k\zeta_{y,+}^l\zeta_{y,-}^m$ and the Lie expansion of $h_x = e^{:F:}\zeta_{x,-} = \sum_r^\infty (D_F^r\zeta_{x,-}/r!)$ with the Poisson bracket $D_F\zeta_{x,-} = [F, \zeta_{x,-}]$. The same process applied to $f_{2000}^{(b)}$ and $f_{0020}^{(b)}$ gives above results. The difference between (B.3-B.4) is specific to quadrupole error. To illustrate this, let's consider F as a polynomial of order $Or(F) = n$ and a transformation g. This gives:

$$
\begin{aligned}
Or(D_F g) &= Or(F) + Or(g) - 2 && = n - 2 + Or(g) \\
Or(D_F^2 g) &= Or(F) + Or(D_f g) - 2 && = 2n - 4 + Or(g) \\
&\vdots && \vdots \\
Or(D_F^m g) &= Or(F) + Or(D_f^{m-1} g) - 2 && = m(n-2) + Or(g)
\end{aligned}
\tag{B.11}
$$

For quadrupole, $n = 2$ which means that $Or(D_F^m g) = Or(g)$ and the higher order of the quadrupole RDTs will

only add on the same term $jklm$. But this is not the case for higher order multipole. As example, for sextupoles, the polynomial order can only increase ($Or(D_F^m g) = m + Or(g)$) and all Spectral Lines are excited; for octupoles, it's RDTs equivalent to even harmonics; and so on.

So let's define the final RDT coefficient $g^{(b)}_{jklm}$ which is the sum of all order RDT terms acting on the same spectral line with the same exponent of $2I_x$ and $2I_y$. We define the angle of $g^{(b)}_{jklm}$ as $q^{(2,b)}_{jklm}$ and for normal quadrupole error, $g_{2000} = -(\sinh(4|f^{(b)}_{2000}|) - i(\cosh(4|f^{(b)}_{2000}|) - 1))/4$. This gives:

$$2H^{(b)}_{\tilde{x}}(-1,0) = \sqrt{2I_x}e^{i\psi^{(b)}_{x,0}}\left[1 + 4i\bar{g}^{(b)}_{2000} + 6i\bar{g}^{(b)}_{3100}2I_x + 4i\bar{g}^{(b)}_{2011}2I_y + 8i\bar{g}^{(b)}_{4200}2I_x^2 + 6i\bar{g}^{(b)}_{3111}2I_x2I_y + 4i\bar{g}^{(b)}_{2022}2I_y^2\right] \quad \text{(B.12)}$$

$$2V^{(b)}_{\tilde{y}}(0,-1) = \sqrt{2I_y}e^{i\psi^{(b)}_{y,0}}\left[1 + 4i\bar{g}^{(b)}_{0020} + 6i\bar{g}^{(b)}_{0031}2I_y + 4i\bar{g}^{(b)}_{1120}2J_x + 8i\bar{g}^{(b)}_{0042}2I_y^2 + 6i\bar{g}^{(b)}_{1131}2I_x2I_y + 4i\bar{g}^{(b)}_{2220}2I_x^2\right] \quad \text{(B.13)}$$

and

$$\begin{aligned}
\Xi^{(b)}_{\tilde{x}}(2I_x, 2I_y) = {} & 1 + 8|g^{(b)}_{2000}|\sin(q^{(2,b)}_{2000}) + 16|g^{(b)}_{2000}|^2 \\
& + 2I_x\left[12|g^{(b)}_{3100}|\sin(q^{(2,b)}_{3100}) + 48|g^{(b)}_{2000}g^{(b)}_{3100}|\cos(q^{(2,b)}_{2000} - q^{(2,b)}_{3100})\right] \\
& + 2I_y\left[8|g^{(b)}_{2011}|\sin(q^{(2,b)}_{2011}) + 48|g^{(b)}_{2000}g^{(b)}_{2011}|\cos(q^{(2,b)}_{2000} - q^{(2,b)}_{2011})\right] \\
& + 2I_x^2\left[16|g^{(b)}_{4200}|\sin(q^{(2,b)}_{4200}) + 64|g^{(b)}_{2000}g^{(b)}_{4200}|\cos(q^{(2,b)}_{2000} - q^{(2,b)}_{4200}) + 36|g^{(b)}_{3100}|^2\right] \\
& + 2I_x2I_y\left[12|g^{(b)}_{3111}|\sin(q^{(2,b)}_{3111}) + 48|g^{(b)}_{2000}g^{(b)}_{3111}|\cos(q^{(2,b)}_{2000} - q^{(2,b)}_{3111}) + 48|g^{(b)}_{3100}g^{(b)}_{2011}|\cos(q^{(2,b)}_{3100} - q^{(2,b)}_{2011})\right] \\
& + 2I_y^2\left[8|g^{(b)}_{2022}|\sin(q^{(2,b)}_{2022}) + 32|g^{(b)}_{2000}f^{(b)}_{2022}|\cos(q^{(2,b)}_{2000} - q^{(2,b)}_{2022}) + 16|g^{(b)}_{2011}|^2\right] \\
& + O((2I_x + 2I_y)^3)
\end{aligned} \quad \text{(B.14)}$$

$$\begin{aligned}
\Xi^{(b)}_{\tilde{y}}(2I_x, 2I_y) = {} & 1 + 8|g^{(b)}_{0020}|\sin(q^{(2,b)}_{0020}) + 16|g^{(b)}_{0020}|^2 \\
& + 2I_y\left[12|g^{(b)}_{0031}|\sin(q^{(2,b)}_{0031}) + 48|g^{(b)}_{0020}g^{(b)}_{0031}|\cos(q^{(2,b)}_{0020} - q^{(2,b)}_{0031})\right] \\
& + 2I_x\left[8|g^{(b)}_{1120}|\sin(q^{(2,b)}_{1120}) + 48|g^{(b)}_{0020}g^{(b)}_{2011}|\cos(q^{(2,b)}_{0020} - q^{(2,b)}_{1120})\right] \\
& + 2I_y^2\left[16|g^{(b)}_{0042}|\sin(q^{(2,b)}_{0042}) + 64|g^{(b)}_{0020}g^{(b)}_{4200}|\cos(q^{(2,b)}_{0020} - q^{(2,b)}_{0042}) + 36|g^{(b)}_{0031}|^2\right] \\
& + 2I_x2I_y\left[12|g^{(b)}_{1131}|\sin(q^{(2,b)}_{1131}) + 48|g^{(b)}_{0020}g^{(b)}_{1131}|\cos(q^{(2,b)}_{0020} - q^{(2,b)}_{1131}) + 48|g^{(b)}_{0031}g^{(b)}_{1120}|\cos(q^{(2,b)}_{0031} - q^{(2,b)}_{1120})\right] \\
& + 2I_x^2\left[8|g^{(b)}_{2220}|\sin(q^{(2,b)}_{2220}) + 32|g^{(b)}_{0020}g^{(b)}_{2022}|\cos(q^{(2,b)}_{0020} - q^{(2,b)}_{2220}) + 16|g^{(b)}_{1120}|^2\right] \\
& + O((2I_x + 2I_y)^3)
\end{aligned} \quad \text{(B.15)}$$

Appendix C

Résumé de la thèse en Français

La qualité du faisceau, et sa stabilité à long terme, est un sujet particulièrement étudié dans les accélérateurs circulaires hadroniques. Chaque nouvel accélérateur est conçu pour fournir une luminosité (nombre de collisions par seconde et par unité de surface) toujours plus importante à plus haute énergie. Cela implique entre autres, des collisionneurs de plus en plus grands ainsi que des contraintes magnétiques et mécaniques de plus en plus fortes sur les éléments les composant. Le Large Hadron Collider (LHC) au CERN en est un parfait exemple avec ses $27\,\mathrm{km}$ de circonférence et un faisceau de protons pouvant atteindre une énergie de collision de $14\,\mathrm{TeV}$ dans le centre de masse. Pour y parvenir, l'accélérateur dépend d'avancées technologiques toujours plus avancées comme celle des aimants supraconducteurs. Le champ magnétique de ces aimants présente des composantes non linéaires, pouvant réduire la stabilité à long terme du faisceau dans la machine. Cela impacterait grandement la luminosité et donc le nombre d'évènements par seconde au niveau des expériences ainsi que la durée de vie des composants de l'accélérateur. Il est donc nécessaire de connaître le mieux possible la position et l'amplitude de ces non-linéarités dans la machine afin de simuler de la façon la plus réaliste possible le transport du faisceau et de corriger efficacement ces non-linéarités.

L'objectif de cette thèse est de modéliser et de quantifier les effets 3D du champ magnétique sur des observables mesurables avec le faisceau. J'ai proposé une modélisation analytique et numérique des effets 3D de champ. J'ai ensuite appliqué mon nouveau modèle de simulation au projet HL-LHC pour prédire l'impact des non linéarités dans les cartes de champ calculées. En parallèle, une étude expérimentale a été menée sur le LHC afin de vérifier si le champ de fuite des aimants pouvait expliquer les écarts observés entre les simulations et les mesures.

Le premier chapitre présente les deux accélérateurs étudiés au cours de cette thèse: le LHC et HL-LHC. Après un rapide rappel de leurs accomplissements et de leurs objectifs respectifs, ainsi que de comment calculer la luminosité maximale aux Points d'Interaction (IP), nous détaillons leurs Régions d'Interaction (IR), où se situent les expériences de ATLAS et CMS. Dans ces régions se trouve de par et d'autre de l'IP une suite de trois

quadripôles de grande ouverture physique, appelée Triplet de Focalisation Final (IT). Des correcteurs sont accolés à ces quadripôles. La publication [5], démontre que pour le LHC, la principale source de non-linéarité à l'énergie de collision provient des quadripôles de l'IT aux niveaux d'ATLAS et de CMS. Cela s'explique par le fait que i) un faisceau de taille minimale au niveau de l'IP, implique une très grande taille de faisceau dans ces quadripôles et ii) les aimants du LHC et de HL-LHC sont supraconducteurs. Les harmoniques composant leur champ magnétique peuvent varier grandement entre leur partie centrale et leurs extrémités. Tous ces points suggèrent que de petits écarts entre le modèle et les mesures avec le faisceau dans ces régions peuvent avoir un impact significatif sur la dynamique du faisceau.

Dans le second chapitre, nous revenons sur la définition des harmoniques du champ magnétique et du champ de fuite. Les harmoniques b_n et a_n correspondent respectivement à des oscillations normales et tournées du champ magnétique lorsqu'il est mesuré sur un cercle dans le plan transverse et centré sur l'axe de l'aimant. On appelle harmonique principale, celle qui correspond au nombre de pôles de l'aimant divisé par 2 ($n = 2$ pour les quadripôles par exemple). Des défauts géométriques peuvent ajouter d'autres harmoniques, considérées comme des termes d'erreurs magnétiques non-linéaires. Les mesures étant généralement réalisées avec une bobine tournante, la force de ces harmoniques est moyennée sur la totalité de l'aimant. Ce faisant, elles sont considérées comme constantes tout au long de l'aimant pour devenir nulles soudainement aux extrémités. Cette approximation est appelée Hard-Edge (ou champ franc). Dans le cas du LHC, des mesures précises à $0.2\,\text{units}$[1] ont été réalisées sur ces quadripôles et sont stockées dans la base de données WISE; base de données recueillant toutes les inductions magnétiques mesurées de tous les éléments du LHC. Pour HL-LHC qui était encore en phase de conception lors de cette thèse, les aimants n'ont pas encore été construits. Dans ce cas, à la partie systématique des harmoniques s'ajoutent deux termes aléatoires comme montré dans Eq. (2.4). Cela permet de modéliser les incertitudes de construction des aimants et les différentes configurations d'erreur dans la machine.

Bien entendu, le modèle hard-edge ne représente pas parfaitement la réalité comme H. WIEDEMANN le rappelle dans Particle Accelerator Physics. Le passage de 0 à la valeur nominale du champ magnétique de l'aimant n'est pas soudain et nous appelons Champs de Fuite (i.e. "Fringe Field" en anglais) cette région de transition. Lorsque l'on regarde le champ magnétique sous la forme d'harmoniques comme dans Fig. 2.1, on peut observer une transition douce pour l'harmonique principale mais cette transition est plus perturbée pour les autres harmoniques. On peut aussi remarquer que la présence à une extrémité des connecteurs servant à alimenter en courant les bobines supra-conductrices, brise la symétrie longitudinale des harmoniques. Ainsi, lorsque nous parlons de champ de fuite, nous désignons le champ magnétique 3D complet que nous pouvons résumer en 2 points:

- la dérivée longitudinale des harmoniques $\partial b_n/\partial z$ (i.e. la reconstruction du champ magnétique longitudinal);

[1] 1 unit correspond à une variation relative sur le champ de 10^{-4} à un rayon de référence donné; 17 cm dans le cas du LHC

- la distribution longitudinale des harmoniques $b_n(z)$.

Différentes études sur la modélisation du champ de fuite ont porté sur l'impact de la composante longitudinale B_z du champ magnétique. Ainsi, ces études prennent seulement en compte la moitié de la définition du champ de fuite. Tout comme avec les mesures, la variation longitudinale des harmoniques est cachée, négligée.

Afin de représenter de la manière la plus réaliste le champ magnétique 3D, nous utilisons les Gradients Généralisés présentés dans [3] et qui sont liés au Potentiel Vecteur 3D. Ce Potentiel Vecteur est utilisé dans cette thèse pour les simulations de dynamique faisceau. L'expression pour calculer les Gradients Généralisés est donnée par Eq. (2.15) et le passage de ceux-ci au Potentiel Vecteur 3D est donné par Eq. (2.18), (2.19) et (2.20).

Grâce à ce potentiel vecteur 3D, des expressions analytiques peuvent être développées pour différents observables de la dynamique faisceau, comme décrit dans le troisième chapitre. La première section de ce chapitre est consacrée à l'expression de l'Hamiltonien décrivant le mouvement des particules chargées dans un champ magnétique de type multipolaire. En utilisant une première approximation dite paraxiale (i.e. le moment total de la particules est considéré comme bien supérieur aux moments transverses), un nouvel Hamiltonien est décrit. Cet Hamiltonien est ensuite décomposé en 2 termes $\mathcal{H}_0$ et $\mathcal{H}_p$. Le premier terme correspond à la dynamique des particules en présence de dipôles et de quadripôles. Les travaux de Courant et Snyder [40] ont montré que le mouvement des particules décrit une ellipse tour après tour dans l'espace des phases (i.e. section de Pointcaré). Les trois paramètres suivants, introduits par leur travaux et caractérisant cet ellipse, sont utilisés et étudiés dans cette thèse ($u \in \{x, y\}$):

- l'action $2J_u$ est un invariant. Il correspond à l'aire de cette ellipse.
- la fonction bétatronique $\beta_u(s)$ est un des paramètres de Twiss qui caractérisent la forme de l'ellipse. Sa racine carrée est proportionnelle à l'enveloppe du faisceau de particules le long de l'accélérateur.
- le nombre d'onde Q_u ou "tune" en anglais. Il correspond au nombre d'oscillations réalisées dans l'espace des phases par la particule après une révolution dans l'accélérateur.

La section 3.2 étudie plus en détails le second terme de l'Hamiltonien $\mathcal{H}_p$. Celui-ci décrit la perturbation du mouvement générée par des erreurs non-linéaires du champ magnétique et des écarts par rapport à $\mathcal{H}_0$. Par la suite, différents sous-termes sont identifiés dans le terme $\mathcal{H}_p$. Nous ne citons que les 4 sous-termes suivants:

- $\mathcal{V}_{HE}$ contient les harmoniques du champ magnétique. La principale différence par rapport aux travaux antérieurs étant que nous considérons la répartition longitudinale de celles-ci le long des aimants.
- $\mathcal{V}_{FF;pa}$ et $\mathcal{V}_{FF;a^2}$ contiennent les effets des dérivées impaires des harmoniques. Elles agissent dans l'Hamiltonien comme des multipôles équivalents[1] respectivement d'ordre $(n+2l+2)$ et $2\times(n+2l+1)$. Ce phénomène est

[1] On note l'ordre de l'harmonique n et leurs dérivées respectivement paire $(2l)$ et impaire $(2l+1)$.

appelé ”feed up”.

- $\mathcal{V}_{FF;a_z}$ contient les effets des dérivées paires. Elles agissent dans l' Hamiltonien comme des multipôles équivalents d'ordre $(n + 2l)$.

Ces sous-termes vont exciter des résonances de l'espace des phases. Ils s'ajoutent aux mêmes résonances excitées par les harmoniques considérées constantes sur la longueur de l'aimant, mais de façon différente. On notera par exemple les contributions venant de $\mathcal{V}_{FF;pa}$ qui sont majoritairement des nombres complexes. Les contributions aux résonances de types octupolaire et dodécapolaire sont montrées respectivement dans les Tables 3.1 et 3.2. Celles-ci ont été obtenues grâce à un code Python présenté dans l'annexe A. Ce code en symbolique donne les différents coefficients h_{jklm} à partir des termes perturbatifs de l'Hamiltonien. Ces coefficients sont par la suite utilisés pour calculer l'excitation des résonances.

Pour les calculer, il est nécessaire de résoudre les équations du mouvement Hamiltonien dans le cas non-linéaire. Pour cela, nous utilisons les propriétés de l'algèbre et de l'opérateur de Lie, comme démontré dans la section 3.3. En identifiant l'opérateur de Lie dans les équations du mouvement de la mécanique Hamiltonienne, ces dernières sont solvables sur un intervalle où l'Hamiltonien est invariant. La solution est appelée Transformation de Lie, ou ”Lie map” en Anglais. L'avantage de cette approche est que cette Transformation est symplectique à tout ordre par construction, i.e. les aires sont préservées par la transformation. Cette condition est nécessaire pour les accélérateurs que nous étudions et les codes numériques que nous utilisons.

Grâce à cette transformation, nous pouvons calculer l'expression des résonances induites par la partie perturbative de l'Hamiltonien, i.e. ”Resonance Driving Terms” (RDT). La section 3.4 présente un rapide résumé des travaux réalisés [44, 45, 46, 47] sur ce sujet. Nous rappelons les conditions sous lesquelles les coefficients h_{jklm} excitent des résonances, génèrent une variation des nombres d'onde ou génèrent un mouvement chaotique. Les Formes Normales [46, 47] introduites par la suite, permettent d'exprimer la perturbation de la trajectoire d'une particules dans l'espace des phases tour après tour de l'accélérateur. La trajectoire initialement sous la forme d'une ellipse dans le cas linéaire, est déformée par la présence de ces résonances. Lorsque l'on applique la Transformation de Fourier aux positions tour après tour dans l'espace des phases, différentes lignes spectrales apparaissent dans le spectre, celles-ci étant liées aux résonances. Comme les fréquences des lignes spectrales correspondent à une composition des nombre d'onde $(n_x Q_x + n_y Q_y)$, les lignes spectrales sont notées $H(n_x, n_y)$ et $V(n_x, n_y)$, respectivement pour les plans horizontal et vertical. Nous donnons l'expression des lignes spectrales $H(-1, 0)$ et $V(0, -1)$, utilisées dans la section 3.6, car elles expriment une déformation de type elliptique dans l'espace des phases.

La variation du nombre d'onde et de la mesure de la fonction bétatronique avec l'action peuvent maintenant être exprimées. Il s'agit des sujets respectifs des 2 sections suivantes. Dans la section 3.5, l'expression de la variation du nombre d'ondes avec l'action obtenue à partir de notre expression du vecteur potentiel est comparée à celle issue de la littérature, que nous assimilons au cas Hard-Edge. Dans la section 3.6, la variation de la mesure de la fonction

bétatronique avec l'action est développée, pour la première fois. Il y a deux méthodes pour la mesurer à partir de la ligne spectrale principale: soit en utilisant l'avance de phase entre 3 BPMs (Beam Position Monitors), soit en utilisant l'amplitude à 1 BPM. Nous nous focalisons sur la seconde méthode. En faisant apparaître la dépendance avec l'action dans l'expression de l'amplitude des lignes spectrales $H(-1,0)$ et $V(0,-1)$, nous obtenons un nouvel observable pour la déviation bétatronique. La dernière section discute des incertitudes sur la mesure de l'action et du nouvel observable.

Les expressions théoriques de deux des observables étant détaillées, le chapitre 4 discute la précision de calcul des trajectoires des particules dans les multipôles magnétiques. Comme nous étudions l'ouverture dynamique dans un accélérateur hadronique circulaire, nos schémas numériques doivent correspondre à certains critères de temps de calcul et de symplecticité.

Dans un premier temps, nous revenons sur la façon dont les trajectoires de particules sont normalement calculées. Le Hard-Edge (HE) est présenté, correspondant à un schéma de type saute-mouton (i.e. une séquence de matrices "kick" et "drift"). Dans notre cas, l'élément magnétique est divisé en 16 sous-éléments plus courts pour un bon compromis entre la précision et la vitesse de calcul.

Dans la seconde section, une première approche est proposée pour prendre en compte la distribution longitudinale des harmoniques le long de l'aimant. Elle consiste à ajouter des "kicks" additionnels aux extrémités du modèle HE. Il est néanmoins important que les forces multipolaires totales des éléments soient conservées. Pour cela, nous divisons les aimants en 3 sections: l'extrémité avec les connecteurs (CS ou LE), la partie centrale avec un champ magnétique constant (BD) et l'extrémité sans les connecteurs (NC ou RE). Les équations (4.6) et (4.7) doivent être satisfaites. Nous notons ce modèle HE+Heads.

Pour finir, la dernière section introduit le schéma numérique que nous avons développé au CEA de Saclay. Il s'agit de l'aboutissement de 3 stages et 2 thèses réalisés sous la direction de B. Dalena, J. Payet et O. Napoly du CEA et en collaboration avec L. Bonaventura de Polytechnico di Milano, Italie. Les objectifs étaient de calculer le potentiel vecteur avec la plus grande précision possible, à partir d'une carte magnétique (simulée ou mesurée) fournie par les concepteurs des aimants, puis de traduire ce potentiel vecteur en carte de transport pour nos simulations de dynamique de faisceau. Ce schéma numérique, présenté dans la première partie de cette section, a été implémenté dans le code de calcul de trajectoire de particules SixTrack, développé au CERN [52]. La procédure pour l'implémenter dans SixTrack, est rapidement détaillée dans la seconde partie de cette section. Nous notons ce modèle Lie2 et précisons le nombre de dérivées du Gradient Généralisé en indiquant: ND0 lorsqu'il n'y en a aucune, et ND6 lorsque nous nous arrêtons au sixième ordre.

Ces 3 modèles correspondent à différentes représentations du champ magnétique comme illustré dans la figure 4.2. Des simulations avec le code SixTrack sont réalisées et leurs effets sur différents observables sont comparés dans les 3 derniers chapitres. Les observables de la dynamique faisceau sont respectivement dans ces

chapitres: i) la variation du nombre d'onde avec l'amplitude (i.e. l'"amplitude detuning"), ii) la variation de la mesure de la fonction bétatronique avec l'amplitude (i.e. l'"amplitude beta-beating") et iii) l'ouverture dynamique.

Le chapitre 5 étudie l'impact des 3 modèles, présentés dans le chapitre 4, sur la variation du nombre d'onde avec l'action, i.e. "amplitude detuning". Cette observable est la mesure la plus directe et la plus stable des effets des non-linéarités du champ magnétique sur la dynamique faisceau. Il est couramment utilisé lors des périodes de réglage du LHC, pour corriger les erreurs multipolaires présentes dans les aimants de la machine.

Dans un premier temps pour HL-LHC, des écarts mesurables sont observés entre les 3 modèles dans les simulations du "amplitude detuning", que ce soit pour la distribution longitudinale des harmoniques ou les dérivées du gradient. Dans le second cas, aucun impact mesurable n'est observé pour des dérivées d'ordre supérieur à 2. Concernant l'impact sur la correction de l'amplitude detuning, ,nous observons aussi un décalage lorsque l'on exprime la force d'un correcteur d'un côté de l'IP en fonction de l'autre. Dans le cas des dérivées du gradient, le décalage des forces des correcteurs octupolaire est de $\sim 4\,\%$ par rapport aux spécifications du correcteur alors que dans le cas de la distribution longitudinale des harmoniques, l'effet sur la force des correcteurs dodécapolaires est plus significatif ($\sim 13\,\%$). Dans tous les cas, le modèle HE+Heads est déjà une très bonne approximation du modèle Lie2 si on ignore les dérivées du gradient. Néanmoins, cette machine étant encore en phase de conception, les incertitudes de configuration magnétiques restent prédominantes.

Dans le cas de LHC, il a été reporté un décalage entre les corrections obtenues à partir de mesures avec le faisceau et les prédictions du modèle [5], qui utilise les valeurs des multipôles connus des aimants du LHC et stockées dans la base de données WISE [24]. Nous nous sommes alors posé la question si ce décalage pourrait être expliqué par la distribution longitudinale des harmoniques le long des éléments. D'autre part, la présence d'un écran faisceau a soulevé la question de son influence sur le champ de fuite par rapport au champ de la partie centrale. Pour cela, le code de simulation de champ magnétique Roxie [60] a été utilisé pour recréer le modèle magnétique 3D d'une des deux familles de quadripôle de la région d'interaction du LHC (Q_1 et Q_3). Aucune information sur la structure mécaniques 3D de la seconde famille (Q_2) n'a été retrouvée et le modèle magnétique 3D du Q_1 avec l'écran faisceau n'a pas convergé. Néanmoins, à partir des résultats du Q_3 nous avons pu observer que:

- l'écran faisceau ajoute bien une erreur octupolaire de l'ordre de $\pm 0.12\,\text{units}$ suivant son orientation (pris en compte dans WISE) mais aussi une erreur de type dodécapolaire de l'ordre de $0.08\,\text{units}$ (non pris en compte dans WISE);
- l'effet de l'écran faisceau n'est pas le même dans les extrémités que dans la partie centrale de l'aimant;
- les valeurs totales des erreurs octupolaires et dodécapolaires sont systématiquement plus petits de $0.2\,\text{units}$ dans le modèle 3D par rapport aux mesures.

Après vérification, il est apparu que les simulations du champ magnétique 3D, sans écran faisceau, reproduisent très bien les mesures du profil longitudinal des harmoniques côté connecteur, fournies par H. Nakamoto (KEK). Un écart apparaît néanmoins pour le b_4 sur une courte région. Les implications de ces résultats préliminaires sont assez significatives pour la force des correcteurs. Tout d'abord, les prédictions du modèle 3D tendent à recentrer les valeurs prévues des correcteurs octupolaires sur celles obtenues avec le faisceau. Sachant aussi que le LHC n'a apparemment pas besoin de correction dodécapolaire, les prédictions du modèle 3D tendent à diminuer la force de ces correcteurs par rapport à celles utilisant la base de donnée WISE. L'impact de la distribution longitudinale des harmoniques est très faible pour les correcteurs octupolaires et assez significatif pour les correcteurs dodécapolaires mais tend à augmenter les forces des correcteurs nécessaires dans les deux cas.

Le chapitre 6 porte sur l'étude du nouvel observable: la variation de la déviation bétatronique avec l'action, ou "Amplitude Beta-Beating". La déviation bétatronique ou "Beta-Beating", est définie comme l'écart relatif des mesures du paramètre $\beta_u(s)$ par rapport à celui du modèle $\mathcal{H}_0$. L'"Amplitude Beta-Beating" est donc la dépendance de ce Beta-Beating avec l'action. Comme précisé dans la section 3.6, il y a 2 méthodes pour mesurer la fonction $\beta_u(s)$ à partir des lignes spectrales des positions de particules tour après tour: soit en utilisant les avances de phase entre 3 BPMs, soit en utilisant l'amplitude à 1 BPM. Ce chapitre se focalise sur cette dernière méthode. La section 3.6 explicite l'expression de cet observable pour des résonances de type octupolaire.

A la suite de la présentation des résultats de la variation du nombre d'onde avec l'action au CERN, la question de pouvoir observer une variation du Beta-Beating avec l'action s'est posée. La première section montre les résultats des analyses pour HL-LHC pour différentes variations du nombre d'onde avec l'action. On peut observer des effets linéaires liés aux erreurs octupolaires (Fig. 6.1) et des effets quadratiques liés aux erreurs dodécapolaires avec ou sans prise en compte de la distribution longitudinale des harmoniques (respectivement, Fig. 6.2 et Fig. 6.3). Dans ces dernières figures, on remarque que si l'effet de l'Amplitude Beta-Beating est assez faible (de l'ordre de quelques pourcents lorsque l'action augmente de $0.01\,\mu\mathrm{m}$), l'impact du champ de fuite sur celui-ci est du même ordre de grandeur.

Ces observations faites, la section suivante porte sur les analyses de mesures réalisées dans le LHC en faisant varier l'action, afin de vérifier si ce phénomène est déjà observable. Il apparaît très rapidement que la principale contrainte de cette mesure est le bruit blanc dans les BPMs. On observe en effet, la même décroissance avec l'action que l'on pourrait observer avec une amélioration du rapport signal sur bruit. On peut néanmoins observer d'importantes variations du Beta-Beating avec l'action pour certains BPMs.

Il a donc été décidé de proposer des configurations d'erreurs octupolaires générant l'Amplitude Beta-Beating mais sans Amplitude Detuning. Les configurations proposées sont reportées dans la dernière section avec pour objectif de générer $+500\,\%/\mu\mathrm{m}$ d'Amplitude Beta-Beating horizontale en utilisant des correcteurs octupôlaires du LHC. Leurs forces sont calculées en utilisant la même méthode que pour la correction de l'Amplitude Detuning

mais en imposant cette fois-ci aussi les parties réelle et imaginaire de certains termes de résonances. En effet, comme le montre l'équation (3.87), le terme f_{3100} est le principal contributeur de l'Amplitude Beta-Beating direct dans le plan horizontal. Les termes de résonance dépendant de la position dans la machine, les forces des correcteurs sont obtenues à partir des termes de résonances calculés à la position d'un BPM de référence et des termes d'Amplitude Detuning directs et croisés. Trois configurations sont ainsi proposées pour différents BPMs de référence et différentes contraintes. Dans les 3 cas, le phénomène d'Amplitude Beta-Beating est observé tout au long de l'accélérateur et est en très bon accord avec la théorie. Une déviation est aussi observée pour de très hautes actions. Cette déviation peut s'expliquer par des termes de résonance d'ordre supérieur, ceux-ci n'étant pas pris en compte dans les prédictions analytiques. Pour finir, d'importants écarts apparaissent lorsque l'on calcule la différence entre les deux méthodes permettant de mesurer la déviation bétatronique. Ces écarts sont localisés à proximité des correcteurs utilisés pour générer la variation de la mesure de la déviation bétatronique avec l'action. Si cette méthode permet de localiser les erreurs, elle reste néanmoins fortement impactée par le bruit blanc des BPMs.

Dans le dernier chapitre, les effets des 3 modèles, décrits dans le chapitre 4, sur l'ouverture dynamique sont comparés. Cet observable correspond à la région de stabilité des trajectoires des particules après plusieurs révolutions dans l'anneau. Les particules, dont leur position initiale se trouve dans cette région, peuvent survivre pendant 10^N révolutions de l'accélérateur. Il s'agit donc d'un observable majeur pour le réglage de la machine car il représente la durée de vie du faisceau. Ces études n'ont porté que sur le cas du HL-LHC.

Dans un premier temps, nous avons vérifié l'impact des dérivées du gradient sur l'ouverture dynamique. Il apparaît que les dérivées n'ont qu'un faible impact de base et, au delà de l'ordre 2, aucun effet significatif n'est observé.

Dans la seconde section, l'impact des 3 modèles est étudié sur l'ouverture dynamique (estimée sur 10^4 révolutions) en fonction de l'angle dans le plan (x, y). Que ce soit pour une configuration de la machine ou la statistique sur 60 configurations, des écarts jusqu'à $2\,\sigma$ sont observés entre les modèles hors axe, (i.e. entre 30° et 60°). La correction dodécapolaire ne corrige pas cet écart hors axe. Cela n'explique pas complètement les écarts de l'ordre de $20\,\%$ observés dans le LHC [76].

Dans la dernière section, l'impact de 3 modèles est étudié sur l'évolution de l'ouverture dynamique en fonction du nombre de révolutions. De manière similaire au cas de la section précédente, de gros écarts sont observés sur les 1000 premières révolutions et évoluent peu après 10^4 révolutions. Sur la statistique de 60 configurations de machine, appliquer le schéma de correction réduit la taille des incertitudes. Ces effets sont significatifs car bien supérieurs aux incertitudes numériques rapportées dans la littérature ($0.5\,\sigma$ à 10^5 révolutions).

En résumé, des deux éléments qui caractérisent le champ de fuite, la distribution longitudinale interne des harmoniques est celle qui a le plus fort impact sur les observables étudiés: la variation du nombre d'onde avec

l'action, la variation de la déviation bétatronique avec l'action et l'ouverture dynamique.

Dans le cas d'un accélérateur en phase de conception comme HL-LHC, les incertitudes magnétiques des aimants et de configuration de la machine sont bien supérieures aux effets du champ de fuite. Mais ceux-ci peuvent néanmoins servir de limite inférieure pour la marge lors du choix des spécifications des correcteurs. Dans le cas d'un accélérateur déjà construit comme le LHC, prendre en compte le champ de fuite peut permettre de réduire les écarts entre le modèle et les corrections à partir d'observations sur le faisceau. Néanmoins, pour prendre en compte ces effets, une grande précision des champs magnétiques et des modèles d'ordre supérieur à ceux utilisés actuellement restent nécessaires.

Bibliography

[1] L Schachinger and R Talman. “TEAPOT: A thin element accelerator program for optics and tracking”. In: *Part. Accel.* 22.SSC-52 (Dec. 1985), 35. 46 p. URL: http://cds.cern.ch/record/165372.

[2] H. Burkhardt et al. “Improved TEAPOT method and tracking with Thick quadrupoles for the LHC and its upgrade”. In: *Proc. 4th International Particle Accelerator Conference*. Shanghai, China: JACOW Publishing, Geneva, Switzerland, June 2013. URL: https://accelconf.web.cern.ch/AccelConf/ipac2013/papers/mopwo027.pdf.

[3] Marco Venturini and Alex J. Dragt. “Accurate computation of transfer maps from magnetic field data”. In: *NIMPA* 427.1-2 (May 1999), pp. 387–392. ISSN: 0168-9002. DOI: 10.1016/S0168-9002(98)01518-6.

[4] A. V. Bogomyagkov et al. “ANALYSIS OF THE NON-LINEAR FRINGE EFFECTS OF LARGE APERTURE TRIPLETS FOR THE HL-LHC PROJECT”. In: *Proc. 4th International Particle Accelerator Conference*. paper WEPEA049 CERN-ACC-2013-0169. Shanghai, China: JACOW Publishing, Geneva, Switzerland, June 2013. URL: https://accelconf.web.cern.ch/AccelConf/ipac2013/papers/wepea049.pdf.

[5] E. H. Maclean et al. “New approach to LHC optics commissioning for the nonlinear era”. In: *Physical Review Accelerators and Beams* 22 (6 June 2019), p. 061004. DOI: 10.1103/PhysRevAccelBeams.22.061004.

[6] Helmut Wiedemann. *Particle accelerator physics*. Berlin; New York: Springer, 2007.

[7] G. E. Lee-Whiting. “Third-order aberrations of a magnetic quadrupole lens”. In: *Nuclear Instruments and Methods* 83.2 (June 1970), pp. 232–244. ISSN: 0029554X. DOI: 10.1016/0029-554X(70)90465-9.

[8] Étienne Forest and Janko Milutinović. “Leading order hard edge fringe fields effects exact in (1 + δ) and consistent with Maxwell’s equations for rectilinear magnets”. In: *Nuclear Instruments and Methods in Physics Research Section A: Accelerators, Spectrometers, Detectors and Associated Equipment* 269.3 (June 1988), pp. 474–482. ISSN: 01689002. DOI: 10.1016/0168-9002(88)90123-4.

[9] Massimo Giovannozzi, Stéphane Fartoukh, and Riccardo De Maria. “SPECIFICATION OF A SYSTEM OF CORRECTORS FOR THE TRIPLETS AND SEPARATION DIPOLES OF THE LHC UPGRADE”. In: *Proc. 4th International Particle Accelerator Conference*. Shanghai, China: JACOW Publishing, Geneva, Switzer-

land, June 2013, pp. 2612–2614. URL: https://accelconf.web.cern.ch/AccelConf/ipac2013/papers/wepea045.pdf.

[10] CERN. *CONVENTION FOR THE ESTABLISHMENT OF A EUROPEAN ORGANIZATION FOR NUCLEAR RESEARCH*. https://council.web.cern.ch/en/convention. July 1953.

[11] Vladimir Shiltsev and Frank Zimmermann. *Modern and Future Colliders*. 2020. arXiv: 2003.09084 [physics.acc-ph].

[12] Fabiola Gianotti, Michelangelo L Mangano, T Virdee, et al. "Physics potential and experimental challenges of the LHC luminosity upgrade". In: *The European Physical Journal C-Particles and Fields* 39.3 (2005), pp. 293–333. DOI: 10.1140/epjc/s2004-02061-6.

[13] Johann Rafelski. "Melting hadrons, boiling quarks". en. In: *The European Physical Journal A* 51.9 (Sept. 2015), p. 114. ISSN: 1434-601X. DOI: 10.1140/epja/i2015-15114-0.

[14] ATLAS Collaboration. "Observation of a New χ_b State in Radiative Transitions to $\Upsilon(1S)$ and $\Upsilon(2S)$ at ATLAS". In: *Physical Review Letters* 108.15 (Apr. 2012). Publisher: American Physical Society, p. 152001. DOI: 10.1103/PhysRevLett.108.152001.

[15] CMS Collaboration. "Observation of the $\chi_{b1}(3P)$ and $\chi_{b2}(3P)$ and Measurement of their Masses". In: *Physical Review Letters* 121.9 (Aug. 2018). Publisher: American Physical Society, p. 092002. DOI: 10.1103/PhysRevLett.121.092002.

[16] Adrian Cho. "Higgs Boson Makes Its Debut After Decades-Long Search". en. In: *Science* 337.6091 (July 2012), pp. 141–143. ISSN: 0036-8075, 1095-9203. DOI: 10.1126/science.337.6091.141.

[17] S. Chatrchyan et al. "Observation of a new boson at a mass of 125 GeV with the CMS experiment at the LHC". en. In: *Physics Letters B* 716.1 (Sept. 2012), pp. 30–61. ISSN: 0370-2693. DOI: 10.1016/j.physletb.2012.08.021.

[18] G. Aad et al. "Observation of a new particle in the search for the Standard Model Higgs boson with the ATLAS detector at the LHC". en. In: *Physics Letters B* 716.1 (Sept. 2012), pp. 1–29. ISSN: 0370-2693. DOI: 10.1016/j.physletb.2012.08.020.

[19] CMS Collaboration. "Measurement of the $B_s^0 \to \mu^+\mu^-$ Branching Fraction and Search for $B^0 \to \mu^+\mu^-$ with the CMS Experiment". In: *Physical Review Letters* 111.10 (Sept. 2013). Publisher: American Physical Society, p. 101804. DOI: 10.1103/PhysRevLett.111.101804.

[20] LHCb Collaboration. "Observation of Two New Ξ_b^- Baryon Resonances". In: *Physical Review Letters* 114.6 (Feb. 2015). Publisher: American Physical Society, p. 062004. DOI: 10.1103/PhysRevLett.114.062004.

[21] LHCb Collaboration. "Observation of the Resonant Character of the Z(4430) State". In: *Physical Review Letters* 112.22 (June 2014). Publisher: American Physical Society, p. 222002. DOI: 10.1103/PhysRevLett.112.222002.

[22] LHCb Collaboration. “Amplitude analysis of $B^+ \to J/\psi\phi K^+$ decays”. In: *Physical Review D* 95.1 (Jan. 2017). Publisher: American Physical Society, p. 012002. DOI: 10.1103/PhysRevD.95.012002.

[23] Oliver Sim Brüning et al., eds. *LHC Design Report v.1 : the LHC Main Ring*. eng. Vol. v.1 : the LHC Main Ring. CERN Yellow Reports: Monographs. Geneva, Switzerland: CERN, 2004. ISBN: 978-92-9083-224-9. URL: https://cds.cern.ch/record/782076/files/CERN-2004-003-V1-ft.pdf.

[24] CERN. *FiDeL home: the Field Model of the LHC*. https://lhc-div-mms.web.cern.ch/lhc-div-mms/tests/MAG/Fidel/. 2019.

[25] G. Apollinari et al., eds. *High-Luminosity Large Hadron Collider (HL-LHC): Technical Design Report V.0.1*. eng. Vol. 4 /2017. CERN Yellow Reports: Monographs 2017-007-M. Geneva, Switzerland: CERN, 2017. ISBN: 978-92-9083-470-0. DOI: 10.23731/CYRM-2017-004.

[26] RB Palmer. *Energy scaling, crab crossing and the pair problem*. Tech. rep. SLAC-PUB-4707. Stanford Linear Accelerator Center, Menlo Park, CA (USA), 1988. URL: https://www.slac.stanford.edu/pubs/slacpubs/4500/slac-pub-4707.pdf.

[27] Katsunobu Oide and Kaoru Yokoya. “Beam-beam collision scheme for storage-ring colliders”. In: *Phys. Rev. A* 40 (1 July 1989), pp. 315–316. DOI: 10.1103/PhysRevA.40.315.

[28] Yi-Peng Sun et al. “Beam dynamics aspects of crab cavities in the CERN Large Hadron Collider”. In: *Phys. Rev. ST Accel. Beams* 12 (10 Oct. 2009), p. 101002. DOI: 10.1103/PhysRevSTAB.12.101002.

[29] Lee Carver et al. “First machine development results with HL-LHC crab cavities in the SPS. First machine developments result with HL-LHC crab cavities in the SPS”. en. In: (2019), p. 4. DOI: 10.18429/JACoW-IPAC2019-MOPGW094.

[30] Stéphane Fartoukh. “Pile up management at the high-luminosity LHC and introduction to the crab-kissing concept”. In: *Phys. Rev. ST Accel. Beams* 17 (11 Nov. 2014), p. 111001. DOI: 10.1103/PhysRevSTAB.17.111001.

[31] I Béjar Alonso et al. *High-Luminosity Large Hadron Collider (HL-LHC): Technical design report*. en. CERN-2017-007-M. Vol. 10. CERN Yellow Reports: Monographs. doi:10.23731/CYRM-2020-0010. Dec. 2020. ISBN: 978-92-9083-587-5.

[32] Rogelio Tomás. “Direct Measurement of Resonance Driving Therms in the Super Proton Synchrotron (SPS) of CERN using Beam Position Monitors”. Ph.D. thesis. Univeritat de Valéncia, Spain, Jan. 2003.

[33] Oliver Brüning and Stéphane Fartoukh. *Field Quality Specification for the LHC Main Dipole Magnets*. Tech. rep. LHC-Project-Report-501. Geneva, Switzerland: CERN, Oct. 2001. URL: https://cds.cern.ch/record/522049/files/lhc-project-report-501.pdf.

[34] CERN - BE/ABP Accelerator Beam Physics Group. *MAD - Methodical Accelerator Design*. https://mad.web.cern.ch/mad. May 2019.

[35] Riccardo De Maria, Stephane Fartoukh, and Massimo Giovannozzi. "Specifications of the Field Quality at Injection Energy of the New Magnets for the HL-LHC Upgrade Project". en. In: *Proc. 4th International Particle Accelerator Conference*. Shanghai, China: JACOW Publishing, Geneva, Switzerland, June 2013, p. 3. URL: http://accelconf.web.cern.ch/AccelConf/ipac2013/papers/wepea045.pdf.

[36] Abele Simona. "Numerical methods for the simulation of particle motion in electromagnetic fields". eng. Ph.D. thesis. Milan: Dipartimento di Matematica, Politecnico di Milano, Mar. 2020. URL: https://www.politesi.polimi.it/handle/10589/152527.

[37] Chad Mitchell. "Calculation of Realistic Charged-Particle Transfer maps". eng. Ph.D. thesis. College Park: University of Michigan, 2007. URL: https://www.physics.umd.edu/dsat/dsattheses.html.

[38] Herbert Goldstein, Charles P. Poole, and John L. Safko. *Classical mechanics*. eng. 3. ed. OCLC: 248389949. San Francisco, NJ: Addison Wesley, 2002. ISBN: 978-0-201-65702-9.

[39] Y. K. Wu, E. Forest, and D. S. Robin. "Explicit symplectic integrator for *s* -dependent static magnetic field". en. In: *Physical Review E* 68.4 (Oct. 2003), p. 046502. ISSN: 1063-651X, 1095-3787. DOI: 10.1103/PhysRevE.68.046502.

[40] E.D. Courant and H.S. Snyder. "Theory of the Alternating-Gradient Synchrotron". en. In: *Annals of Physics* 281.1-2 (Apr. 2000), pp. 360–408. ISSN: 00034916. DOI: 10.1006/aphy.2000.6012.

[41] S. White, E. Maclean, and R. Tomás. "Direct amplitude detuning measurement with ac dipole". en. In: *Physical Review Special Topics - Accelerators and Beams* 16.7 (July 2013), p. 071002. ISSN: 1098-4402. DOI: 10.1103/PhysRevSTAB.16.071002.

[42] A J Draft et al. "Lie Algebraic Treatment of Linear and Nonlinear Beam Dynamics". In: *Annual Review of Nuclear and Particle Science* 38.1 (1988), pp. 455–496. DOI: 10.1146/annurev.ns.38.120188.002323.

[43] Alex J. Dragt. *Lie Methods for Nonlinear Dynamics with Applications to Accelerator Physics*. eng. U. S. Department of Energy Grant DE-FG02-96ER40949. University of Maryland, Aug. 2019. URL: http://www.physics.umd.edu/dsat/docs/Book19Nov2020.pdf.

[44] Etienne Forest, Martin Berz, and John Irwin. "Normal form methods for complicated periodic systems: a complete solution using differential algebra and lie operators". In: *Particle Accelerators* 24 (Jan. 1989), pp. 91–107. URL: https://cds.cern.ch/record/1053511/files/p91.pdf.

[45] Andrea Franchi. "Studies and Measurements of Linear Coupling and Nonlinearities in Hadron Circular Accelerators". Ph.D. thesis. Johann Wolfgang Goethe-Universität, Frankfurt, Germany, Sept. 2006.

[46] G Servizi et al. “A normal form approach to the theory of nonlinear betatronic motion”. eng. In: *CERN* CERN 94-02 (1994), p. 234. DOI: 10.5170/CERN-1994-002.

[47] R. Bartolini and F. Schmidt. “Normal form via tracking or beam data”. eng. In: *Particle Accelerators* 59 (1998), p. 10. URL: https://cds.cern.ch/record/333077/files/p93.pdf.

[48] Pedro Castro-Garcia. “Luminosity and beta function measurement at the electron-positron collider ring LEP”. Ph. D. thesis. CERN, Switzerland, Nov. 1996. URL: http://cds.cern.ch/record/316609/files/Thesis-1996-Castro.pdf.

[49] Ana Garcia-Tabares Valdivieso. “Optics-measurement-based Beam Position Monitor Calibration”. eng. Ph. D. Thesis. Universidad Complutense de Madrid, Sept. 2019. URL: http://cds.cern.ch/record/2701414/files/CERN-THESIS-2019-211.pdf.

[50] Patrik Goncalves Jorge. *Computation of Optics Distortions due to Beam-Beam Interactions in the FCC-hh*. Tech. rep. CERN-THESIS-2016-317. CERN and EPFL, May 2016. URL: http://cds.cern.ch/record/2275479.

[51] A. García-Tabarés Valdivieso and R. Tomas. “Optics-measurement-based beam position monitor calibrations in the LHC insertion regions”. en. In: *Physical Review Accelerators and Beams* 23.4 (Apr. 2020), p. 042801. ISSN: 2469-9888. DOI: 10.1103/PhysRevAccelBeams.23.042801.

[52] CERN - BE/ABP Accelerator Beam Physics Group. *SixTrack - 6D Tracking Code*. https://sixtrack.web.cern.ch/SixTrack. June 2019.

[53] Haruo Yoshida. “Construction of higher order symplectic integrators”. en. In: *Physics Letters A* 150.5 (Nov. 1990), pp. 262–268. ISSN: 0375-9601. DOI: 10.1016/0375-9601(90)90092-3.

[54] Ewen Hamish Maclean et al. *Report from LHC MD 1391: First tests of the variation of amplitude detuning with crossing angle as an observable for high-order errors in low-$\beta*$ colliders*. Tech. rep. CERN, Jan. 2017. URL: http://cds.cern.ch/record/2314409.

[55] Ewen Hamish Maclean et al. *Report from LHC MD 2158: IR-nonlinear studies*. eng. Tech. rep. CERN-ACC-Note-2018-0021. Geneva, Switzerland: CERN, Mar. 2018, p. 22. URL: http://cds.cern.ch/record/2306295/files/CERN-ACC-NOTE-2018-0021.pdf.

[56] Stephane Fartoukh. “Achromatic telescopic squeezing scheme and application to the LHC and its luminosity upgrade”. In: *Physical Review Special Topics - Accelerators and Beams* 16 (Nov. 2013). DOI: 10.1103/PhysRevSTAB.16.111002.

[57] Abele Simona et al. “High order time integrators for the simulation of charged particle motion in magnetic quadrupoles”. en. In: *Computer Physics Communications* 239 (June 2019), pp. 33–52. ISSN: 0010-4655. DOI: 10.1016/j.cpc.2019.01.018.

[58] Oliver Sim Brüning et al. *Dynamic Aperture Studies for the LHC Separation Dipoles*. Tech. rep. Geneva: CERN, June 2004. URL: http://cds.cern.ch/record/742967.

[59] J.L. Abelleira et al. "FCC-hh Final-Focus for Flat-Beams: Parameters and Energy Deposition Studies". In: *Proc. 8th International Particle Accelerator Conference* (Copenhagen, Denmark). International Particle Accelerator Conference 8. Geneva, Switzerland: JACOW Publishing, Geneva, Switzerland, May 2017, pp. 2139–2142. ISBN: 978-3-95450-182-3. DOI: https://doi.org/10.18429/JACoW-IPAC2017-TUPVA037.

[60] CERN - TE/MSC Magnets, Superconductors and Cryostats Group. *ROXIE - Electromagnetic simulation and Optimization of accelerator magnets*. https://espace.cern.ch/roxie. July 2009.

[61] A. Yamamoto et al. "Analysis of mechanical tolerances of a low-/spl beta/ quadrupole magnet for the LHC". In: *IEEE Transactions on Applied Superconductivity* 10.1 (Mar. 2000), pp. 131–134. DOI: 10.1109/77.828193.

[62] *Beta-Beat Source - Python-tool package of the optics measurements and corrections group (OMC)*. CERN - BE/ABP Accelerator Beam Physics Group. https://github.com/pylhc/Beta-Beat.src. Jan. 2020.

[63] R. Tomás. "Normal form of particle motion under the influence of an ac dipole". en. In: *Physical Review Special Topics - Accelerators and Beams* 5.5 (May 2002), p. 054001. ISSN: 1098-4402. DOI: 10.1103/PhysRevSTAB.5.054001. (Visited on 11/27/2019).

[64] Joschua Werner Dilly et al. *Report and Analysis from LHC MD 3311: Amplitude detuning at end-of-squeeze*. eng. Tech. rep. CERN-ACC-NOTE-2019-0042. Geneva, Switzerland: CERN, Mar. 2019, p. 39. URL: http://cds.cern.ch/record/2692810/files/CERN-ACC-NOTE-2019-0042.pdf.

[65] J.-L. Starck, Fionn Murtagh, and Jalal M. Fadili. *Sparse image and signal processing: wavelets and related geometric multiscale analysis*. Second edition. New York, NY: Cambridge University Press, 2015. ISBN: 978-1-107-08806-1.

[66] Jacques Laskar, Claude Froeschlé, and Alessandra Celletti. "The measure of chaos by the numerical analysis of the fundamental frequencies. Application to the standard mapping". en. In: *Physica D: Nonlinear Phenomena* 56.2 (May 1992), pp. 253–269. ISSN: 0167-2789. DOI: 10.1016/0167-2789(92)90028-L.

[67] *NAFF - Numerical Analysis of Fundamental Frequencies*. J. Laskar (ASD-IMCEE, Paris), Y. Papaphilippou, F. Asvesta, N. Karastathis and P. Zisopoulos (CERN). https://oraweb.cern.ch/pls/hhh/code_website.disp_code?code_name=NAFF or https://github.com/nkarast/PyNAFF. Oct. 2019.

[68] R Bartolini and F Schmidt. "SUSSIX: A computer code for frequency analysis of non-linear betatron motion". en. In: *Workshop on Nonlinear and Stochastic Beam Dynamics in Accelerators : a Challenge to Theoretical and Computational Physics, Luneburg, Germany* (Oct. 1997), pp. 390–394. URL: http://cds.cern.ch/record/394313.

[69] R. Bartolini and F. Schmidt. *A Computer Code for Frequency Analysis of Non-Linear Betatron Motion*. eng. Tech. rep. SL-Note-98-017-AP. Geneva, Switzerland: CERN, 1998, p. 8. URL: https://cds.cern.ch/record/702438/files/sl-note-98-017.pdf.

[70] N. Biancacci. *FFT corrections for tune measurements*. eng. June 2011. URL: https://indico.cern.ch/event/132526/contributions/128902/attachments/99707/142376/Meeting1-06-11_FFT_corrections_for_tune_measurements.pdf.

[71] A. Franchi et al. "First simultaneous measurement of sextupolar and octupolar resonance driving terms in a circular accelerator from turn-by-turn beam position monitors data". In: *Physical Review Special Topics - Accelerators and Beams* 17.7 (July 2014). arXiv: 1402.1461, p. 074001. ISSN: 1098-4402. DOI: 10.1103/PhysRevSTAB.17.074001. URL: https://arxiv.org/abs/1402.1461.

[72] E. Todesco and M. Giovannozzi. "Dynamic aperture estimates and phase-space distortions in nonlinear betatron motion". In: *Physical Review E* 53 (Apr. 1996), p. 4067. DOI: 10.1103/PhysRevE.53.4067.

[73] E. H. Maclean, M. Giovannozzi, and R. B. Appleby. "Innovative method to measure the extend of the stable phase-space region of proton synchrotrons". In: *Physical Review Accelerators and Beams* 22 (Mar. 2019), p. 034002. DOI: 10.1103/PhysRevAccelBeams.22.034002.

[74] S. Fartoukh and M. Giovannozzi. "Dynamic aperture computation for the as-built CERN Large Hadron Collider and impact of main dipoles sorting". In: *Nuclear Instruments and methods A* 671 (Apr. 2012), pp. 10–23. DOI: 10.1016/j.nima.2011.12.052.

[75] M. Hayes, E. McIntosh, and F. Schmidt. *The influence of Computer Errors on Dynamic Aperture Results Using SixTrack*. LHC Project Note 309. https://cds.cern.ch/record/692073/. Geneva, Switzerland: CERN, Jan. 2003.

[76] E. H. Maclean, M. Giovannozzi, and R. B. Appleby. "Innovative method to measure the extent of the stable phase-space region of proton synchrotrons". en. In: *Physical Review Accelerators and Beams* 22.3 (Mar. 2019), p. 034002. ISSN: 2469-9888. DOI: 10.1103/PhysRevAccelBeams.22.034002.

[77] A. Franchi, E. Métral, and R. Tomas. "Emittance sharing and exchange driven by linear betatron coupling in circular accelerators". en. In: *Physical Review Special Topics - Accelerators and Beams* 10.6 (June 2007), p. 064003. ISSN: 1098-4402. DOI: 10.1103/PhysRevSTAB.10.064003.

Titre: Dynamique des faisceaux de particules non-linéaire pour les upgrades du LHC

Mots clés: Physique des accélérateurs, Dynamique non-linéaire, Schémas symplectiques

Résumé:
La réalisation des futurs collisionneurs circulaires de protons dépend d'avancées technologiques décisives. En particulier, les aimants supraconducteurs seront construits en technologie Nb3Sn, ce qui permettra d'augmenter leur ouverture et leur champ magnétique. La qualité du champ (i.e. l'homogénéité) de cette nouvelle technologie va influencer la dynamique du faisceau. Des méthodes avancées de modélisation et de simulation doivent être utilisées et ultérieurement développées pour la conception des futures accélérateurs. En effet, des imperfections du champs magnétique des aimants, même très faible, pourraient avoir un impact important en limitant les performance de l'anneau, en particulier sur la dynamique de faisceau à long terme. La prise en compte de ces effets exige un modèle détaillé et réaliste du champ magnétique des aimants, y compris de ses champs de fuite. La description de ces champs magnétiques peut-être obtenue, sous la forme de champ à 3 dimensions sur une grille ou sous la forme d'harmoniques longitudinales, par différents codes à éléments finis (par exemple le code ROXIE du CERN) et/ou par des mesures directement sur les aimants. Pour décrire de façon réaliste les effets de ces champs sur la dynamique du faisceau à long terme, il est nécessaire de pouvoir utiliser ces informations dans les codes qui simulent le transport des particules.
Dans cette thèse, une nouvelle carte de transfert pour décrire ces imperfections de champ a été développée et implémentée dans le code de transport du CERN, SixTrack. Celle-ci a permis de quantifier pour la première fois l'impact des imperfections 3D du champ sur des observables faisceau, tel que la variation du nombre d'onde et de la fonction bétatronique de la machine avec l'amplitude et l'ouverture dynamique. Quand cela est possible, une expression analytique a été dérivée et comparée aux simulations.

Title: 3D non-linear beam dynamics for the LHC upgrades

Keywords: Accelerator Physics, Nonlinear beam dynamics, Symplectic maps

Abstract:
In order to boost the precision of the physics measurements, an improvement of a factor 10 of the LHC luminosity is planned for the next decade. A key ingredient of this upgrade is the need to use a new technology for the superconducting magnets which allows increasing the available peak field at a given aperture. The field quality of this new technology influences the beam dynamics; in large rings very little effects can have an important impact on the long term motion of the particle in the accelerator. This motion can be studied by means of transfer maps. For the individual elements of the beam line, these maps can in general depend sensitively on non-linear fringe-field and high-multipole effects, usually concentrated at magnets extremities. The inclusion of these effects in the particle dynamics requires a detailed and realistic model of the full magnetic field, including its fringe fields. The accurate description of the field can be obtained by various finite element field codes, in form of 3-dimensional field data on a grid. Starting from these field maps (or equivalent magnetic measurements) and using Fourier analysis, it is possible to compute the transfer map.
In this thesis, a new transfer map describing this 3D field imperfections has been developed and implemented into the CERN Tracking code, SixTrack. This allows to quantify for the first time the impact of such imperfections on beam-based observables such as Amplitude Detuning, measured Amplitude Beta-Beating and Dynamic Aperture. When possible an analytical expression have been derived and compared to simulations.

Université Paris-Saclay
Espace Technologique / Immeuble Discovery
Route de l'Orme aux Merisiers RD 128 / 91190 Saint-Aubin, France